UNIVERSTIY OF CALIFORNIA SAN DIEGO

Bioinspired liquid crystal elastomer (LCE) based soft actuators with multimodal actuation

A dissertation submitted in partial satisfaction of the requirements for the degree Doctor of Philosophy

in

Engineering Sciences (Mechanical Engineering)

by

Qiguang He

Committee in charge:

Professor Shengqiang Cai, Chair
Professor Renkun Chen
Professor Shaochen Chen
Professor Nicholas G. Gravish
Professor Michael T. Tolley

2021

The Dissertation of Qiguang He is approved, and it is acceptable in quality and form for publication on microfilm and electronically.

University of California, San Diego

2021

Table of Contents

List of Figures

Acknowledgements

I could not finish my PhD thesis without the help and support from many people, I would like to express my sincere gratitude to all of them.

First, I would like to express my deepest and heartiest appreciation to my world's best Ph.D. advisor, Prof. Shengqiang Cai, who gives me his fully support in every aspect ranging from research to life. His excellent insight, deeply understanding and great passion in mechanics of materials field guide me through my entire Ph.D. career. In the past six years, I learn a lot of knowledge in mechanics from him when we have discussions. More importantly, I also learn how to find a valuable problem and come up with an idea to solve this problem. I feel extremely exciting and lucky under his training at Cai group.

Second, I would like to my other dissertation committee members: Prof. Renkun Chen, Prof. Shaochen Chen, Prof. Nicholas G. Gravish and Prof. Michael T. Tolley for their valuable suggestions, comments, kid assistances and times to my research projects.

Third, I would like to thank Prof. Zhijian Wang, who teaches me how to do experiment. I learn a lot from him in the past five years when we discuss and share ideas. Prof. Zhijian Wang is always supportive and inspiring to me, which gives me power to overcome the obstacles in my research projects.

Then I am very grate grateful to our previous and current group member, thank you for creating excellent atmosphere in the lab, this is paradise in terms of doing research. They are Chihyung Ahn, Xudong Liang, Somaye Jafari, Yue Zheng, Zhaoqiang Song, Yang Wang, Zijun

Wang, Gaoweiang Dong, Chenghai Li, Raja Annapooranan, Nada F. Qari, Wei Fan.

Finally, I would like to give my gratitude to my parents and my friends for taking good care of me and giving me all the unconditional love and understanding.

Chapter 2, in full, is a reprint of the material as it appears in "Electrically controlled liquid crystal elastomer-based soft tubular actuator with multimodal actuation", *Science advances* 5 (2019): eaax5746, by Qiguang He, Zhijian Wang, Yang Wang, Adriane F. Minori, Michael T. Tolley and Shengqiang Cai. The dissertation author was the primary investigator and first author of this paper.

Chapter 3, in full, is a reprint of the material as it appears in "Bioinspired design of vascular artificial muscle", *Advanced Materials Technologies* 4 (2019): 1800244, by Qiguang He, Zhijian Wang, Zhaoqiang Song and Shengqiang Cai. The dissertation author was the primary investigator and first author of this paper.

Chapter 4, in full, is a reprint of the material as it appears in "Recyclable and self-repairable fluid-driven liquid crystal elastomer actuator", *ACS Applied Materials & Interfaces* 12 (2020): 35464-35474, by Qiguang He, Zhijian Wang, Yang Wang, Zhaoqiang Song and Shengqiang Cai. The dissertation author was the primary investigator and first author of this paper.

Chapter 5, in full, is currently being prepared for publication by Qiguang He, Zhijian Wang, Yang Wang, Zijun Wang, Chenghai Li, Jian Zeng, Raja Annapooranan, Renkun Chen and Shengqiang Cai. The dissertation author was the primary investigator and first author of this paper.

Vita

2015	Bachelor of Engineering, Tsinghua University
2016	Master of Science, University of California San Diego
2021	Doctor of Philosophy, University of California San Diego

Publications

1. **Q. He**, Z. Wang, Y. Yan, J. Zheng, S. Cai, "Polymer nanofiber reinforced double network gel composite: Strong, tough and transparent", *Extreme Mechanics Letters*, 9 (2016): 165-170.

2. **Q. He**, Z. Wang, Z. Song, S. Cai, "Bioinspired design of vascular artificial muscle", *Advanced Materials Technologies*, 4 (2019): 1800244.

3. **Q. He**, Z. Wang, Y. Wang, A. F. Minori, M. T. Tolley., S. Cai, "Electrically Controlled Liquid Crystal Elastomer Based Soft Tubular Actuator with Multimodal Actuation", *Science advances,* 5 (2019): eaax5746.

4. **Q. He**[#], Y. Zheng[#], Z. Wang, X. He, S. Cai, "Anomalous Inflation of a Nematic Balloon", *Journal of the Mechanics and Physics of Solids,* (2020): 104013.

5. **Q. He**[#], Z. Wang[#], Y. Wang, Z. Song, S. Cai, "Recyclable and self-repairable fluid-driven liquid crystal elastomer actuator", *ACS applied materials & interfaces* 12 (2020): 35464-35474.

6. **Q. He**, S. Cai, "Soft pumps for soft robots", *Science Robotics*, 6 (2021): eabg6640.

7. Z. Wang, **Q. He**, Y. Wang, S. Cai, "Programmable actuation of liquid crystal elastomer via "living" exchange reaction", *Soft matter*, 15 (2019): 2811-2816.

8. A. F. Minori, **Q. He**, P. Glick, A. Stopol, I. Adibnazari, S. Cai, M.T. Tolley, "Reversible actuation for self-folding modular machines using liquid crystal elastomer", *Smart Materials*

and Structures, 29 (2020): 105003.

9. B. Sun, Z. Wang, **Q. He**, W. Fan, S. Cai, "Porous double network gels with high toughness, high stretchability and fast solvent-absorption", *Soft matter*, 13 (2017): 6852-6857.

10. Z. Wang, W. Fan, **Q. He**, Y. Wang, X. Liang, S. Cai, "A simple and robust way towards reversible mechanochromism: Using liquid crystal elastomer as a mask", *Extreme Mechanics Letters*, 11 (2017): 42-48.

11. Z. Wang, H. Tian, **Q. He**, S. Cai, "Reprogrammable, reprocessible, and self-healable liquid crystal elastomer with exchangeable disulfide bonds", *ACS applied materials & interfaces*, 9 (2017): 33119-33128.

12. Z. Wang, K. Li, **Q. He**, S. Cai, "A Light-Powered Ultralight Tensegrity Robot with High Deformability and Load Capacity", *Advanced Materials*, 31 (2019): 1806849.

13. Y. Wang, Z. Wang, **Q. He**, P. Lyer, S. Cai, "Electrically controlled soft actuator with multiple and reprogrammable actuation modes", *Advanced Intelligent Systems* 2 (2020): 1900177.

14. X. He, Y. Zheng, **Q. He**, S. Cai, "Uniaxial Tension of a Nematic Elastomer with Inclined Mesogens", *Extreme Mechanics Letter*, 40 (2020): 100936.

15. Z. Wang, Z. Wang, Y. Zheng, **Q. He**, Y. Wang, S. Cai, "Three-dimensional printing of functionally graded liquid crystal elastomer", *Science advances*, 6 (2020): eabc0034.

16. A. F. Minori, S. Jadhav, **Q. He**, S. Cai, M. T. Tolley. "Reversible Actuation of Origami Inspired Composites Using Liquid Crystal Elastomers", In *ASME 2017 Conference on Smart Materials*, American Society of Mechanical Engineers, 2017.

Abstract of the Dissertation

Bioinspired liquid crystal elastomer (LCE) based soft actuators with multimodal actuation

by

Qiguang He

Doctor of Philosophy in Engineering Sciences (Mechanical Engineering)

University of California San Diego, 2021

Professor Shengqiang Cai, Chair

Inspired by the biology, soft robots have drawn tremendous attention due to its large and continuous deformation, friendly human-machine interaction, large number of degrees of freedom (DOFs), capability of absorbing energy. They have been explored in broad applications ranging from dexterous soft gripper to the novel assistive devices. In the recent decade, numerous soft actuating materials and deformable structures have been developed to construct soft robots, including hydrogels, shape memory polymers (SMPs), dielectric elastomer actuators (DEAs), fluid elastomer actuators (FEAs) and magnetic actuators. However, those materials and structures have

well-known limitations such as slow actuation speed, irreversibility, high voltage input and bulky controlling systems. Liquid crystal elastomers (LCEs), as newly emerging soft actuating materials, exhibit large and reversible deformation and versatile actuation modes. Based on the molecular structure, LCE can be viewed as a combination of liquid crystal molecules and polymer networks. When the LCE is heated above the critical temperature, it can generate large deformation because of the nematic-isotropic phase transition. However, in terms of the practical use of LCE, a few challenges exist such as lack of programmable operation and slow responsive speed for LCEs, which need to be addressed.

In this dissertation, we first integrate flexible heating wire into LCE tube, forming electrically controlled soft tubular actuator. By selectively applying low electrical voltage, this soft tubular actuator can exhibit multiple actuation modes, such as different directional bending and homogeneous contraction. The LCE soft tubular actuator can also be integrated to construct untethered robot that can execute multiple functionalities. To address the slow responsive speed of LCE based soft actuator, we embed microfluidic channel into LCE, forming vascular LCE soft actuator. Through alternatively injecting hot and cold fluid into its internal fluidic channel, the vascular LCE soft actuator can generate fast actuation as well as recovery. In addition, by introducing the disulfide bonds into the LCE materials, the newly obtained vascular LCE based soft actuator has shown repairability and recyclability. Finally, we use electrospinning technique to fabricate LCE microfiber that can be actuated by NIR light. We demonstrate that the electrospun LCE fiber can be easily integrated to micro-robotic system and machine as artificial muscle fiber.

Chapter 1 Introduction

1.1 Background

Inspired by the biology, soft robotics have been extensively explored for diverse applications because of its intrinsic softness and compliance characteristics, large and continuous deformation, large number of degrees of freedom (DOFs), resilience to the impact. Compared with the conventional hard robots, soft robots can interact with human more friendly and safely, better handle delicate and fragile objects and operate in unplanned terrains [1]. Versatile soft robotics applications have been broadly demonstrated in the recent decade such as soft gripper [2], multi terrain robot [3] and medical assistant devices [4].

Recently, various soft actuating materials and deformable structures have been explored to construct soft robotics. For instance, responsive hydrogel can swell or shrink when the temperature is below or above its critical temperature [5]. Dielectric elastomer actuators (DEAs) can generate large deformation when high voltage is applied [6]. Shape memory polymers (SMPs) can change shapes upon the variation of the temperature [7]. Various forms of fluid elastomer actuators (FEAs) have been intensively studied as pneumatic and hydraulic artificial muscles in soft robotic applications [8, 9].

Though tremendous success has been achieved in the applications of those materials and structures, certain limitations have also been well recognized. For instance, the actuation of

environmental responsive hydrogels needs water environment, the actuation speed of hydrogel is based on diffusion process, which is always slow. To trigger the actuation of dielectric elastomer actuators, ultra-high voltage (> 10 kV) is often required, which is not always convenient for the designs. The actuation of shape memory polymer is always irreversible. To generate vacuum or pressurized air to actuate fluid elastomer actuators, bulky and noisy pumps are included into the whole system, which limit reduction of size and untethered applications.

1.2 Liquid crystal elastomers (LCEs) overview

Liquid Crystal Elastomer (LCE), a combination of liquid crystal molecules (mesogens) and polymer networks, has been broadly studied and developed because of its extraordinary properties such as large and reversible actuations, anisotropic mechanical properties and optical properties, which demonstrates versatile possibilities ranging from artificial muscles [10], biomimetic structures [11], soft robotics [12]. Recent trends surrounding LCEs are built on its reversible actuation, which is determined by order-disorder arrangement of mesogens microscopically. These mesogens undergo phase transition from nematic state (mesogens are well aligned in ordered state) to isotropic state (mesogens behave randomly oriented) which can be driven by the external stimulus such as heats [13], lights [14], and chemicals [15]. The development of LCE undergoes renaissance stage from scientific and engineering perspectives, ranging from material preparations, structure designs to potential applications.

Traditional fabrication of LCE can be classified into two categories: one pot polymerization and two-step polymerization routes [16]. The alignment of mesogens varies depend on the fabrication process. In terms of one pot polymerization, the mesogens, spacer and crosslinker are incorporated together, during the reaction process, the mesogens can be oriented with the surface rubbering effect, magnetic and electric aid. After reaction, the LCE with specific alignment of mesogens can be fabricated. It is noted that the arrangement of mesogens can be controlled precisely but the efficient is relatively low. Therefore, the one pot polymerization method typically provides thin film LCE while two-step polymerization method has been developed in order to fabricate the large scale with commercially available chemicals. The loosely crosslinked polymer networks are formed after first crosslinking process, after that, the external mechanical stretch is applied to the loosely crosslinked LCE to re-orient the arrangement of mesogens, then the sample is stimulated to the second crosslinking process, finally, the arrangement of mesogens can be fixed [17]. Normally, the alignment of mesogens for two-step polymerization cannot become complicated although recent studies have shown some techniques such as applying inhomogeneous stretching method.

With recent development of 4D printing techniques, LCE can be directly fabricated through direct ink write (DIW) method [18, 19]. During this process, the oligomers (ink) need to be heated up (tune viscosity) and loaded into nozzle, as the ink is gradually extruded from the nozzle, mesogens can be directly aligned by shear force, then the sample can be UV photo crosslinked after printing. The uniqueness of DIW is that mesogens can be spatially determined achieved

through designing the printing pathway, resulting in complex 3D deformation modes can be easily realized.

The LCE which contains exchangeable dynamic bonds has been recent studied that enables it to possess not only good mechanical properties and but also processability [20]. In particular, for LCE which is composed exchangeable disulfide bonds [21, 22], disulfide exchanging reaction happens under heat or UV environment, the LCE is able to show self-healing capability, reprogrammability and processability, which may open a new door for fabricating LCE.

Joule heating can directly trigger the nematic – isotropic phase transition of LCE which leads it to generate macroscopic actuation based on pre-determined shapes. To provide Joule heating that LCE need to absorb, several methods have been adopted in previous studies including embedding heating element and designs of vascular architectures. Embedding flexible, stretchable heating wire or conductive inks into LCE is one simple way to provide Joule heat which enables LCE to realize programmability, locomotion and compact design [23, 24]. However, passive and external cooling mechanisms always restrict the recovery speed of LCE which is not desired for most applications. Inspired by the biological vascular architectures in plants and human muscle, microfluidic channel can be created into LCE, through alternatively injecting high and low temperature of fluid into its internal fluidic channels, the LCE can realize fast actuation as well as recovery [25, 26].

Lights provide appealing alternative due to its remote and wireless control. Typically, light triggered nematic - isotropic phase transition of LCE can be classified into two categories:

photothermal actuations and photochemical actuations [27]. The photothermal actuation is based on the photothermal agents (nanoparticles, organic dyes) incorporated in LCE that convert light to heat, the temperature of LCE reach to transition temperature once it is exposed to light, resulting in actuation follow its pre-determined shape; photochemical actuation relies on photoisomerization of mesogens (trans and cis isomers transformation of specific mesogens such as azobenzene molecular and its derivatives). When UV light is penetrated into LCE, the length of mesogens decrease which driven LCE deform, the LCE recovery to its initial shape when it is shield to visible light to trigger cis-trans transformation. Combining photothermal and photochemical actuation, the LCE can be controlled via multiple wavelengths which endow LCE have multiple functions such as reprogrammabilities and multilight responsiveness actuators [28].

In addition, LCE can be synthesized to become chemical responsive actuators that can be driven by organic solvent and vapor such as Toluene and THF, which can be demonstrated as sensors [15].

Although most actuation achieved by LCE actuators are based on its nematic – isotropic transition, the actuation can be also generated based on other anisotropic materials properties such as soft elasticity and electrical permittivity [29, 30]. Thus, certain LCE structures can also be driven under the pressurized air (LCE balloon). This unique actuation mode provides higher energy efficiency compared with other mechanisms.

LCE have been largely developed as the actuator and sensor for broad applications due to its reversible deformation. Many previous studies demonstrate LCE as soft artificial muscle, the

contraction ratio (~ 50%), actuation stress (~ 1 MPa) and work density are comparable to mammalian muscle. Simple contraction can be achieved by external control such as heat and light. Through spatially patterning the mesogens of LCE, tremendous complex deformation modes can be realized. Therefore, the LCE can be exploited in a broad soft robotic application such as soft walkers [31], caterpillars [32], swimmers [33], tendrils [34], iris [35] and origami structures [36, 37]. Besides of actuators, LCE has been also demonstrated as sensors to sense external environments based on the change of arrangement of mesogens. For instance, the color of polydomain LCE changes from opaque to transparent (isotropic or monodomain) when the arrangement of mesogens change, using polydomain LCE as mask, our group develops mechanochromism device [38]. The LCE can also sense different chemical environment based on its deformations.

1.3 Dissertation structure

The objective of my dissertation is to design and fabricate the LCE based soft actuator that can generate multimodal actuation with fast responsive speed. Moreover, we expect these LCE based soft actuators have multiple functionalities and can be applied to broad practical applications in large and micro sizes. To achieve those goals, we mainly focus on synthesizing LCE material as well as developing new structure using LCE. We describe the design and fabrication process, characterize the actuation performance via experiments, apply the LCE based actuators to novel applications. This dissertation is organized as follows:

Chapter 1 introduces the background of soft robotics and overview of liquid crystal elastomers.

Chapter 2 describes the design, fabrication, characterizations and demonstrations of electrically controlled liquid crystal elastomer based soft actuators. This soft tubular actuator exhibits multiple actuation modes such as different directional bending as well as homogeneous contraction, which can be used to construct soft robotics that can achieve multifunctionalities. In Chapter 3, to address the slow responsive speed of LCE, we embed the microfluidic channel into the LCE forming vascular LCE soft actuator which demonstrates fast actuation as well as recovery. We discuss the design, fabrication, characterizations of vascular LCE artificial muscle. In Chapter 4, we modify the introduce disulfide LCE to the fabricate actuator. We then show the unique advantages of disulfide LCE based fluid driven actuator such as self-repairability and recyclability. In Chapter 5, we use electrospinning technique to fabricate LCE fiber actuator, we show that the actuation performance of LCE fiber are comparable to human skeleton muscle and the LCE fiber can be applied into broad micro robotic and device applications. In Chapter 6, we summary the dissertation and provide outlooks for the future works.

Chapter 2 Electrically controlled liquid crystal elastomer-based soft tubular actuator with multimodal actuation.

2.1 Introduction

In nature as well as engineering applications, we can often find actuators of cylindrical shape. For instance, the trunk of the elephant, the arms of the octopus and the tube feet of the starfish. Concentric tubular surgical robots [39, 40] and endoscopes [41-43] are representative examples from biomedical engineering, which can exhibit multimodal actuation. Those tubular actuators are usually made of stiff materials, in which a gear-and-shaft system is used to achieve their multimodal actuation.

Recent work has intensively explored soft continuum robots, and has demonstrated their many unique and attractive characteristics, such as a large number of degree of freedoms and high biocompatibility [1-3, 44, 45]. Notably, researchers have designed and fabricated various soft actuators with cylindrical shape to achieve various bioinspired movements, such as octopus-inspired robotic tentacles [46, 47], trunk-inspired manipulators [48] and worm-inspired architectures [49]. However, most previously constructed soft actuators were either pneumatically or hydrodynamically driven, which often require bulky external control system, complex internal channels for diverse actuation modes and the prevention of fluid leakage [50-52]. There is a clear need for stimuli-responsive material to construct soft actuators [53, 54], which has the potential to simplify fabrication and assembly processes and reduce the complexity of the controlling.

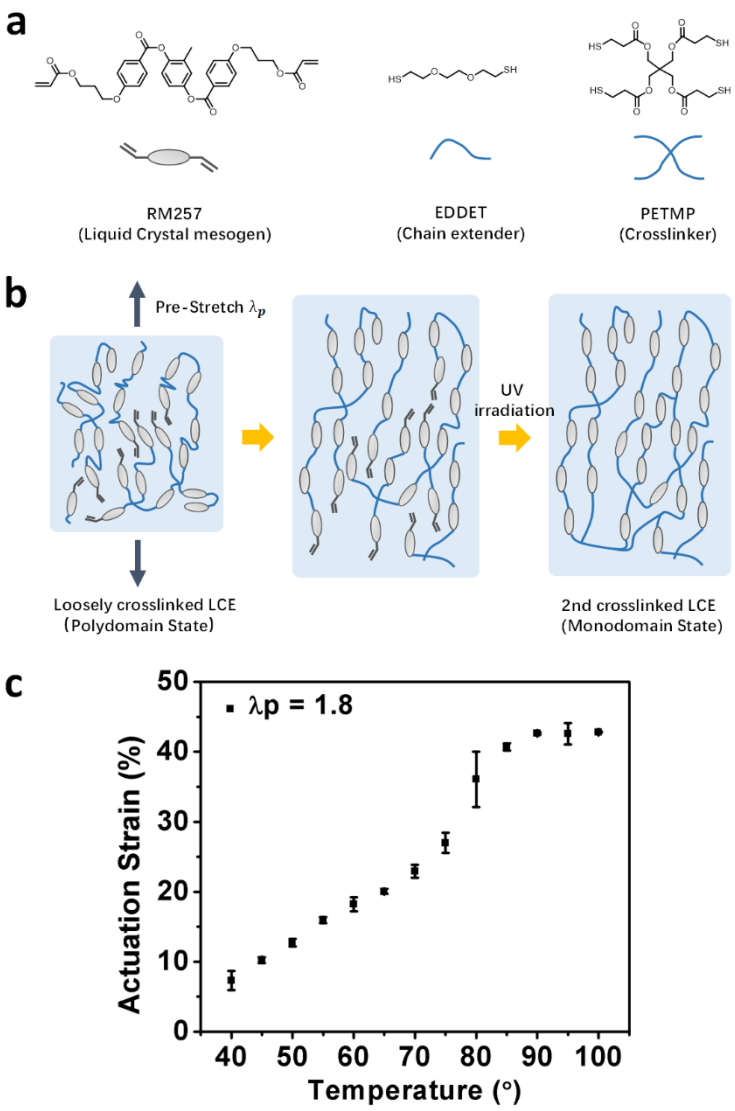

Figure 2.1: Chemical component, fabrication process and actuation performance of an LCE thin film. a RM257 is the liquid crystal mesogen, EDDET is the chain extender, and PETMP is the crosslinker. **b** Monodomain LCE is obtained through stretching loosely crosslinked LCE by λ_p to align the liquid crystal mesogen and then being exposed under UV irradiation to stimulate the second crosslinked process. **c** Plot of actuation strain versus temperature of LCE film with λ_p=1.8. Actuation strain would increase with the increase of temperature. The maximum actuation strain of LCE film is 41%, which is comparable to LCE artificial muscle with heating wires, implying that embedded heating wires do not restrict the deformation of LCE film.

Liquid crystal elastomer (LCE), a thermally-driven actuating material that combines polymer network and liquid crystal mesogens, as shown in Figure 2.1a, has attracted much attention recently due to its unique properties, including large (~40%) and reversible actuation, high processability and programmability [14, 21, 55-58]. As the temperature increases, liquid crystal mesogens transition from the nematic phase to the isotropic phase, leading to a significant and macroscopic deformation in the material. A variety of LCE-based actuating structures have been designed and successfully fabricated, which are often actuated by direct environmental heating [13, 59] or by light through photo-thermal and photochemical effects [33, 60-65]. However, for most practical applications, electronically-powered actuators provide significant convenience for system control and integration. A few recent studies have successfully integrated stretchable resistive heaters into LCE [24, 35, 66], whose actuation can be then easily controlled by electrical potential. In this article, we describe the design and fabrication of an LCE-based tubular actuator with multiple actuation modes and controlled by the externally applied electrical potential of several volts (1.0 to 3.0 V). To demonstrate the advantages of the soft tubular actuator in potential applications, we further fabricate an untethered soft robot with on-board power source and microcontroller, mainly driven by the LCE-based tubular actuators. Such features are often highly desired in constructing compact and multifunctional devices.

2.2 Results and discussion

2.2.1 Fabrication of LCE-based tubular actuator

Figure 2.2a and Figure 2.3 show the main steps of fabricating an LCE-based tubular actuator. We sandwiched three separate thin stretchable serpentine heating wires (as shown in Figure 2.4) between two layers of loosely crosslinked LCE films (1 mm, each) as shown in steps i) and ii). In step iii), we made the tubular shape by rolling the sandwich-like structure and stretching it by λ_p. The LCE tubular actuator could be finally obtained once the entire structure was exposed to UV irradiation to fix the alignment of the liquid crystal mesogens inside.

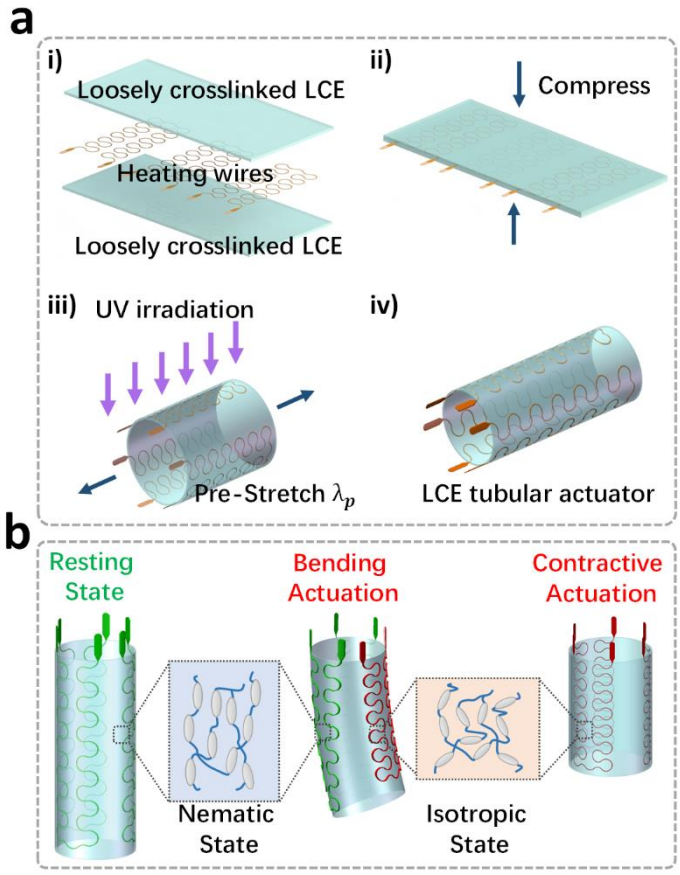

Figure 2.2: Design, fabrication, and operation principle of an LCE tubular actuator. a Fabrication steps of an LCE-based tubular actuator: i) Three serpentine heating wires were sandwiched between two layers of loosely crosslinked LCE films. ii) The sandwiched structure was compressed slightly to promote adhesion. iii) A tube was made by rolling the thin film. iv) An LCE tubular actuator was obtained by stretching and then exposing the actuator under UV irradiation. **b** Principle of operation of LCE tubular actuators. Bending motion can be realized by applying an electrical potential to one of the heating wires (colored red), homogeneous contraction can be obtained by applying an electrical potential to all heating wires (colored red).

In nature, animals such as mammals can contract muscles in different parts in their bodies to achieve multimodal actuation. Similarly, the fabricated LCE-based tubular actuator contains three separate heating wires which can be controlled independently, as shown in Figure 2.2b. The electric current going through the metallic wires generate Joule heating and increases the

temperature of the adjacent LCE. Consequently, the heated LCE can contract in the longitudinal direction. By applying an electrical potential onto different embedded heating wires, we achieve various actuating modes. For example, if only one of the heating wires generates Joule heating, the tube can bend toward one direction; while if all three heating wires generate Joule heating, the tube can contract homogenously.

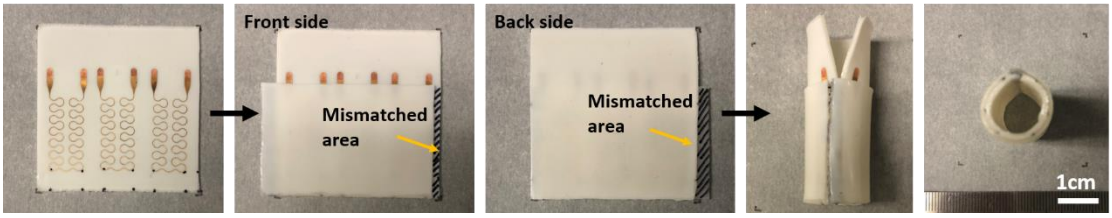

Figure 2.3: Process of the fabrication of an LCE tubular actuator. Three separate heating wires were firstly transferred to a thin LCE sheet. Then, the second layer of LCE sheet was used to cover the three heating wires. Two mismatched areas between the two LCE sheets were intentionally introduced on the edges. These two mismatched areas were bonded to each other after rolling. Finally, the tube was placed under UV light for the second polymerization, and the interfaces of the two layers were bonded through covalent bonds.

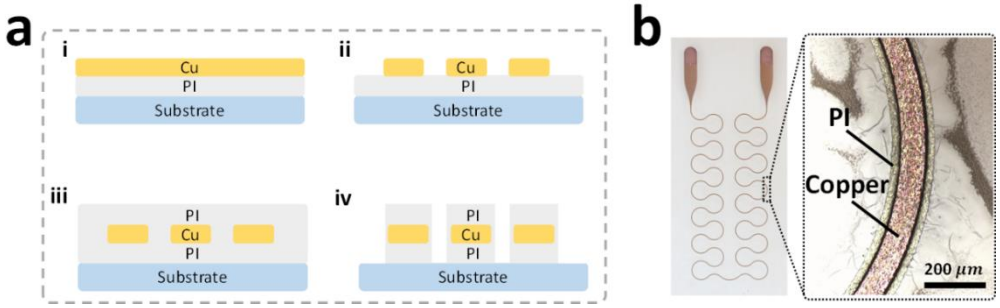

Figure 2.4: Design, fabrication, and morphology of heating wire. a Fabrication process of heating wire. In the first step, copper coated with polyimide (PI) was placed on the glass substrate. In the second step, the pattern was achieved through photolithography following by wet etching. In the third step, another PI layer was spin coated on the pattern and cured in the oven. In the fourth step, the pattern was achieved by photolithography following by dry etching. **b** Morphology of heating wire. 100 μm width copper was capsuled by 150 μm PI layer.

2.2.2 Electrical potential-driven actuation of an LCE thin film

To better control the actuation of the tubular actuator, we first fabricated and characterized the actuation behavior of an LCE artificial muscle film. The fabrication of LCE artificial muscle film is similar to that of the LCE tubular actuator. A freestanding LCE artificial muscle film contracted by 41% of its initial length as 3.0 V was applied, as shown in Figure 2.5a. When we turned off the electrical potential, the temperature of LCE artificial muscle gradually decreased to room temperature, and the LCE artificial muscle recovered to its original shape within 4 min. To quantitatively characterize the actuation of the LCE-based artificial muscle, we define the actuation strain as: $\varepsilon = (L - l)/L \times 100\%$, where L and l are the lengths of LCE artificial muscle in the initial and actuated states, respectively.

Thermal images (taken by FLIR E75-42 Advanced Thermal Imaging Camera) in Figure 2.6a showed the surface temperature of LCE artificial muscle film during the heating process when we applied 3.0 V to it. The highest temperature on the surface increased from 20 ℃ to 120 ℃ within 30 s, and the actuation strain of the LCE artificial muscle reached 41%. We also noticed that nearly homogeneous temperature distribution could be generated on the surface of the artificial muscle via Joule heating and thermal diffusion after the 30 s of heating. If we applied the electrical potential onto the heating wires for a longer time, the surface temperature of the artificial muscle could be further increased to 220 ℃, while the actuation strain maintained its 41% contraction. We had also shown, in Figure 2.1c, that the embedding heating wires of serpentine shape have a negligible influence on the actuation behavior of LCE films.

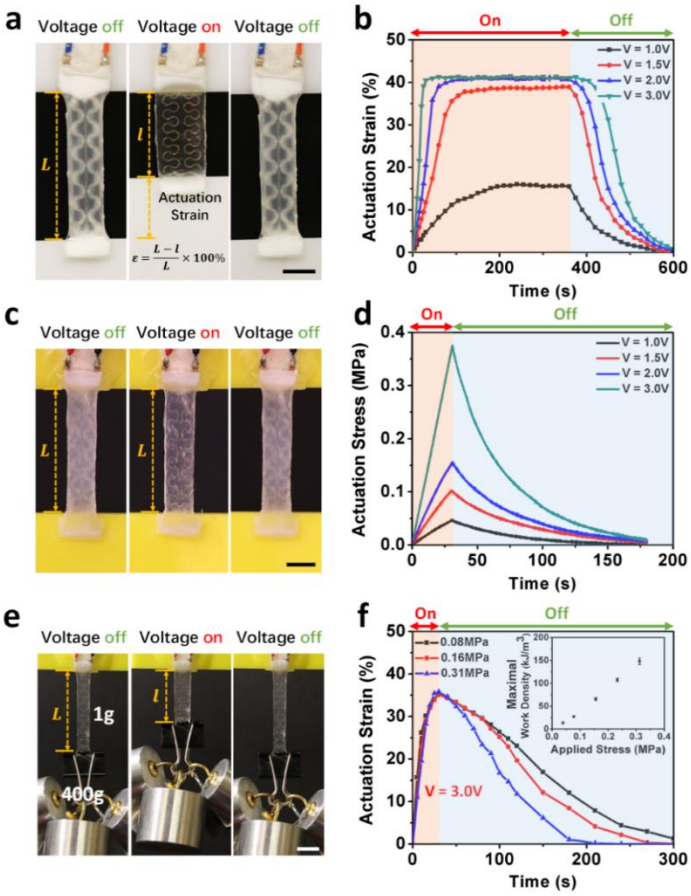

Figure 2.5: Thermo-mechanical characterizations of LCE artificial muscle film. a Optical images of reversible actuation of the artificial muscle: the film contracted by 40% of its initial length when an electrical potential of 3.0 V was applied. **b** Plot of actuation strain of LCE artificial muscle versus time with different applied electrical potential ranging from 1.0 V to 3.0 V. For a given electrical potential, actuation strain increased then reached a plateau value (steady state). When the electrical potential increased from 1.0 V to 2.0 V, the actuation strain at steady state increased from 15% to 41%. As the electrical potential further increased from 2.0 V to 3.0 V, the actuation strain of LCE artificial muscle at steady state remained the same, while the response time (time for reaching the steady state) decreased from 100 s to 30 s. **c** and **d** Actuation stress of the artificial muscle film (with fixed length) versus time with different electrical potentials ranging from 1.0 V to 3.0 V for 30 s. The actuation stress increased from 0.05 MPa to 0.35 MPa as the electrical potential was increased from 1.0 V to 3.0 V. **e** An LCE artificial muscle film could lift a load of 3.92 N (the stress was 0.312 MPa) by 38% of its initial length. **f** Actuation strain of the LCE artificial muscle film versus time under three different levels of applied stresses. As the load was increased, the time needed for the LCE film to contract was almost unchanged, while the time needed for it to recover to its original length decreased. Inset: maximal work density of LCE artificial muscle under different applied stresses. Scale bars in **a**, **c** and **e**: 1 cm.

Next, we quantitively characterized the actuation behaviors of LCE artificial muscle when different electrical potentials were applied. In Figure 2.5b, we showed the actuation strain of LCE artificial muscle versus time with four different levels of electrical potential (1.0 V, 1.5 V, 2.0 V, and 3.0 V) for 360 s. For a given electrical potential, the actuation strain of LCE artificial muscle increased at the beginning and then reached a plateau value either because the temperature field in the artificial muscle reached a steady state or because the actuation was at its maximal value (41%). As we turned off the electrical potential, the actuation strain decreased to zero within 240 s. When we increased the electrical potential from 0.5 V to 2.0 V, the maximal actuation strain rose from 15% to 41%. As we incremented the electrical potential further from 2.0 V to 3.0 V, the maximal actuation strain maintained the same value (41%), but the response time decreased. It took about 30 s for the LCE artificial muscle to reach the maximum contraction (41%) when 3.0 V was applied, compared with 150 s while 2.0 V was applied. As shown in Figure 2.6b, as we increased the electrical potential from 1.0 V to 2.0 V, the surface temperature of the LCE films in the steady state was increased from 55 °C to 120 °C. Correspondingly, the actuation strain of the LCE artificial muscle was increased from 16% to 41%, as shown in Figure 2.5b. If we further increased the electrical potential from 2.0 V to 3.0 V, and the maximal surface temperature increased from 120 °C to 220 °C (Figure 2.6b), the actuation strain of LCE film stayed unchanged (Figure 2.5b). We also showed that the performance of the LCE artificial muscle film almost remained unchanged after more than 50 cycles and 100 cycles of actuation with an applied electrical potential of 3.0 V

and 2.0 V, respectively (Figure 2.7). Moreover, no delamination between LCE layer and heating wire was observed in cyclic heating and cooling process in the experiments.

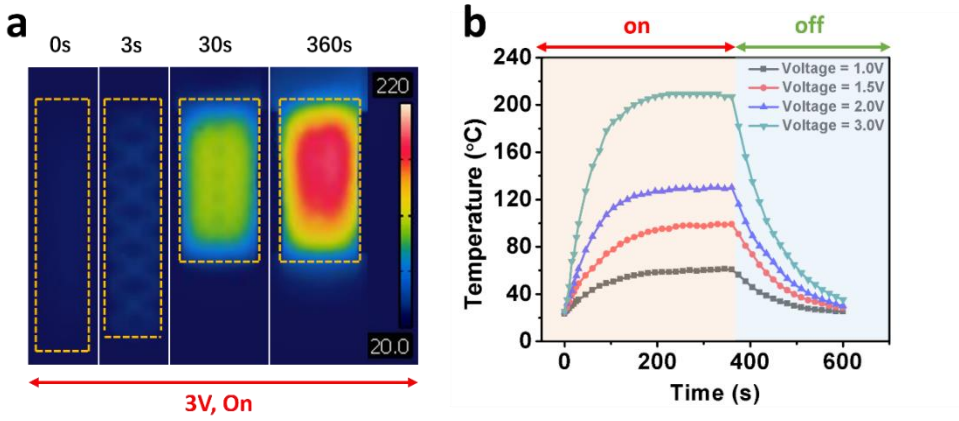

Figure 2.6: Temperature change of the LCE artificial muscle film during contraction and recovery. **a** Screenshots of the IR video showing the thermal image of the artificial muscle during its contraction when an electrical potential of 3.0 v was applied. **b** Surface temperature (measured by IR camera) of the artificial muscle film with several different applied electrical potentials. The surface temperature increased at the beginning, and then reached a steady state. When the electrical potential was turned off, the surface temperature of LCE artificial muscle decreased. As the electrical potential was increased from 1.0 V to 3.0 V, the surface temperature at the steady-state increased from 55 °C to 220 °C.

By fixing the length of the LCE artificial muscle film (Figure 2.5c), we studied its actuation stress of fixed length with different applied electrical potentials ranging from 1.0 V to 3.0 V for 30 s. For a given electrical potential, the actuation stress increased from zero to the maximum value within 30 s and dropped to zero when we turned off the electrical potential. As the electrical potential increased from 1.0 V to 3.0 V, the maximal actuation stress increased from 0.05 MPa to

0.35 MPa, which is shown in Figure 2.5. We noted that the typical actuating stress generated by skeletal muscles of most mammals is also around 0.1 to 0.35 MPa [25].

We also measured the work density of LCE artificial muscle film by applying a constant load onto the LCE artificial muscle film and an electrical potential of 3.0 V (Figure 2.5e and f). In the experiment, we measured the contraction of the artificial muscle film with five different loads ranging from 0.49 N to 3.92 N. We calculated the mechanical work done by the artificial muscle film by multiplying the magnitude of the load by the maximal displacement of contraction, as shown in Figure 2.5e. The maximal work density can be further obtained by dividing the mechanical work by the volume of the LCE artificial muscle film. As shown in the inset of Figure 2.5f, the maximal work density of the LCE artificial muscle film could reach as high as 150 kJ/m^3 when the applied stress was 0.31 MPa, which was comparable to that of dielectric elastomer membrane and mammalian skeletal muscle, but higher than that of ionic polymer-metal composites (IPMC)and piezoelectric actuators [53].

Finally, we would like to point out that, like other thermally responsive materials, the actuation bandwidth of LCE actuators depends primarily on the characteristic time of heat transfer in the material. The thermal conductivity of LCE is low, so their response time is relatively slow, as shown in Figure 2.5b, d and f. The most effective way to reduce the response time is to decrease the size of the material or, more precisely, the characteristic size of the heating area. However, this modification could adversely affect other actuation performance of the LCE actuators, such as the

actuation force and strain. Therefore, an optimized design will certainly be needed to achieve a desirable combination of actuation speed, strain and stress for specific applications.

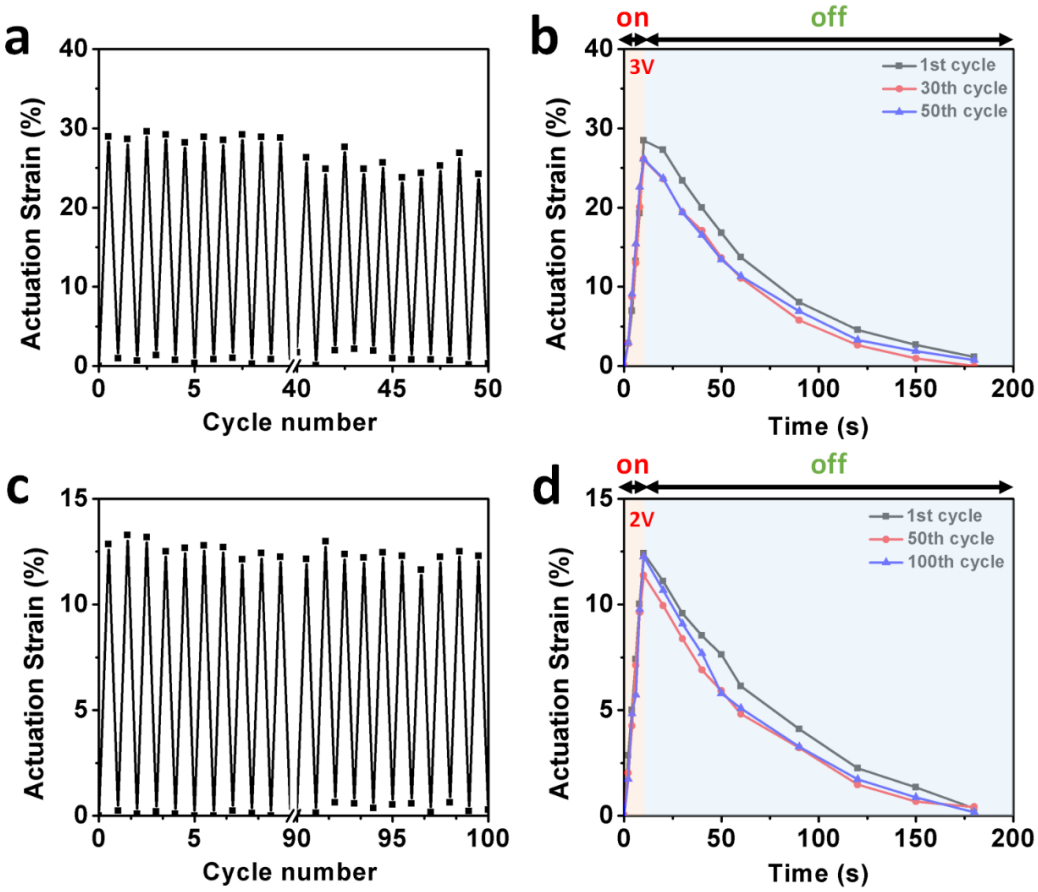

Figure 2.7: Cyclic actuation test of the LCE artificial muscle film with applied stress of 0.078 MPa. a in one cycle of test, an electrical potential of 3.0 V was applied to an LCE artificial muscle film for 10 s, and the electrical potential was turned off for 180 s. **b** the maximal actuation strain decreased from 30% to 26% after 50 cycles of tests. Such performance degradation might be due to the increase of the electrical resistance of the heating wires, which was caused by the oxidization of the copper heating wires. **c** in one cycle**,** an electrical potential of 2.0 V was applied to an LCE artificial muscle film for 10 s, and the electrical potential was turned off for 180 s. **d** the actuation behavior of the actuator was almost unchanged after 100 cycles of actuation.

2.2.3 Electrical potential-controlled multimodal actuation of a tubular actuator

We also characterized the multimodal actuation of an LCE tubular actuator. In Figure 2.8 (a and b), we demonstrated that applying an electrical potential onto one or two of the heating wires (same electrical potential for both heating wires) could generate bending actuation. Depending on which heating wires we distributed activated, the tube could bend towards six different directions (red color in Figure 2.8b indicates the activated heating wires). Similarly, by simultaneously applying the electrical potential to all the heating wires, the entire LCE tube was heated up, resulting in a homogenous contraction. The LCE tubular actuator recovered to its original shape and geometry after the electrical potential was turned off.

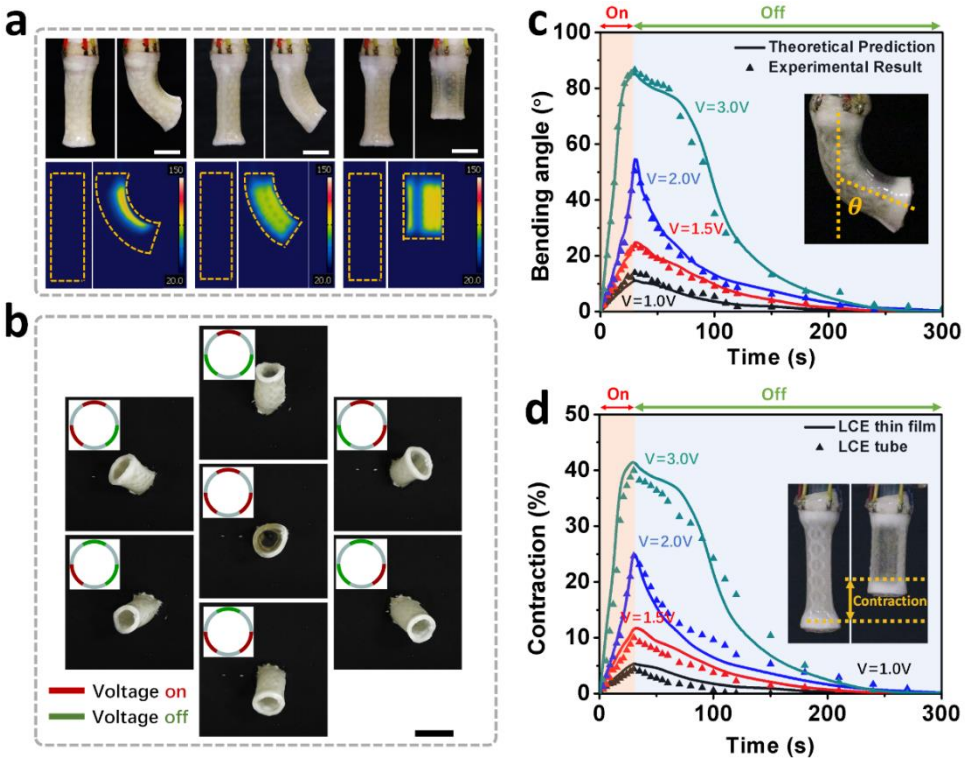

Figure 2.8: Multimodal actuation of an LCE-based tubular actuator. a Real and thermal image of an LCE tubular actuator during actuation: activating one or two heating wires resulted in bending motion; activating all three heating wires resulted in homogeneous contraction. **b** Different actuation modes of the tubular actuator. Six directional bending were realized by activating one or two heating wires. Contraction was achieved by simultaneously activating all three heating wires. **c** Plot of bending angle of LCE tubular actuator versus time by applying electrical potentials from 1.0 V to 3.0 V. The heating time was 30 s and the cooling time was 270 s. Solid lines represent theoretical prediction, and dots represent experimental results. **d** Plot of contraction of LCE tubular actuator versus time through the activation of all three heating wires, the electrical potential was set to 3.0 V and the time of electrical potential on was set as 30 s and the time of electrical potential off was set as 270 s. Solid lines represent theoretical prediction and dots represent experimental results. Scale bar in **a** and **b**: 1 cm.

Based on the measurement of the actuation strain on a single LCE artificial muscle thin film as described previously, we could quantitatively predict the bending angle of the LCE tubular actuator, as shown in Figure 2.8c. In the experiment, we applied different electrical potentials to

an LCE artificial muscle thin film for 30 s and then turned off the electrical potentials. We measured the actuation strain of the thin film as a function of time for different electrical potentials. The results are shown in Figure 2.8d, together with the contraction of the LCE tubular actuator when we applied the electrical potential was onto all three embedded heating wires. It can be seen that those two results are very similar to each other.

To predict the bending angle of the tubular actuator when we applied the electrical potential only onto one of the heating wires, we adopted the model developed for calculating the deflection of a beam caused by inhomogeneous thermal expansion [67]. As shown in Figure 2.9, when one of the three embedded heating wires was subjected to an electrical potential, we assumed one-third of the tubular actuator behaves just like the LCE artificial muscle thin film, and the other two third of the tubular actuator acts like passive elastic material. Therefore, the bending angle of the tube can be computed as $\theta = \frac{M_T}{I} l_0$, where l_0 is the length of the tube, $I = \frac{\pi}{64} E[(d_o)^4 - (d_i)^4]$, known as the bending stiffness of the tube with *E* as the modulus of the LCE and d_o and d_i as the outer and inner diameter of the tube, respectively, $M_T = \int \varepsilon_T Z dA$ as the thermal bending moment, with ε_T as the actuation strain of the thin film, and *Z* and *A* as denoted in Figure 2.9. With the input of the actuation strain ε_T measured for LCE thin film, as shown in Figure 2.8, the above equation allows us to predict the bending angle of the tubular actuator as a function of time. The prediction agrees very well with the experimental measurements, shown in Figure 2.8. We observed that both the length of the tube as well as the inner and outer diameters of the tube can be measured. There is no fitting parameter for the prediction.

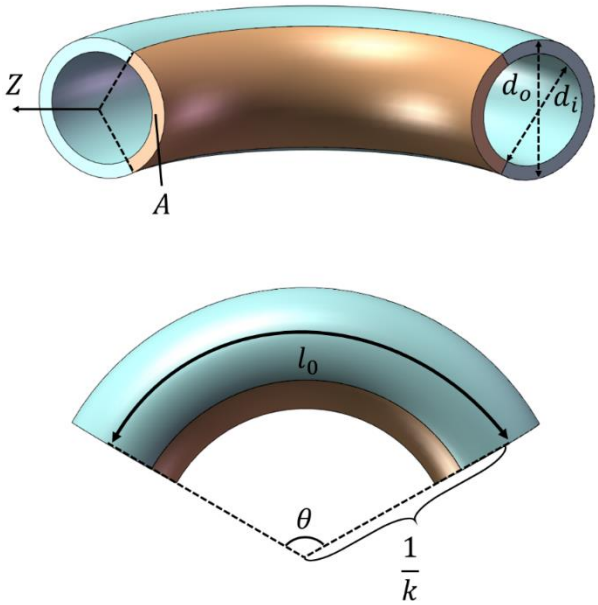

Figure 2.9: Theoretical prediction of bending angle of LCE tubular actuator through using the actuation of LCE artificial muscle thin film.

The position of the center of the unconstrained cross-section area of the tubular actuator is important to understand the actuation performance. We plotted the trajectory in Figure 2.10 (a and b), in which one or two heating wires were subjected to electrical potentials. The trajectory of the center points on the cross-section area of the tubular actuator, when we applied in one wire an electrical potential of 3.0 V for 30 s is shown in Figure 2.10a. When the power supply delivered the same electrical potential (3.0 V) for 20 s to two heating wires, the trajectories of the actuator's cross-section have the displacements shown in Figure 2.10a. When all three heating wires had the same electrical potential (3.0 V) for 30 s, we observed a homogeneous contraction.

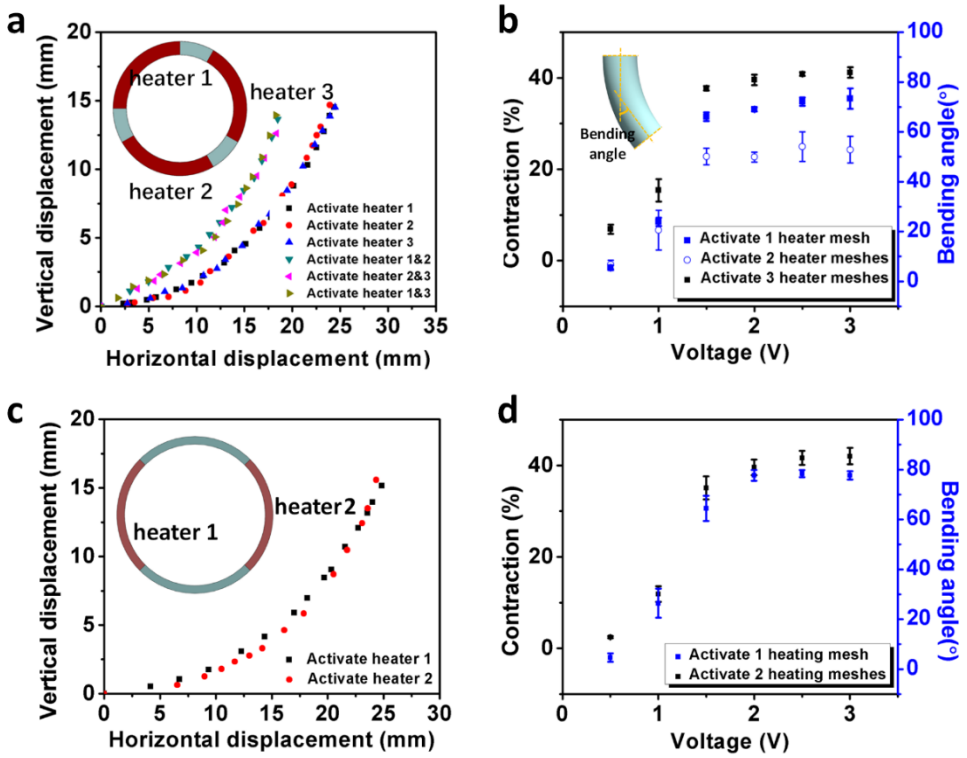

Figure 2.10: Characterizations of LCE tubular actuators (**a** and **b**: three heaters were embedded into the tubular actuator, **c,** and **d**: two heaters were embedded into the tubular actuator). **a** Trajectory of the center point of the bottom cross-section area through activating the individual heater. **b** Contraction and maximum bending angle of LCE tubular actuator with different applied electrical potentials. As we increased the electrical potential from 0.5 V to 2.0 V, both the contraction and maximum bending angle increased. As the electrical potential was further increased, the contraction and maximum bending angle maintained the same value. **c** Trajectory of the center point of the bottom cross-section area through activating individual heater. **d** Contraction and maximum bending angle of LCE tubular actuator with different applied electrical potentials. As we increased the electrical potential from 0.5 V to 2.0 V, both the contraction and maximum bending angle was increased. As the electrical potential was further increased, the contraction and maximum bending angle maintained the same.

Because of the thermal diffusion, when we applied high electrical potential (e.g. 3.0 V) to one heating wire or two heating wires, larger areas of the tube could be heated up if the heating time was too long (e.g., 360 s), which might induce unexpected geometrical distortion of the tube as

shown in Figure 2.11. To address this problem, we adopted the following strategy: we first applied a high electrical potential (V1=3.0 V) to the heating wires for 30 s to induce fast bending, and then the electrical potential was reduced to a lower value (V2=1.5 V) for the rest of time to maintain the deformation, as shown in Figure 2.11. We show the cyclic bending of the LCE tubular actuator in Figure 2.12, when we turned on and off, repeatedly, the electrical potential into one or two heating wires.

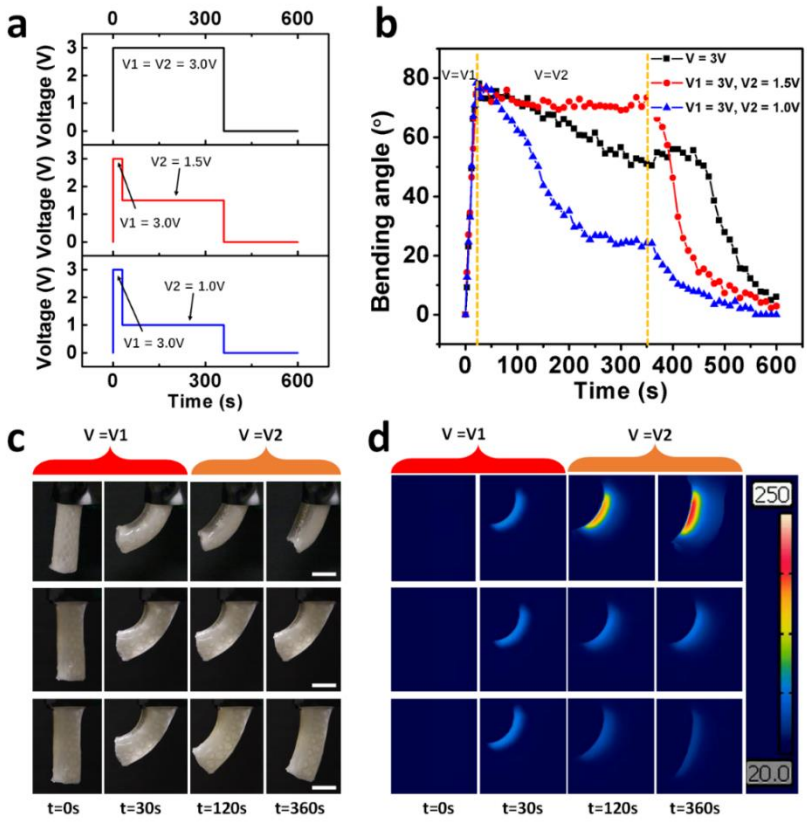

Figure 2.11: The actuation behavior of LCE tubular actuator with different voltage controls. **a** The time-dependent electrical potential control V1=3.0 V was applied to LCE tubular actuator for 30 s, and V2 (3.0 V, 1.5 V and 1.0 V) was applied to LCE tubular actuator for the following 330 s. Then the V2 was turned off. **b** The bending angle of the LCE tubular actuator was measured during the whole process. When the V2=3.0 V, the bending was increased to the maximum value at 30 s and was decreased due to the overheating. When the V2=1.5 V, the bending was increased to the maximum value at the 30 s, and it was maintained during the whole process. When the V2=1.0 V, the bending was increased to the maximum value at 30 s and was decreased due to the overcooling; **c** Images of LCE tubular actuator during the heating process. **d** IR images of LCE tubular actuator during the heating process.

Because of the internal heating mechanism of the tubular actuator, we further show that the LCE tubular actuator could also work effectively in a water environment (Figure 2.13) with

slightly increased electrical potential (6.0 V) due to the higher thermal conductivity and heat capacity of water as compared to air.

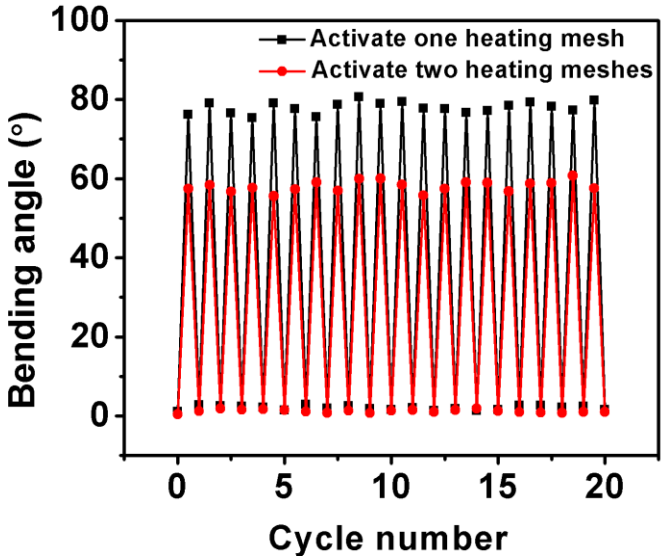

Figure 2.12: Cyclic test of LCE tubular actuator with different heating wires. An electrical potential of 3.0 V was applied to the heating mesh. For activating one heating mesh, the electrical potential was turned on for 30 s and off for 240 s. For activating two heating meshes, the electrical potential was turned on for 20 s and off for 240 s.

2.2.4 Soft gripper based on LCE-based tubular actuator

We next built a soft gripper, Figure 2.14, using the tubular actuator demonstrated previously as the main building block. As shown in Figure 2.14a, we could construct an electronically controlled soft gripper by using three tubular actuators. Three tubular actuators were first attached to a circular plate, which was further connected to an LCE artificial muscle film. We used a microcontroller to control the electrical potential applied to the actuator and thus, the deformation of each tubular actuator. By selectively activating the heating wires in each tubular actuator of the

gripper, the gripper can grasp and lift a vial (Figure 2.14c) and also twist its cap (Figure 2.14b) without additional external control.

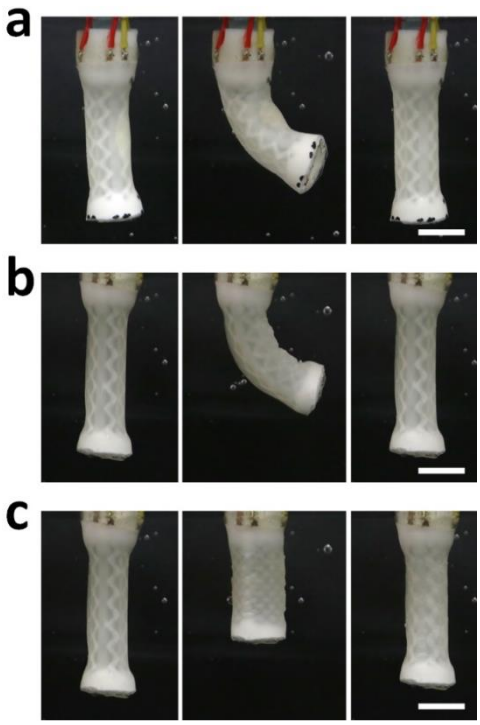

Figure 2.13: The reversible actuation (bending motion and contraction) of LCE tubular actuator in the water environment. The applied electrical potentials were 6.0 V.

2.2.5 An untethered soft robot

We next designed and fabricated the untethered robot using the LCE tubular actuators. We integrated a microcontroller (Arduino mini, 3.0 V), electrical components (MOSFETs, wires), battery (lithium/polymer, 3.7 V), LCE tubular actuators containing two separate heating wires (for the detailed characterizations, see Figure 2.10c and d) with an acrylic plate to build an untethered robot shown in Figure 2.15a.

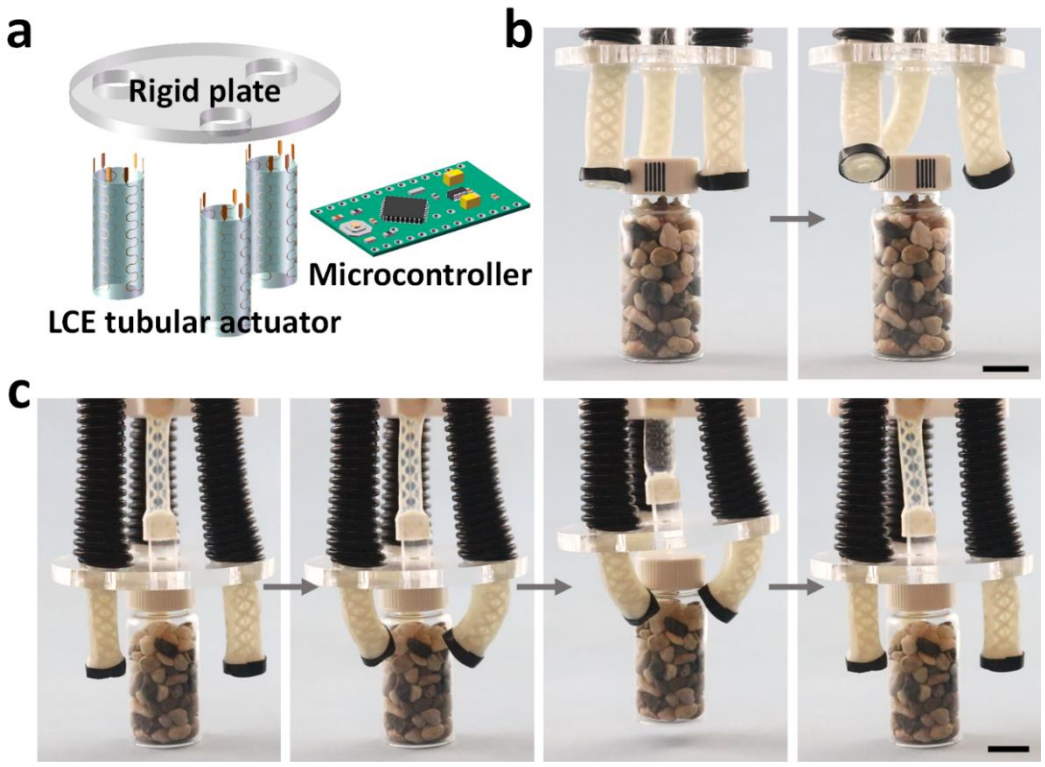

Figure 2.14: A multi-functional soft gripper composed of three LCE tubular actuators. a Schematic of the assembly of the soft gripper. **b** Soft gripper twisting the cap of a vial. **c** Soft gripper grasping and lifting the vial (50 g). Scale bar in **b** and **c**: 1 cm.

In Figure 2.15b, with automatically controlled LCE tubular actuators, the untethered robot can walk on a flat surface. The robot started to walk by simultaneously activating a pair of its diagonal tubular actuators for 17 s to bent forward. After that, the other pair of tubular actuators were activated simultaneously for 18 s. In the last step, the electrical potential was turned off for all the tubular actuators for 205 s, and all the actuators turned back to the original resting state. The displacement in one period was around 8.5 mm (see Figure 2.15d). After 30 min of walking, the robot can move forward for the distance about one body length (8 cm).

Figure 2.15c demonstrates three cycles of the untethered robot transporting an item on the top. In the experiment, we placed a cardboard on the top of the four tubular actuators, and a weight of 10 g on the plate. During the operation, the two front actuators first bent forward gradually using around 45 s and then recovered back to the straight state accompanied by contraction. During the recovery and contraction of the front actuators, the other two rear actuators bent forward also using about 45 s, which was followed by the state that the electrical potential was turned off for all the actuators. Such repetitive actions enabled the robot to move the rigid plate and the weight on the top of the plate, forward about 5 cm within 15 min, as shown in Figure 2.15d.

The cost of transports (COTs) is estimated as 5.0×10^4 and 1.0×10^5 for the robot walking and transporting experiments, respectively. Compared with other untethered soft robots [68], the magnitude of COTs of the LCE based untethered robot is very large, due to the low energy efficiency of thermally driven actuating materials.

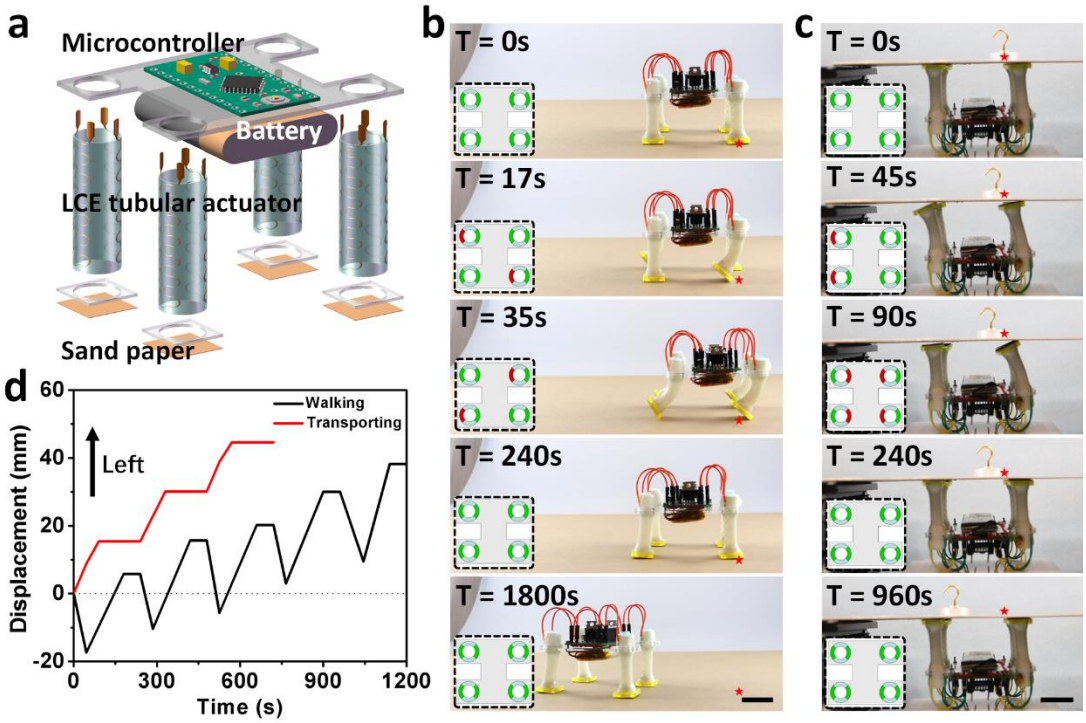

Figure 2.15: Electrically activated, untethered soft robot. a Schematic of the robot, mainly composed of a microcontroller, battery, four LCE tubular actuators. **b** Frames from a video of the robot walking. Walking began from rest (all the actuators were in the deactivated state), then a pair of diagonal tubular actuators were simultaneously activated for 17 s to bend forward. After that, the other pair of tubular actuators were activated simultaneously for 18 s. In the last step, the electrical potential to all actuators was turned off for 205 s, returning the actuators to their original states. **c** Frames from the video of the robot transporting an object on a plate of cardboard. During the operation, the two front actuators first bent forward for 45 s and then straightened without touching the top plate. During the straightening of the two front actuators, the two rear actuators bent forward for approximately 45 s, then the electrical potential to all the actuators was turned off. Repeating this sequence enabled the robot to move the rigid plate and the weight on top, forward about 5 cm within 15 mins. **d** Plot of displacement of the untether robot (black curve) and displacement of the item on the top plate (red curve) versus time. Scale bar in **b** and **c**: 2 cm.

2.3 Conclusion

In this chapter, we have discussed the design and fabrication of an LCE-based tubular actuator, which can exhibit multidirectional bending and homogenous contraction as a low electrical

potential is selectively applied to heating wires embedded in the LCE. Additionally, based on the tubular actuators, we have further constructed soft grippers which can grasp a vial and twist its cap. By integrating a battery, a microcontroller and the tubular actuators, we have built an untethered robot which can crawl on the ground and transport an item.

The distributed actuation of a tubular LCE caused the multimodal actuation of the soft tubular actuator developed in this article. Because of the embedded serpentine heating wires, we can fully activate the tubular actuator by an applying an electrical potential. Although LCE has been intensively explored in recent years to design and fabricate various novel structures and devices [11, 38, 69], the multifunctional robot based on the tubular actuators, to our knowledge, is the first untethered robotic system only using LCE as the actuating material.

Previous work in electrically-controlled soft-structures such as most dielectric elastomer actuators (DEAs) has shown much faster speed and higher energy efficiency, compared to the LCE-based tubular actuators developed in this article [70]. However, the LCE-based tubular actuator does not require any stiff frames to maintain large pre-stretch for achieving large actuation. Furthermore, the tubular actuator also uses a low-voltage power source, (around 3 orders of magnitude lower than the electrical potential required to actuate DEAs). This feature makes our tubular actuator compatible with most low-cost, commercially available electronic devices and batteries.

Chapter 2, in full, is a reprint of the material as it appears in “Electrically controlled liquid crystal elastomer-based soft tubular actuator with multimodal actuation”, *Science advances* 5 (2019): eaax5746, by Qiguang He, Zhijian Wang, Yang Wang, Adriane F. Minori, Michael T. Tolley and Shengqiang Cai. The dissertation author was the primary investigator and first author of this paper.

Chapter 3 Bioinspired design of vascular artificial muscle

3.1 Introduction

Soft and stretchable actuators, which are also often called artificial muscle, have been widely employed in the applications ranging from soft robotics [1, 3, 71], biomimetic systems [32, 47, 72] to wearable devices [73, 74]. Recently, various materials and structures have been explored as artificial muscle with different characteristics [6, 75-79]. For instance, dielectric elastomer films can generate fast and large deformation when subjected to electrical voltage [6]; shape memory polymer can change shapes upon the change of temperature [78]; environmentally-sensitive hydrogels can significantly swell or shrink when exposed to different external stimuli such as the variation of temperature and pH value in a solution [75]. Large actuating stress and strain have been recently demonstrated in thermally-powered twisted fish-line artificial muscle [80, 81]. Various balloon-like structures have also been intensively explored as pneumatic and hydraulic artificial muscle in soft robots [9, 82, 83].

Though tremendous success has been achieved in the applications of those materials as artificial muscle, certain limitations have also been well recognized. For example, ultra-high voltage is often required to actuate a thin dielectric elastomer film [76]; Special designs are often required for soft pneumatic/hydraulic actuators to generate high-force output [84, 85]. Significant reduction of the size of twisted fish-line artificial muscle can be technically challenging.

Liquid crystal elastomer (LCE), as a newly emerging soft actuating material, has recently received much attention [11, 14, 21, 33, 38, 54, 57, 61, 86-88]. Based on the molecular structure, LCE can be simply viewed as an integration of mesogenic molecules into a polymer network (Figure 3.1). When the temperature of the LCE is increased above a critical temperature (also called isotropic transition temperature), the mesogens can transit from liquid crystal phase to isotropic phase, which may lead to large and reversible deformation of the elastomer. It has been shown that both actuating strain and stress generated by an LCE can be comparable to real mammalian skeletal muscle [62]. In addition, using different fabrication techniques such as 3D printing [89] and photo-lithography [61], active LCE structures of various sizes have been successfully fabricated.

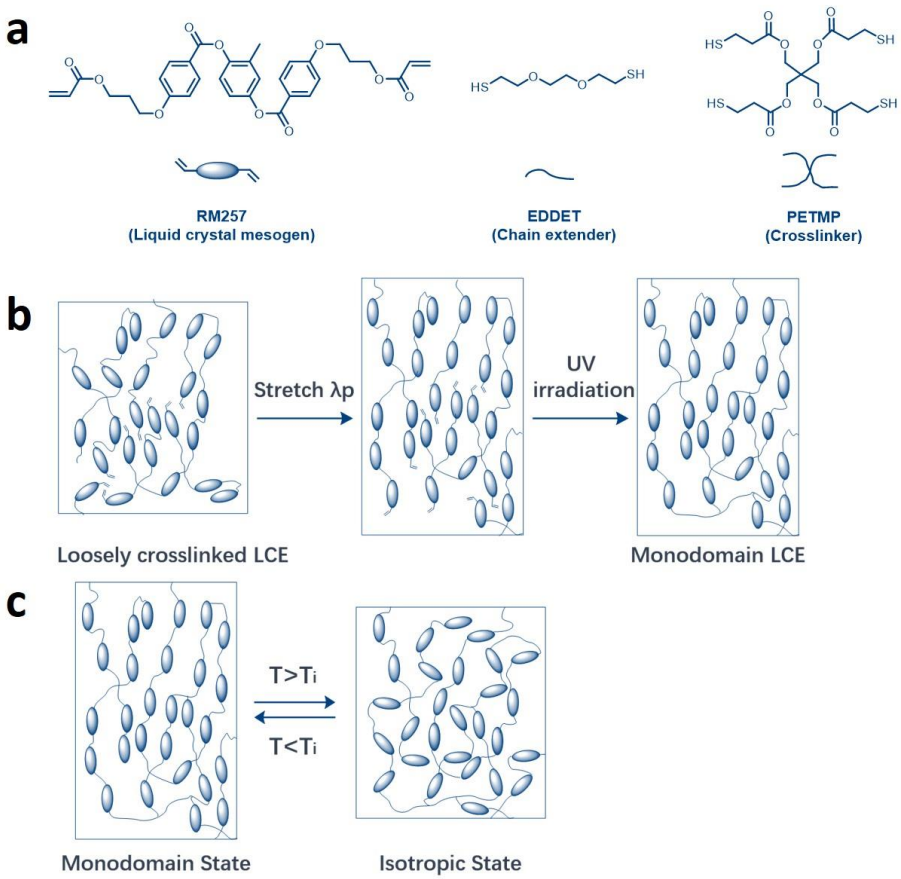

Figure 3.1: Chemical components for synthesizing LCE: RM257 is liquid crystal mesogen, EDDET is chain extender, and PETMP is crosslinker. **b.** Monodomain LCE can be obtained by stretching loosely crosslinked LCE to align the liquid crystal mesogen. The LCE can be fixed in monodomain state when it is exposed to UV irradiation to stimulate the second-step crosslinking reaction. **c.** LCE contracts once its temperature is increased above the isotropic transition temperature T_i, because liquid crystal mesogens transit from nematic phase to isotropic phase.

In practical uses of LCE as artificial muscle in the structures with complex forms, it is often essential to integrate heating element into the material [90]. For instance, Thomsen et al. fabricated a multilayer LCE structure with embedded flexible heating element, where low-voltage induced large deformation has been achieved. In most previous studies, resistance heating wires have been embedded into LCE, and Joule heating generated by the resistance heating wires can induce the

actuation of the material. As a matter of fact, using embedded resistance heating wires to generate thermal actuation have been explored in many different thermally-actuating materials including shape memory polymers [91], temperature-sensitive hydrogels [5], and fish line artificial muscle [92]. However, such experimental setup may have several drawbacks: First, the heating wires are typically metallic, which may constrain the stretchability and also increase the overall stiffness of the actuating material; second, for those thermally-actuating materials, they are often required to recover to their initial states after being cooled down for a subsequent actuation cycle. Compared to heating up, cooling down is generally more challenging to control. So far, few efforts have been made to achieve active and fast cooling of those materials. Consequently, in most of the previous experiments, passive and external air cooling is adopted, which is typically very slow and can greatly depend on the environmental temperature as well as the ventilating conditions.

Nevertheless, for real muscle in biology, to maintain their normal physiological activities, both the supply of oxygen and nutrients and removal of waste such as carbon dioxide [93, 94] should be highly efficient. In addition, most mass transport processes in biological system are through slow diffusion. To enable fast mass transport, the strategy adopted in nature (for both animals and plants) is to develop vascular structure (see Figure 3.2a as an example [95]). Inspired by the prevalence of the vascular structure in biology, in the article, we design a vascular LCE-based artificial muscle (VLAM). We inject hot and cool water into its internal fluidic channel to realize both fast thermal actuation and recovery. Because of the internal heating and cooling, the VLAM shows very robust actuation performance within a wide range of environmental temperature.

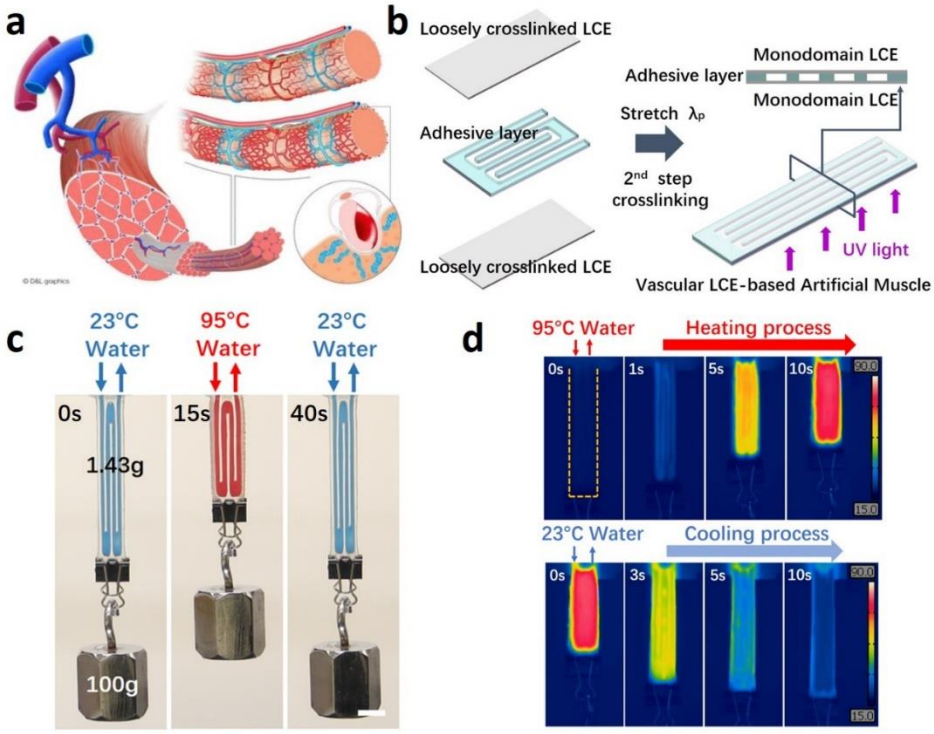

Figure 3.2: Design, fabrication and performance of vascular LCE-based artificial muscle (VLAM). a Vascular structure of a real muscle bundle. **b** Fabrication procedure of VLAM: one adhesive layer (with laser-cut water channel) is first sandwiched between two layers of loosely crosslinked LCE films; the entire structure is then stretched by λ_p and exposed under UV irradiation to form additional crosslinks in the LCE films. **c** Reversible actuation of VLAM: VLAM of 1.4 grams can lift up a weight of 100 grams by 40% contracting strain with the injection of 95°C circulated water (dyed red) and lower down the load with the injection of room-temperature circulated water (23°C). Scale bar: 1cm. **d** Thermal imaging of VLAM during the contraction and recovery process.

3.2 Results and discussion

3.2.1 Design and fabrication of VLAM

We fabricate the VLAM following the steps as sketched in Figure 3.2b. The VLAM is composed of three layers. Both the top and bottom layers are monodomain LCE thin films (liquid crystal mesogens are well aligned in the film in stress-free state), while the middle layer is an

adhesive thin film (VHB tape, 3M) with fluidic channel which is made by high-precision laser cutting (Universal laser systems).

To fabricate the VLAM, we first synthesize two loosely crosslinked polydomain LCE films, which are then bonded by an adhesive layer (VHB tape from 3M company) with laser-cut fluidic channels. The detailed synthetic procedures of the LCE film are described in the experimental section. We then pre-stretch the entire structure by λp times of its original length to induce the polydomain-to-monodomain transition of the LCE and place it under UV irradiation to induce second crosslinking reaction in the LCE to fix it in monodomain state (Figure 3.2b). In the following experiments, the prestretch ratio λp is set to be 3 unless otherwise specified.

It is known that monodomain LCE can exhibit reversible thermal-actuation with or without externally applied stress. When the temperature is above the isotropic transition temperature, well-aligned mesogens in the LCE can transit to isotropic state, resulting in macroscopic contraction of the elastomer along the aligning direction of mesogens. In the experiment, to increase the temperature of the VLAM, we inject hot water into its internal fluidic channel as shown in Figure 3.2c. The temperature of the hot water (dyed red) in the test is 95^{o}C with the flow rate of 1.50 mL/s. The VLAM with a weight of 1.43 grams can contract by 40% of its initial length and lift a weight of 100 grams within 10 seconds as shown in Figure 3.2c.

To enable the VLAM to recover to its initial length, we inject water of room temperature (dyed blue) into the internal fluidic channel. In contrast to external and passive cooling method used in most previous studies, we here adopt internal and active cooling method to lower down the

temperature of the VLAM. As shown in Figure 3.2c, the artificial muscle recovers to its initial length also around 10 seconds, which is much faster than the external and passive air cooling. Compared to other method to induce active deformation of LCEs such as light and resistance heating wires, using circulating water provides another potential advantage: the artificial muscle can keep its high transparency during the entire actuating process as shown in Figure 3.3.

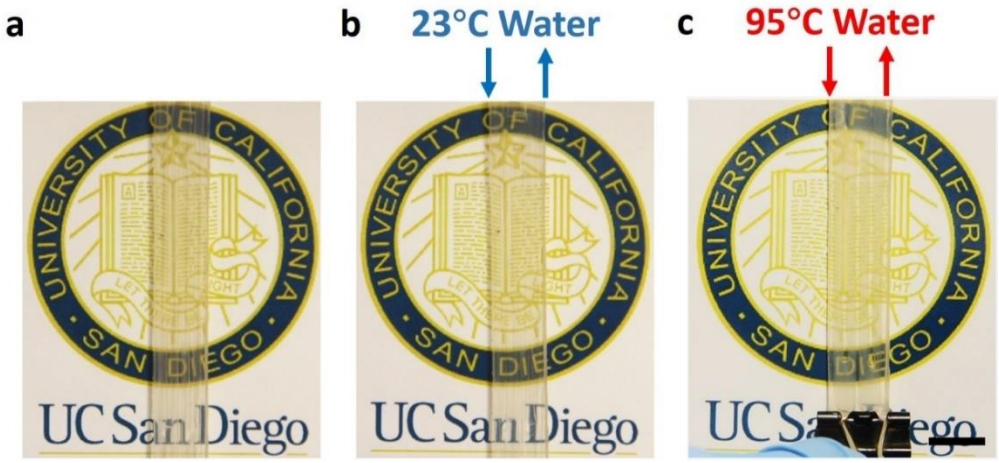

Figure 3.3: VLAM is transparent during the entire actuation process. a. The initial state of VLAM. **b.** Water at room temperature is injected into the internal fluidic channel of VLAM. **c.** Water at 95^0C is injected into the internal fluidic channel of VLAM. Scale bar: 1cm.

During the process of injecting water into the VLAM, we use thermal imaging technique (FLIR E75-42 Advanced Thermal Imaging Camera) to further examine the temperature of the surface of VLAM as shown in Figure 3.2d. When we inject hot water of 95 ^{o}C into the fluidic channel of the artificial muscle, the surface temperature of the structure increases from 20 ^{o}C to 85 ^{o}C within 10 seconds and then maintain as a constant, indicating the temperature field in the

material reaches a steady state. Likewise, the temperature decreases from 85 ^{o}C to 20 ^{o}C also within 10 seconds, when water of room temperature is injected into the VLAM.

3.2.2 Characterizations of VLAM

We next quantitatively characterize the dynamics of actuation of VLAM. In the experiment, we first measure the actuation strain of a free-standing VLAM with the injection of hot water into its internal fluidic channel. The results are shown in Figure 3.4a. The actuation strain increases rapidly and reaches a plateau value within 8 seconds after the injection of hot water at 95 ^{o}C with the flow rate of 1.50 mL/s. When the actuation strain reaches the plateau, the VLAM reaches a steady state. Depending on the temperature of the injected water, the plateau value varies. After the actuation strain stays at the maximal value for tens of seconds, we inject water of room temperature (23 ^{o}C) into VLAM with the flow rate of 1.50 mL/s. As shown in Figure 3.4b, around 15 seconds after the injection of cool water, the VLAM recovers to its initial state, which is much faster than the passive and external air cooling as also shown in Figure 3.4b for comparison. As discussed previously, slow recovery process often limits the applications of most thermally-driven artificial muscle.

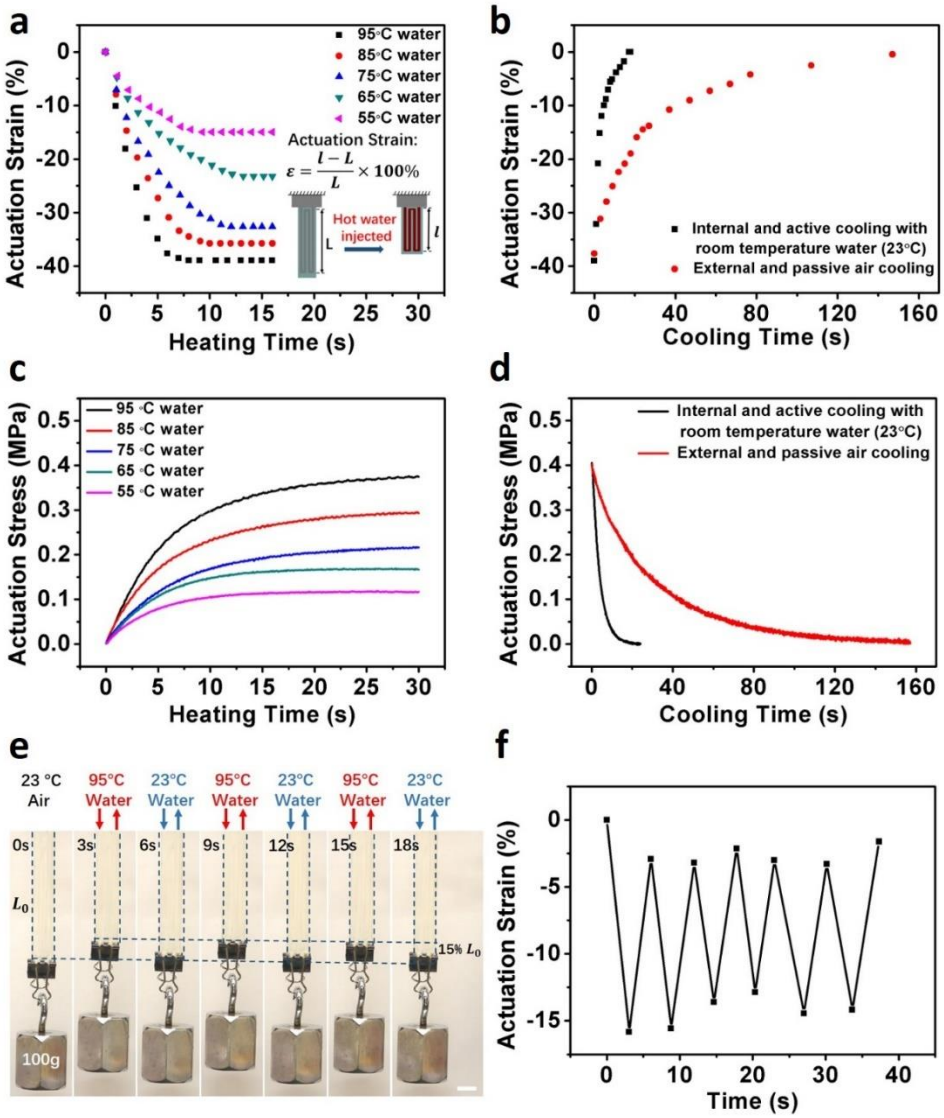

Figure 3.4: Fast actuation and recovery of VLAM. a. Actuation strain of a free-standing VLAM as a function of time with the injection of water at several different temperatures. **b**. Recovery of an actuated free-standing VLAM as a function of time through internal and active cooling with room-temperature water and through external and passive air cooling. **c**. Actuation stress of VLAM with fixed length as a function of time with the injection of water at several different temperatures. **d**. Stress relaxation of an actuated VLAM with fixed length as a function of time through internal and active cooling with room-temperature water and through external and passive air cooling. e and f. Fast cyclic actuation and recovery of a VLAM attached to a weight of 100 gram, with the alternative injection of room-temperature water and hot water. Scale bar in e is 1cm.

By fixing its original length, we can also measure the actuating stress generated by the VLAM when hot or cool water is injected into it. Similar to the change of actuation strain, as shown in Figure 3.4c, the actuation stress increases rapidly from zero to a maximal value within 30 seconds. The maximal actuating stress also depends on the temperature of the hot water. The actuation stress quickly relaxes to zero (within 15 seconds) when we inject cool water into the structure as shown in Figure 3.4d.

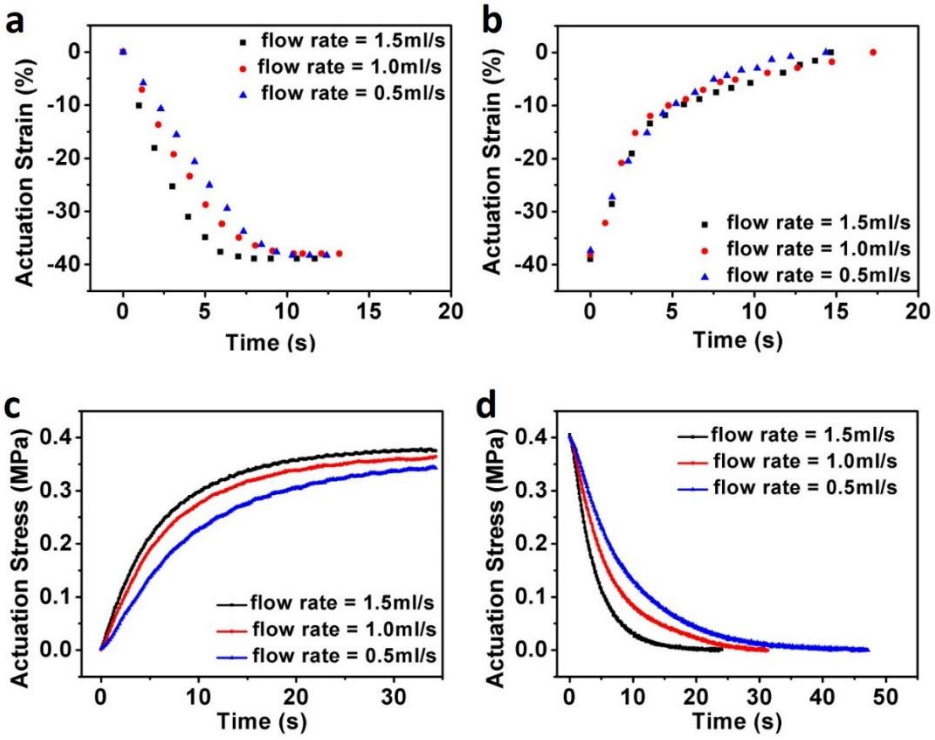

Figure 3.5: Flow rate effects to the responsive speed of VLAM. a. Actuation strain of a free-standing VLAM as a function of time with the injection of water (95 ^{o}C) at three different flow rates. **b.** Recovery of an actuated free-standing VLAM as a function of time through internal and active cooling with room-temperature water at three different flow rates. **c.** Actuation stress of VLAM with fixed length as a function of time with the injection of water (23 ^{o}C) at three different flow rates. **d.** Stress relaxation of an actuated VLAM with fixed length as a function of time through internal and active cooling with room-temperature water at three different flow rates.

In addition to the temperature of the water, we also study the effect of flow rate of the water on the actuating performance of VLAM. The results are shown in Figure 3.5. In the experiment, the temperature of the hot water is fixed at 95 ^{o}C and the cool water is fixed at room temperature, and we use three different flow rates: 1.5mL/s, 1.0mL/s and 0.5mL/s. With the increase of the flow rate, both the thermal actuation and recovery of VLAM are faster. The flow rate of water has negligible influence on the magnitudes of actuating stress and actuating strain of VLAM in steady state.

By alternatively injecting room-temperature water and hot water into VLAM, we further demonstrate that the frequency of cyclic actuation (with an actuation strain of 15%) of VLAM can be easily achieved at around 0.2 Hz as shown in Figure 3.4e and f, without detailed structural optimization and using fluids at extreme temperatures. According to our knowledge, such cyclic response rate is significantly faster than most thermally-actuating materials with similar level of actuation strain and size, reported in the previous studies [69]. In addition, the cyclic response rate of VLAM is also close to that of mammalian skeletal muscle [93]. It is also noted that we did not detect any water leakage or film delamination after 30 cycles of actuation.

The actuation performance of VLAM strongly depends on the pre-stretch ratio λp during the second crosslinking step of the LCE (Figure 3.2b). To study such dependence, we pre-stretch loosely-crosslinked LCE films by λp of three different values: 2.0, 2.5, 3.0, and then crosslink the film under the illumination of UV light during the fabrication procedure as shown in Figure 3.2b. We measure the actuation strain and stress of VLAM in the steady state with the injection of water

at different temperatures (from 40 ^{o}C to 95 ^{o}C). We plot the experimental measurements of actuation strain and stress in Figure 3.6a and b. With the increase of the pre-stretch λ_p or the temperature of the injected water, the magnitude of both actuation strain and actuation stress increase. In particular, as the temperature of water is increased from 40 ^{o}C to 95 ^{o}C, the magnitude of actuation strain increases from 7% to 40%, and the magnitude of actuation stress increases from 0.1MPa to 0.4MPa for VLAM with the pre-stretch λ_p=3. Both actuation stress and strain are comparable to those of mammalian skeletal muscle (with actuation strain ranging from 20% to 40% and actuation stress ranging from 0.10 to 0.35 MPa). It is also worth to mention that the actuation strain of VLAM is almost identical to a single monodomain LCE sheet with the same pre-stretch λ_p (Figure 3.7), implying that the embedded fluidic channel does not place any restriction on the actuation capacity of active LCE films.

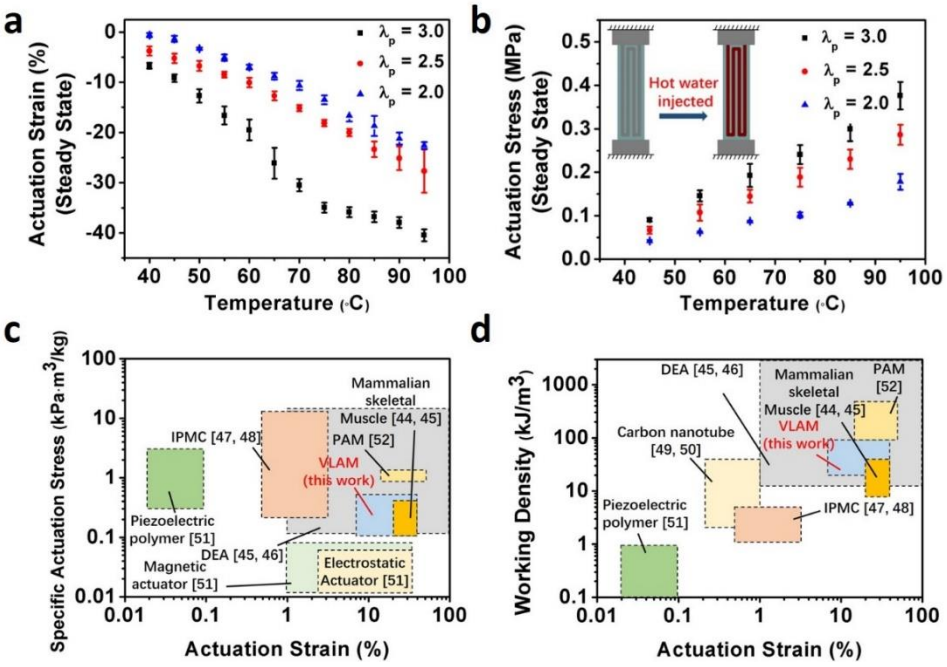

Figure 3.6: Actuation performances of VLAM at steady state. a Actuation strain of free-standing VLAM as a function of temperature, for three different pre-stretch ratios of the VLAM: λ_p= 2.0, 2.5 and 3.0, during its preparation. **b** Actuation stress of VLAM with fixed length as a function of temperature for three different pre-stretch ratios of the VLAM: λ_p= 2.0, 2.5 and 3.0, during its preparation. **c** Specific actuation stress versus actuation strain of several widely-used actuating materials and mammalian skeletal muscle. **d** Working density versus actuation strain of several widely-used actuating materials and mammalian skeletal muscle. Abbreviation: VLAM-vascular LCE-based artificial muscle. IPMC-ionic polymer metal composite, DEA-dielectric elastomer actuator. PAM- pneumatic artificial muscle.

In Figure 3.6c, we plot the specific actuation stress (actuation stress divided by density) versus the magnitude of actuation strain of VLAM based on the measurements in Figure 3.6a, b, together with other widely-used actuating materials and mammalian skeletal muscle. In Figure 3.6d, we plot the working density of the VLAM based on the experimental measures shown in Figure 3.2c and Figure 3.8, in which we hang weight of 100g and 500g at the bottom of a VLAM, respectively, and measure the corresponding contracting distance of the artificial muscle with the injection of

hot water of 95 ^{o}C. We find that in terms of the performance metrics in Figure 3.6c, d, VLAM is comparable to mammalian skeletal muscle. VLAM also has similar actuation performance as currently-leading artificial muscle materials: dielectric elastomer and pneumatic artificial muscle. Considering many other advantageous features, VLAM can be regarded as excellent supplement to all the currently available artificial muscle materials for various applications.

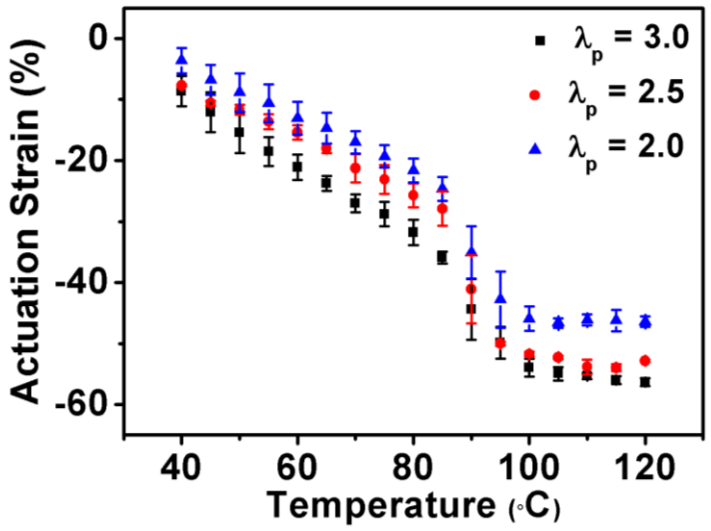

Figure 3.7: Actuation Strain versus temperature of a free-standing LCE film with the pre-stretch λ_p (during its synthesis procedure) equal to 2.0, 2.5 and 3.0. Larger actuation strain can be generated by larger pre-stretch ratio and higher temperature.

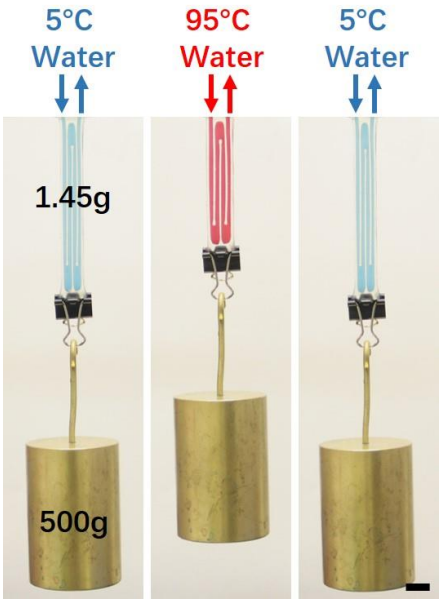

Figure 3.8: A VLAM of 1.45g can lift up a weight of 500g by 30% of the initial length of the VLAM with the injection of water at 95 °C. Working density of the VLAM is calculated as the work done by it divided by its volume. In this case, the work done by VLAM is around 0.0882J, and the volume of VLAM is 1.026e-6 m^3, which results in the working density as 86kJ/m^3. Scale bar: 1cm.

3.2.3 Broad operation temperature of VLAM

Performance of most thermally-driven artificial muscle can strongly depend on the environmental temperature. Thanks to the internal cooling and heating mechanism, another important advantage of VLAM developed in this article is its broad range of working temperature. In the experiment, we submerge a VLAM into a large water tank with temperature ranging from 5°C to 80°C as shown in Figure 3.9a, b. It is noted that thermal contraction in an LCE film becomes noticeable when its temperature is above 40 °C and reaches maximum when the temperature is 80 °C. Consequently, in our experiment, when the VLAM is put into the water tank of temperature above 40 °C, it shortens immediately. We plot the ratio of the length of the VLAM in the air (Lair)

and in the water tank (Lw) of different temperatures in Figure 3.9c. It clearly shows that in the water tank of 80 ^{o}C, the artificial muscle can contract as much as 40%. We then alternatively inject hot water (95 ^{o}C) and cool water (5 ^{o}C) into the VLAM to investigate its actuating behavior. We plot the length of the artificial muscle Lc (normalized by Lair) in the steady state with the injection of cool water in Figure 3.9d. We also plot the actuation strain of the VLAM in Figure 3.9, which is defined as (Lc- Lh)/ Lc, where Lh is the length of VLAM in the steady state with the injection of hot water. As we can see from Figure 3.9d, the magnitude of the actuation strain is roughly a constant for the entire range of experimental temperature (5^{o}C to 80^{o}C).

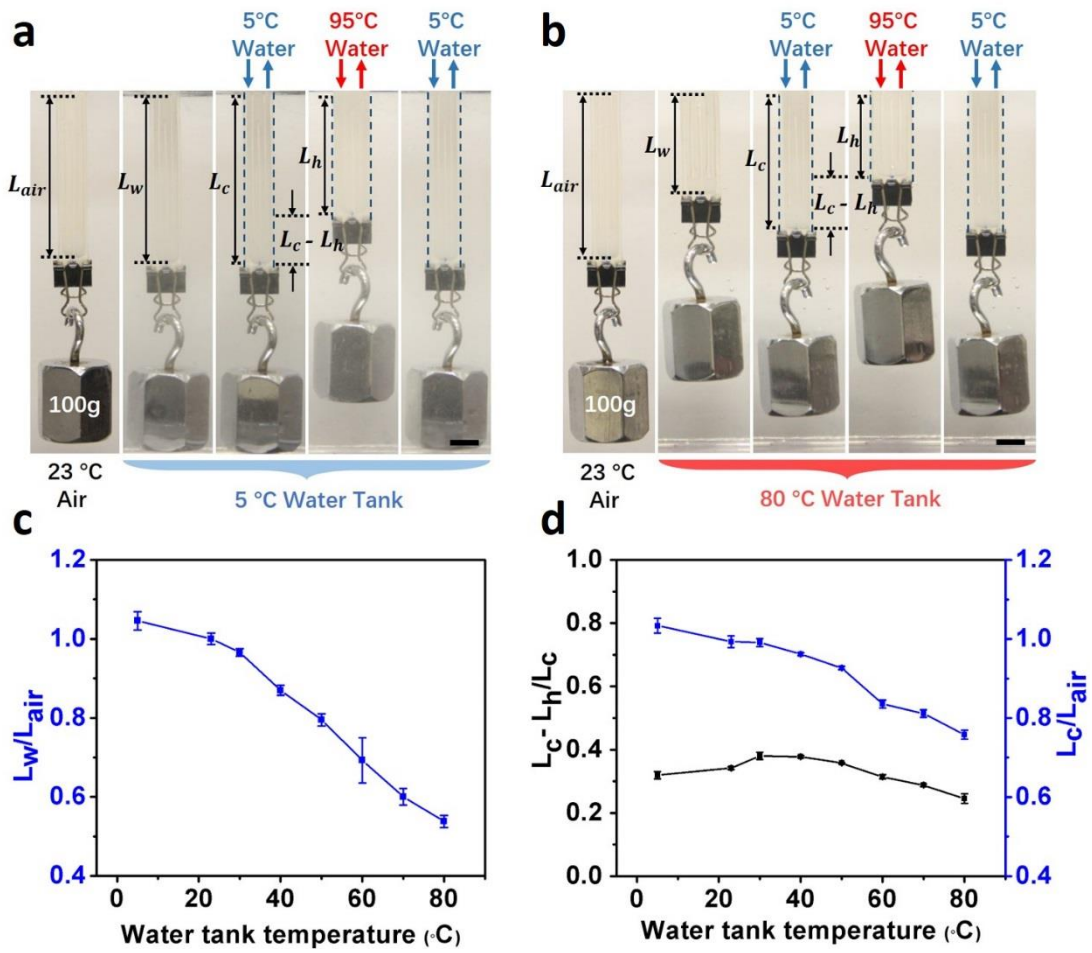

Figure 3.9: Actuation of VLAM in a wide range of environmental temperature. a Reversible actuation of a VLAM in cold water (5°C). **b** Reversible actuation of a VLAM in hot water (80°C). **c** Length of a VLAM (normalized by its length in the air) in a water tank at different temperatures. **d** Length of a VLAM in a water tank with the injection of cold water (5 °C), and the actuation strain of the VLAM with injection of hot water (95°C). The magnitude of actuation strain only weakly depends on the environmental temperature indicating the high robustness of the system. Scale bar in a and b are: 1cm.

3.2.4 Potential demonstration of VLAM

As a final demonstration, we use VLAM to drive different modes of motion of a skeleton model. The attachments of artificial femoris, biceps, triceps and masseter muscles onto the

skeleton are shown in Figure 3.10. With hot water (95 ^{o}C) injected to the artificial masseter muscles, they contract, move the jaw up and close the mouth. The mouth can quickly open with cold water being injected into the artificial masseter muscle. The bending movement of elbow can be controlled by two separate muscles: biceps and triceps. We simultaneously inject hot and cool water into artificial biceps and triceps muscles, respectively. The biceps contract and triceps relax, which moves the arm to bend at elbow. Alternately injecting hot and cool water can generate cyclical movement of the arm. The artificial muscle can also be used as biceps femories to control the movement of the shank of the skeleton.

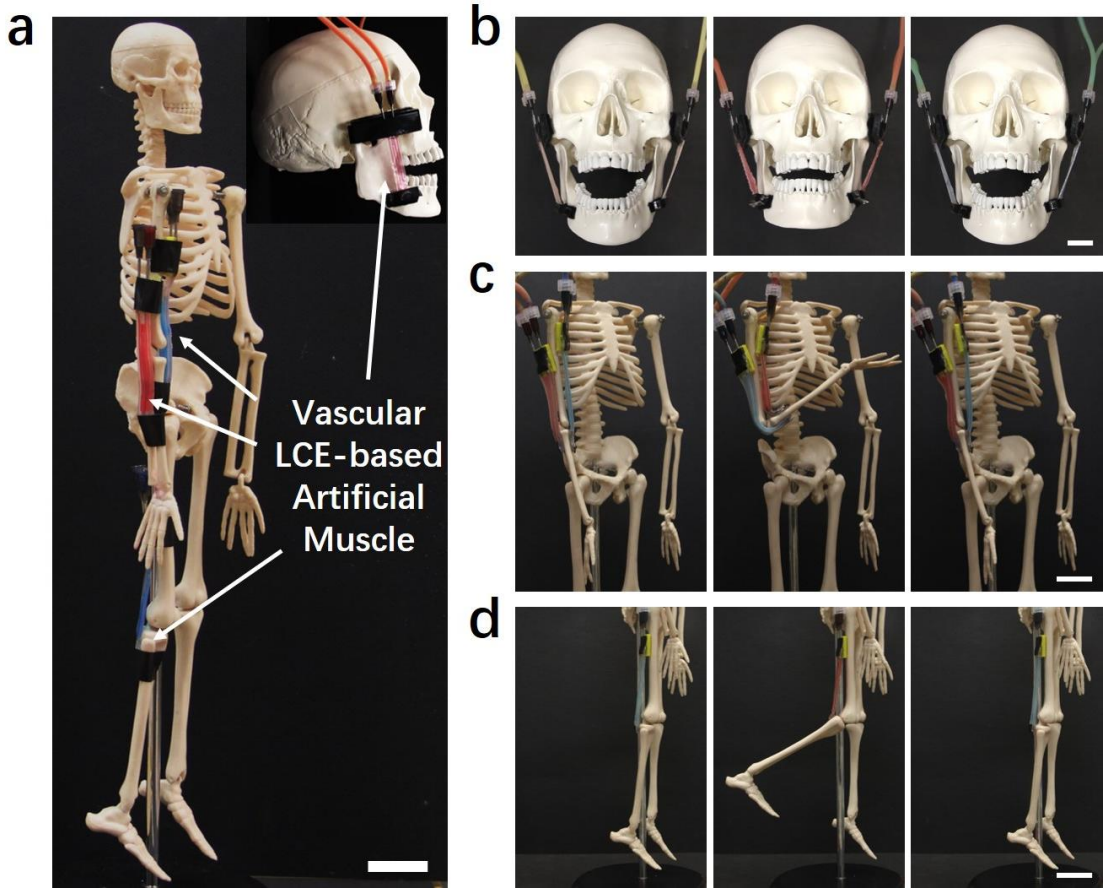

Figure 3.10: Potential applications of VLAM. **a**. Demonstration of the implementation of VLAM as biceps femoris artificial muscle, biceps artificial muscle, triceps artificial muscle and masseter artificial muscle on a human skeleton. **b**. Jaw movement by contraction of artificial masseter muscle. **c**. Lift of an arm by the contraction of artificial biceps muscle and relaxation of artificial triceps muscle. **d**. Lift of a shank by the contraction of artificial biceps femoris muscle. The scale bars in all the figures are 2cm.

3.3 Conclusion

In summary, in this chapter we demonstrate a bioinspired design of a vascular LCE-based artificial muscle, which exhibits large actuation strain and stress in a fast-cyclic response rate. In many aspects, the actuating performance of the artificial muscle is comparable to real mammalian skeleton muscles. Thanks to the internal heating and cooling by circulated water, the newly

developed artificial muscle can work in a broad range of environmental temperature while maintain robust performance. We further demonstrate the application of the vascular artificial muscle in driving various movements of a skeleton. Last, we would like to point out that the fluid-driven vascular artificial muscle developed in this article may provide an effective way to make use of waste heat generated in different processes. Although in this article, we only demonstrate the advantages of the vascular structure in the LCE-based artificial muscle, similar ideas should be applicable to most thermally-actuating materials of various kinds.

Chapter 3, in full, is a reprint of the material as it appears in “Bioinspired design of vascular artificial muscle”, *Advanced Materials Technologies* 4 (2019): 1800244, by Qiguang He, Zhijian Wang, Zhaoqiang Song and Shengqiang Cai. The dissertation author was the primary investigator and first author of this paper.

Chapter 4 Recyclable and self-repairable fluid-driven liquid crystal elastomer actuator

4.1 Introduction

Soft robots exhibit versatile unique features compared with their stiff counterparts, such as continuum deformation, excellent adaptabilities, high impact resistance and benign human-robot interfaces [1, 96]. In this context, various soft responsive materials and deformable structures have been explored to make soft actuators, including pneumatically/hydraulically inflating structures [2, 9], stimuli responsive hydrogels [97] , dielectric elastomer actuators (DEAs) [6, 44, 76] and shape memory polymers (SMPs) [7]. Recently, liquid crystal elastomer (LCE) has emerged as a promising soft actuating material due to its capability of generating large and reversible actuation via liquid crystal-isotropic phase transition [98]. It has been shown in previous studies that the liquid crystal-isotropic phase transition can be stimulated by heat and light through photothermal or photochemical reactions [27, 98, 99]. Spatially patterned orientation of liquid crystal molecules (mesogens) in an LCE structure can result in versatile actuation modes such as contraction [29, 100], bending [11, 59, 101], rolling [102, 103], crawling [12, 104], jumping [31] and oscillating [105], which have further stimulated widespread interests.

However, grand challenges still exist in constructing LCE-based soft robots and devices, which need to be addressed for their broader applications. First, achieving easily controllable actuation of LCE-based actuator is often not trivial. In previous studies, environmental heating has

been widely adopted for many demonstrations of LCE-based structures, which, however, is not feasible for most practical applications. Light-powered LCE-based actuators have also been intensively explored, which have their own limitations such as poor scalability and maneuverability of the light source. Another straightforward strategy to generate controllable actuation is to embed metallic heating wires into LCE [23, 24]. Joule heating generated in the metallic wires can trigger the deformation of the actuator. However, incorporating metallic wires may constrain the stretchability of the entire structure and affect its overall stiffness. In addition, the embedded metallic wires or other heating elements often hamper the recycling of the actuator, which has been regarded as a potential advantage of polymer-based actuators, as compared to other traditional ones. Second, another well-known concern of using LCE-based soft actuator is its slow actuation speed because of the low thermal conductivity of LCE as well as the passive external cooling mechanism. Although our previous works have demonstrated that vascular LCE-based actuator can generate approximately 15% cyclic contraction at 0.17 Hz, the actuation bandwidth is still significantly lower than most animal muscle (> 1 Hz) [25]; in addition, delamination is often detected in the previously developed vascular LCE-based actuator, due to the weak bonding at the interface between each layer in the structure.

Recent advancements in the chemistry of LCEs have provided us great opportunities to address these challenges mentioned above [106]. In particular, previous studies have shown that the incorporation of dynamic covalent bonds, such as disulfide bonds [21, 22], ester bonds [57, 107] and ally sulfide groups [108] into LCE could make it self-healable, reprogrammable,

reconfigurable, recyclable and reusable. Subjected to certain external stimuli, the dynamic covalent bonds can undergo bond exchange reaction, enabling the rearrangement of polymer network as well as the combination of two or multiple pieces of LCE into a single piece without weak interfaces [21].

Here, through the combination of disulfide LCE material and fluidic architecture, we develop a novel fluid-driven LCE soft actuator through laminate manufacturing approach enabled by bond exchange reaction, termed as fluid-driven ss-LCE soft actuator. We demonstrate that the newly constructed fluid-driven ss-LCE actuator has the following features: 1) rapid cyclic response, 2) good durability, 3) self-repairability, 4) recyclability, 5) broad operating temperature range and 6) programmability. Using the novel ss-LCE based actuators as building blocks, we have further explored soft grippers and soft locomoting robots that can be programmed to realize manipulating and crawling.

4.2 Results and discussion

4.2.1 Design and fabrication of fluid-driven ss-LCE actuator

The used ss-LCE is synthesized following the procedures reported in our previous study [22]. As shown in Figure 4.1a, RM257 serves as the liquid crystal mesogen, HDT is the chain extender and PETMP acts as crosslinker. The disulfide groups (R-S-S-R´) are introduced through the oxidation between thiol groups, endowing the self-healing capability of the synthesized LCEs. Self-healing is achieved through disulfide exchange reaction (Figure 4.1b) at elevated temperature

(180 °C) to bond cracked surfaces together. To verify the self-healing capability of ss-LCE, we cut a long strip LCE thin film into two pieces and then bring them into contact for 1 hour at 180 °C, during which dynamic exchange reaction occurs (Figure 4.1c)). After exchange reaction, the two pieces of LCE films can be firmly bonded with each other, which is verified by the uniaxial tension test as shown in Figure 4.1d.

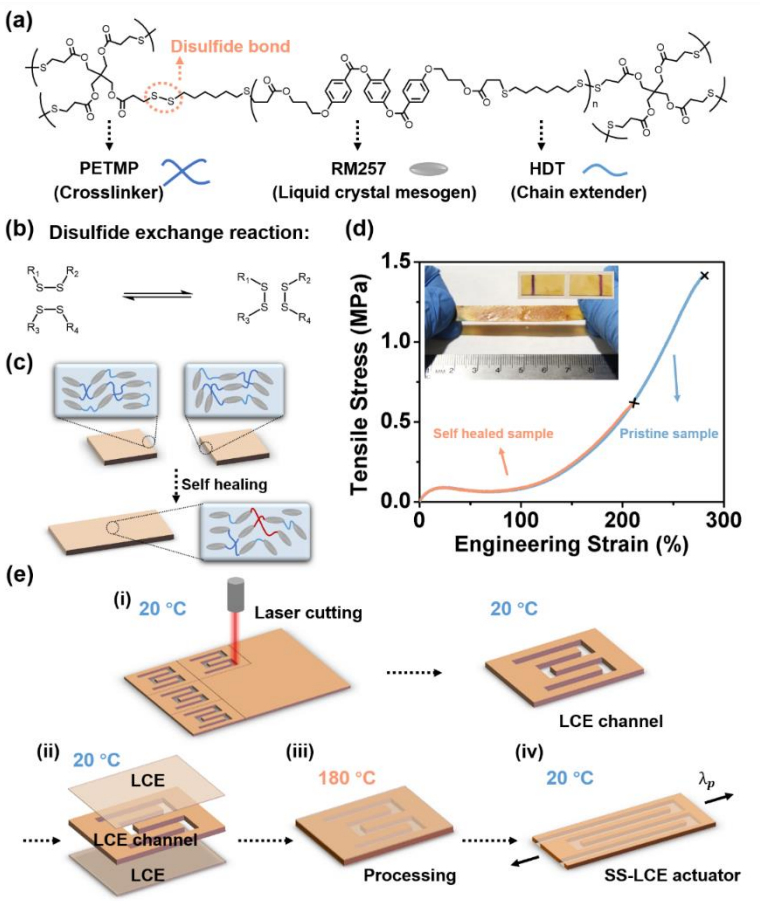

Figure 4.1: Design and fabrication of a fluid-driven ss-LCE actuator. a. Chemical structure of ss-LCE. RM257 is liquid crystal mesogen, HDT is chain extender, and PETMP acts as crosslinker. The disulfide bonds (dynamic bonds) are incorporated into the LCE through oxidation reaction between the thiol groups of the oligomer made through RM257 and HDT and crosslinker PETMP. **b**. Schematic of disulfide bond exchange reaction. **c**. Self-healing process of ss-LCE. These two ss-LCE films are brought into contact and then heated up to 180 °C for 1 hour to trigger the exchange reaction of disulfide bonds. The self-healed sample is obtained after the temperature is gradually decreased to 20 °C. **d**. Uniaxial tension tests of a pristine ss-LCE sample and the self-healed sample. The self-healed sample (orange line) shows similar mechanical property with the pristine sample (blue line), indicating excellent self-healing property of the material. **e**. Fabrication of fluid-driven ss-LCE actuators. (i) First, we use laser cutter to create fluidic channel in one ss-LCE sheet with the thickness of 1 mm. (ii) Then, the LCE sheet with channel is sandwiched between two solid layers of ss-LCE thin film layer (0.3 mm thickness). (iii) This sandwiched structure is heated up to 180 °C in an oven and with an applied compressive force of 1 N for 1 hour, during which the dynamic exchange reaction proceeds and three layers of ss-LCE can be firmly bonded together to form one integrated structure. (iv) After the structure is cooled down to 20 °C, we stretch it by two times and maintain it in the stretched state for 24 hours to align the mesogens in the LCE. A fluid-driven ss-LCE actuator is finally obtained.

Detailed thermo-mechanical characterizations of a monodomain ss-LCE are shown in Figure 4.2. Figure 4.2a shows the stress-strain relationship of a monodomain ss-LCE at different temperatures. As the temperature increases, both the strength and stretchability of ss-LCE decrease. We have also measured the actuation strain of a free standing monodomain ss-LCE film as shown in Figure 4.2b. The LCE film can contract by 48% when the temperature is gradually increased from 22 °C to 120 °C. In addition, we have also performed a cyclic actuation test of a free standing monodomain ss-LCE and no degradation of the actuation strain is observed within 100 cycles (Figure 4.2c).

We fabricate a fluid-driven ss-LCE actuator through laminate manufacturing approach by following four simple steps (Figure 4.1e): (i) We use laser cutter (Universal Laser Systems) to create a connected fluidic channel pattern in an LCE film (1 mm thickness) which is used as a middle layer of the entire structure (the shape and dimension of the fluidic channel can be found in Figure 4.3); (ii) We attach two thin layers of LCE films (0.3 mm thickness) to the two surfaces of the middle layer; (iii) We apply a small compressive loading (1 N) onto the sandwiched structure and place it into an oven with a temperature of 180 °C for an hour. The disulfide exchange reaction is activated and strong binding forms at the interface between LCE layers; (iv) After the structure is cooled down to room temperature, we apply a uniaxial stretch ($\lambda_p = 2$) to the structure to align mesogens, and the stretch is held for 24 hours to fix the mesogen alignment. The fluid-driven ss-LCE actuator with the dimension 50 mm ×12 mm×1.2 mm can be finally obtained.

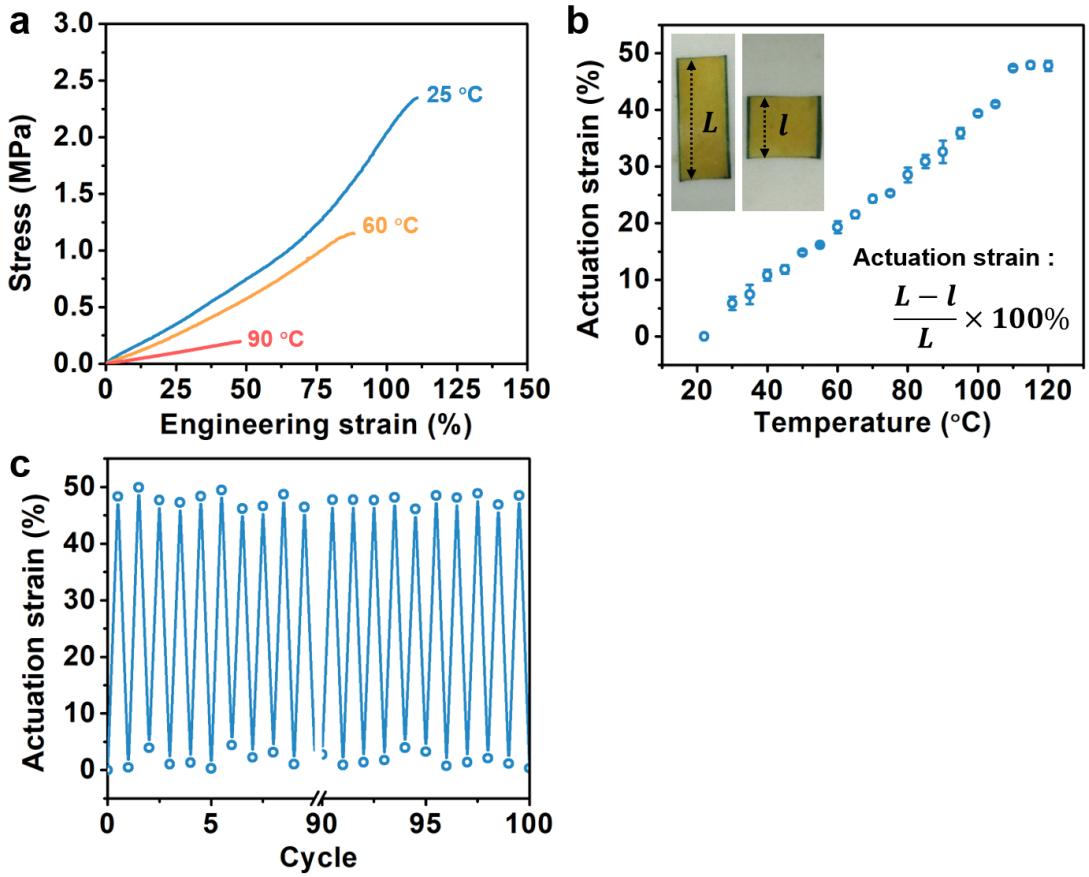

Figure 4.2: Characterizations of a monodomain ss-LCE thin film. a. Stress-strain relationship of a monodomain ss-LCE film at three different temperatures. **b**. Actuation strain of a free standing monodomain ss-LCE film as a function of temperature. The actuation strain increases when the temperature is gradually increased. **c**. The monodomain LCE thin film undergoes cyclic heating and cooling tests between 22 °C and 120 °C for 100 cycles. No degradation of actuation strain of is observed.

4.2.2 Characterization of the fluid-driven ss-LCE actuators

To characterize the actuation performance of the fluid-driven ss-LCE actuator, we measure the actuation strain of the actuator in isotonic configuration (the actuator is subjected to a constant load of 0.4 N which is 100 times of its own weight) as shown in Figure 4.4a. The actuation strain (ε) is determined by $\varepsilon = \frac{L-l}{L} \times 100\%$, where L is the length of actuator in the initial state and

l is the length of actuator in the actuated state. The basic operation principle is illustrated in Figure 4.4a and 4.4b. As hot water passes through the internal fluidic channel of the actuator, it heats up the adjacent LCE; as a result, the actuator generates axial contraction and lifts the weight due to the nematic-isotropic phase transition of the LCE. When room-temperature water (20 °C) is continuously injected into the fluidic channel, the temperature of LCE drops quickly, resulting in fast recovery of the actuator (Figure 4.4a and b).

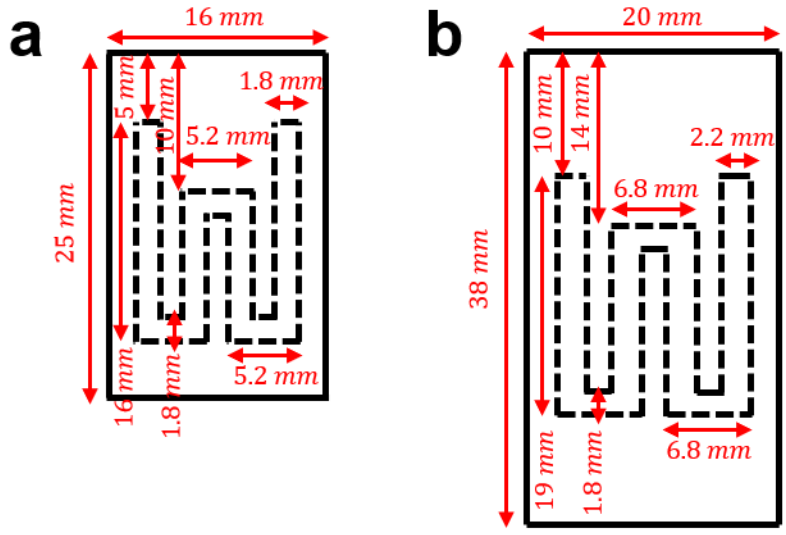

Figure 4.3: Cutting path of the middle layer of the LCE film for constructing the laminated LCE actuator.

To quantitively study the relationship between the actuation strain and the temperature of the injecting water, we inject water with the temperature ranged from 50 °C to 90 °C as shown in Figure 4.4c. For a certain water temperature (for instance 90 °C), the actuation strain increases at

beginning and then reaches a constant value (steady state) within approximately 3 seconds. The actuator can also recover to its initial state within 3 seconds with room-temperature water (20 °C) being injected to the internal fluidic channel. In addition, as we increase the temperature of hot water from 50 °C to 90 °C, larger actuation strain at the steady state as well as higher strain rate are achieved. Specifically, actuation strain (steady state) of 32% and average actuation strain rate of 10 %/s can be realized when the temperature of the hot water is 90 °C.

We further measure the actuation strain of the actuator with two other levels of axial loading (0 N and 1 N) during the isotonic tests (Figure 4.5a and b). We find that both actuation strain at steady state and average actuation strain rate decreases as the load increases. Specifically, the actuation strain in steady state can reach 41%, 31% and 27% and the average strain rates are 11%/s, 10%/s and 4%/s, when the load is 0 N, 0.4 N and 1 N, respectively. However, the recovery rates of the actuator for all the three loads are comparable (9%/s). Based on the measurements, we can quantitively estimate the work density of the actuator (Figure 4.5c), which increases as we gradually increase the axial load.

By alternatively injecting hot and cold water into the fluidic channel of the actuator (with an axial load of 0.4 N), rapid cyclic actuation can be achieved (Figure 4.4d). In the experiments, we control the feeding time of both hot and cold water. The temperature of hot water and cold water is set to be 90 °C and 20 °C, respectively. By tuning the feeding time of water, the LCE actuator can generate actuation strain of 30%, 20% and 10% with a frequency of 0.25 Hz, 0.5 Hz and 1 Hz, respectively (Figure 4.4d). We finally conduct the durability tests of the actuator (Figure 4.5d). Its

actuation performance maintains almost unchanged after 100 cycles, and no delamination and fluid leakage are detected during the cyclic tests.

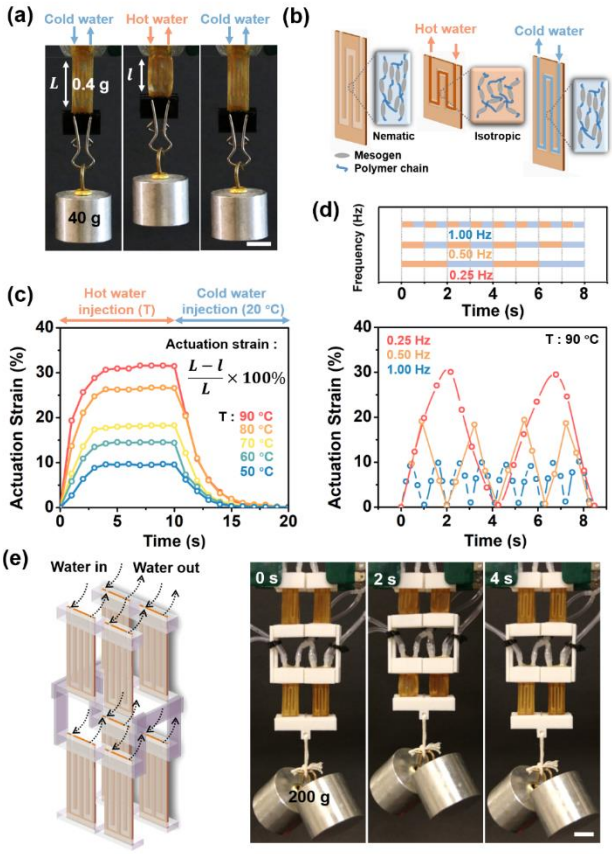

Figure 4.4: Operation principle, characterizations, and enhanced performance of fluid-driven ss-LCE actuators. **a** Photos and **b** schematic illustration of the reversible actuation mechanism of a fluid-driven ss-LCE actuator. The actuator undergoes nematic-isotropic phase transition as hot water is injected into its internal fluidic channel, accompanied with large contraction. The actuator recovers to its initial shape when cool water is pumped into the fluidic channel, owing to the transition from isotropic phase to nematic phase. **c**. Actuation strain of a fluid-driven ss-LCE actuator when hot or cold water is injected into its internal fluidic channels. In the experiment, we inject hot water (at several different temperatures ranging from 50 °C to 90 °C) into its internal fluidic channel for 10 seconds, and subsequently, we inject cold water (20 °C) into the channel for another 10 seconds. The contractive actuation strain of the actuator increases at the beginning and then reaches to a plateau (steady state) within 3 seconds. The actuation strain decreases to 0 within 3 seconds after the cold water is pumped into the actuator. **d**. Cyclic actuation tests of a fluid-driven ss-LCE actuator. The frequency is determined by controlling time period of injecting hot (90 °C)/cold water (20 °C) time. The actuation strain of ss-LCE actuator depends on the actuation frequency. When the frequency of switching hot and cold water is 0.25 Hz, the actuation strain is around 30%; when the frequency is 0.5 Hz, the actuation is around 20%; when the frequency is 1 Hz, the actuation strain is 10%. **e**. The assembly of 8 fluid-driven ss-LCE actuators. This design can increase both of actuation force and displacement without affecting the response speed. Scale bar in **a** and **e**: 1 cm.

Compared to other thermally driven LCE actuator in the previous studies, the fluid-driven ss-LCE actuator constructed in the current study shows significantly faster cyclic response because of the following reasons: 1) active heating and cooling mechanism; 2) small thickness of the LCE films. For most thermally driven LCE based soft actuator of similar size in previous studies, the frequency is typically below 0.1 Hz because of the low thermal conductivity and passive cooling mechanism. However, owing to the merit of actively heating and cooling mechanism, the actuation frequency of the fluid-driven ss-LCE actuator is increased by at least one order of magnitude. Furthermore, it is worth mentioning that the actuation performance of fluid-driven ss-LCE actuator such as actuation strain (~30%), work density (~40 kJ/m^3), strain rate (~10%/s) and frequency (~1 Hz) are all very close to those of mammalian muscle [93].

It is also worth pointing out that the geometry of the fluidic channel could certainly impact the overall performance of the fluid-driven ss-LCE actuator. For the fluidic channel in the current design, we make the distance between two adjacent parallel channels comparable to the thickness of the actuator, with the characteristic time scale for the thermal diffusion along the lateral direction similar to the thickness direction; We determine the size of the fluidic channel (length and width) by letting the time needed for injecting fluid into the entire fluidic channel comparable to the actuation time of the ss-LCE actuator. Therefore, although we have not systematically optimized the design of the fluidic channel, we believe the performance of the actuator in the demonstration is close to its best one that can be achieved.

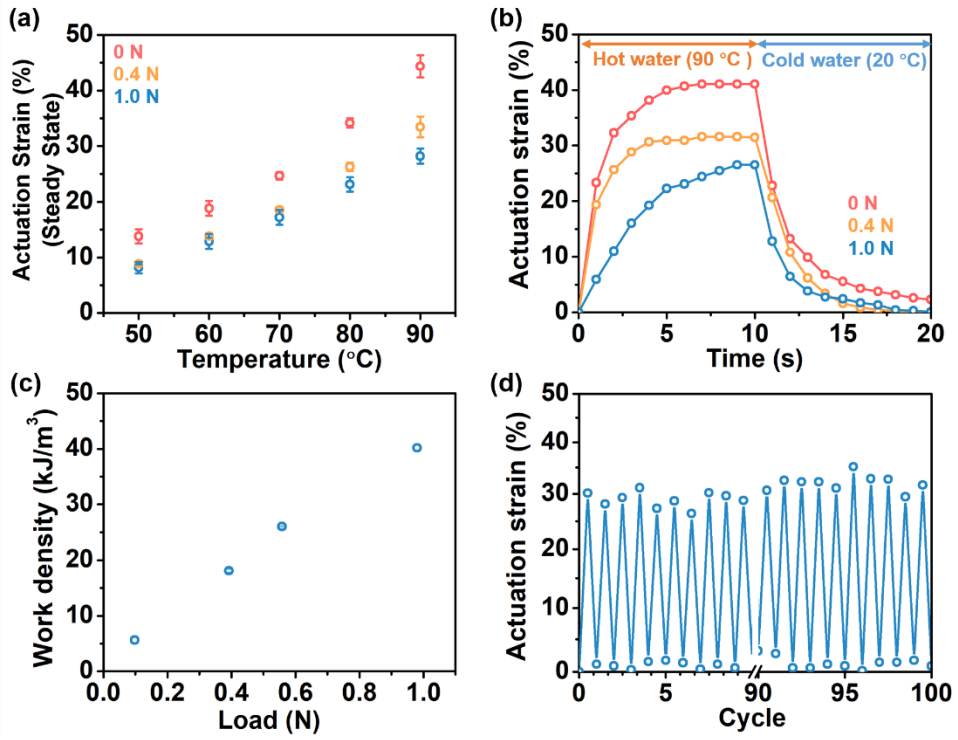

Figure 4.5: Additional characterizations of a fluid-driven ss-LCE actuator. A. Actuation strain (steady state) versus water temperature under three levels of load (0 N, 0.4 N and 1.0 N). The actuation strain at steady state increases with increasing water temperature for a fixed load. As the load is increased, the actuation strain at steady state decreases. **B**. Actuation strain changing with time under three levels of load (0 N, 0.4 N and 1.0 N). When the load is increased, the time for the actuator to reach a steady state increases while their recovery speed is almost unaffected. **C.** Work density of the fluid-driven ss-LCE actuator versus load. The work density can be estimated by $\frac{PH}{V}$ where P is applied load, H is displacement of a load during actuation, V is the volume of actuator. The work density of actuator is comparable to mammalian muscle. **D.** Cycling test of a fluid-driven ss-LCE actuator. The actuator undergoes 100 cycles (10 seconds heating and 10 seconds cooling) subject to an applied load of 0.4 N. No delamination and fluid leakage in the experiments are detected.

When the actuation force and displacement of a single actuator are not sufficient for certain applications, we can amplify them by simply assembling multiple individual actuators as shown in Figure 4.4e. For instance, a single actuator generates modest displacement (~ 1 cm) and load

capacity (0.4 N) during actuation. Without changing the response speed, the assembly of eight such actuators can produce larger displacement (~ 2 cm) with heavier load (2 N) with 90 °C water being injected into all the fluidic channels simultaneously (Figure 4.4e).

4.2.3 Self-repairability of the fluid-driven ss-LCE actuator

Although soft actuators possess many advantages, they may be vulnerable when in contact with sharp edges or corners. For the fluidic driven ss-LCE actuator, a small crack in the actuator may lead to the fluid leakage and permanent failure of the device. Therefore, easy repairing is important for their practical applications. Thanks to the disulfide bonds in the elastomer, the actuator can be self-repairable through bond exchange reaction.

To evaluate the self-repairability of fluid-driven ss-LCE actuator, a small cut is created intentionally on the surface of the actuator using a blade (Figure 4.6a). As a result, when hot water is injected into the actuator, water leaks out as shown in Figure 4.6b. Self-repairing of the actuator can be activated by means of increasing the environmental temperature to 180 °C with 1 N compressive load for 1 hour. In this stage, the polymer network tends to rearrange through bond breakage and reforming so that the crack can be entirely healed. However, the alignment of liquid crystal mesogens is also erased with the rearrangement of the polymer network, and thus the actuation capability of the actuator is lost. To regenerate the actuation capability in the actuator, immediately after the actuator is cooled down to room temperature from 180 °C, we uniaxially stretch it by two times at room temperature and hold the stretch for 24 hours (Figure 4.6a). After

the damaged actuator is fully repaired, we inject hot water again into the sample and cannot detect any fluid leakage (Figure 4.6b). The crack morphology during different stages of the repairing process is shown in Figure 4.6c.

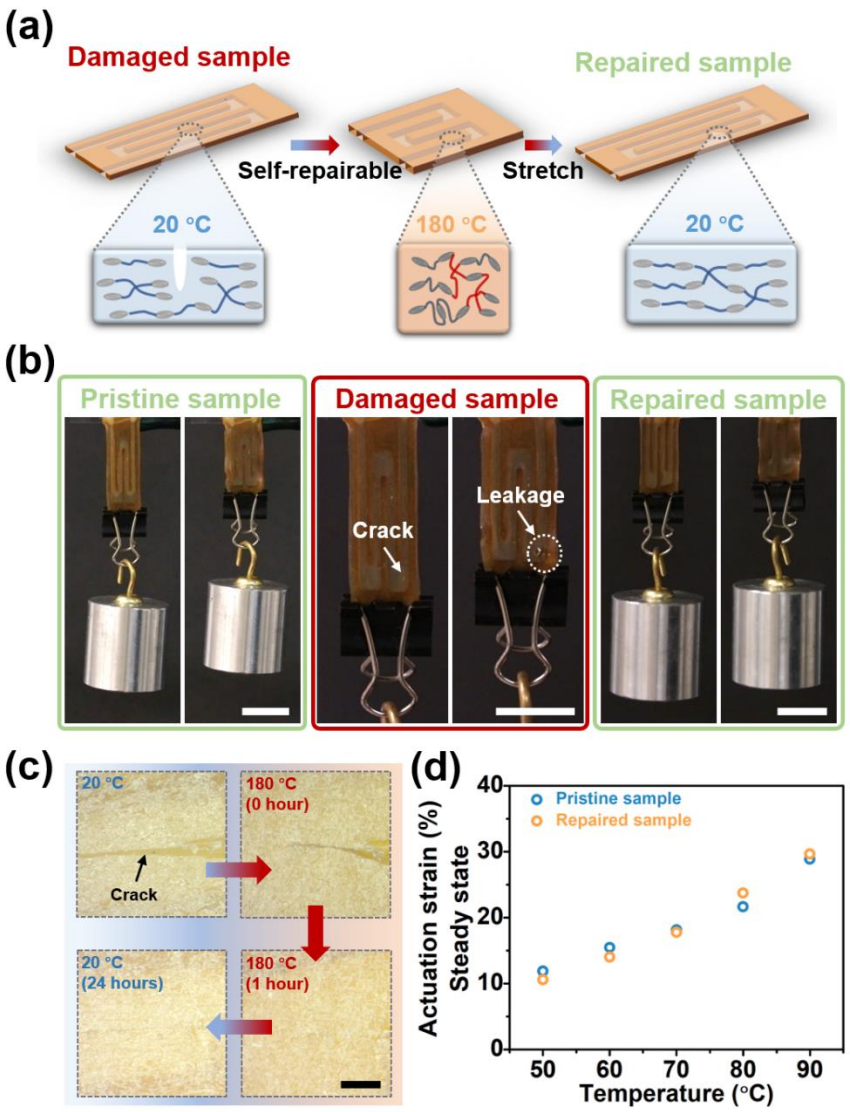

Figure 4.6: Self-repairability of a fluid-driven ss-LCE actuator. **a**. Schematic of the self-repairing process of the actuator. A damaged actuator can be self-repaired through the following two simple steps: we first put the damaged sample in an oven of 180 °C with an additional compressive force around 1 N for an hour; second, after the sample is cooled down to room temperature, we stretch the sample and maintain it in the stretched state for 24 hours. **b**. Experimental demonstration of the self-repairability of a fluid-driven ss-LCE actuator. Water leakage can be clearly detected in the damaged actuator. After self-repairing, the actuator behaves similarly as a pristine one. **c**. The repairing process of an open crack in the LCE film in different stages. **d**. Actuation strain (at the steady state) versus the temperature of the injected hot water for both pristine and self-repaired fluid-driven ss-LCE actuators. It shows that the actuation performance of the pristine actuator and the self-repaired one are almost identical to each other. Scale bar in **c**: 1 cm. Scale bar in **c**: 200 μm.

To examine the recovery of the actuation performance of the fluid-driven ss-LCE actuator, we measure the actuation strain (at steady state) of the repaired sample as a function of the temperature of the injecting water. The results shown in Figure 4.6d demonstrate the negligible difference of the actuation strain between the pristine sample and the self-repaired one.

4.2.4 Recyclability of the fluid-driven ss-LCE actuator

From both economic and environmental aspects, high recyclability of materials in various applications is greatly desired, given that polymer waste has already generated significant adverse impacts on environment. As a matter of fact, recyclable soft actuators have attracted increasingly attention in recent years [82, 109].

There are two critical factors determining the feasibility of recycling a structure in practice [110]: 1) whether a structure is composed of recyclable materials or not; 2) the difficulties of separating different materials in a structure. For most previously developed LCE-based actuators, LCE is often covalently crosslinked and not recyclable like most thermoset polymer. Recent progresses in integrating dynamic covalent bonds into LCE have made the materials themselves recyclable. For the fluid-driven ss-LCE actuator built in this article, it is only composed of a single and recyclable polymer, which makes the recycling process extremely facile as shown below.

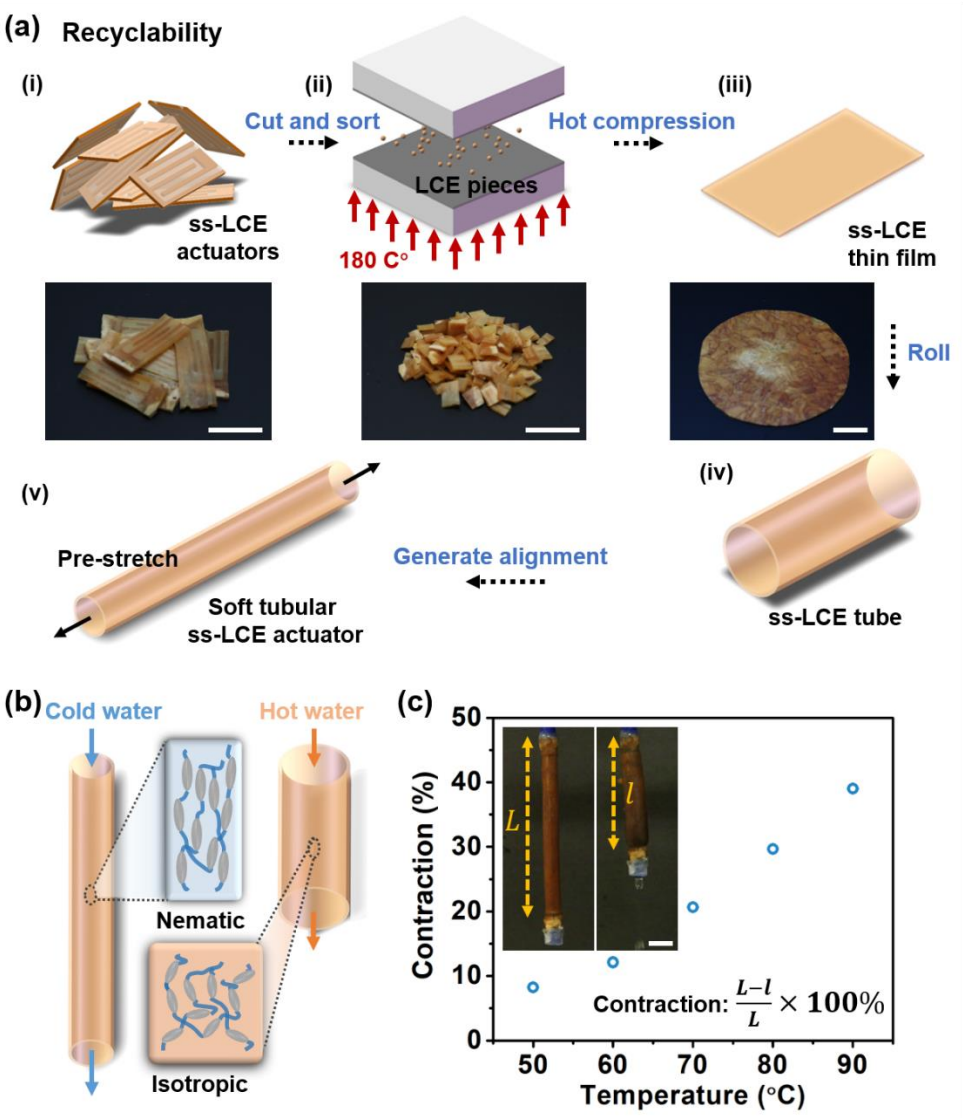

Figure 4.7: Recyclability of fluid-driven ss-LCE actuators. **a**. Recycling process of fluid-driven ss-LCE actuator. First, we cut several used ss-LCE actuators into small pieces. Then, we heat and compress these small LCE pieces at 180 °C for 1 hour, during which bond exchange reaction is activated and a single ss-LCE thin film can be obtained. After that, the LCE thin film is rolled to a tube. Finally, we apply stretch (λp = 2) onto the tube for 24 hours to align and fix the liquid crystal mesogens. A soft tubular ss-LCE actuator can be finally obtained. **b**. Actuation mechanism of the soft tubular actuator. As hot water passes through the soft tubular actuator, it is heated up and contracts in the axial direction. **c**. Contraction strain versus the temperature of hot water for the tubular actuator. The magnitude of contraction depends on the temperature of the hot water. The contraction of the tubular actuator is increased from 9% to 40% as the temperature of the hot water is increased from 50 °C to 90 °C. Scale bar in **a** and **c**: 2 cm.

We demonstrate the entire recycling process of the ss-LCE actuator in Figure 4.7a and 4.8. We first cut several actuators into small pieces (Figure 4.8). We then heat and compress these fragmented pieces (180 °C for 1 hour) into a single LCE thin film enabled by the disulfide bond exchange reaction. The obtained LCE film can be reused to construct a new actuator of different forms. As a proof-of-concept demonstration, we have fabricated a tubular actuator from the thin film. We first roll the thin film into a hollow tube and then apply axial stretch to align the liquid crystal mesogens. We hold the stretch for 24 hours at room temperature to finally obtain an LCE tubular actuator as shown in Figure 4.7a. When we inject hot water into the hollow tube, it contracts as shown in Figure 4.7b. The magnitude of the contraction can be controlled by varying the temperature of the injecting water. Specifically, the contractive strain of the actuator is increased from 9% to 40% when the injecting water temperature is increased from 50 °C to 90 °C (Figure 4.7c).

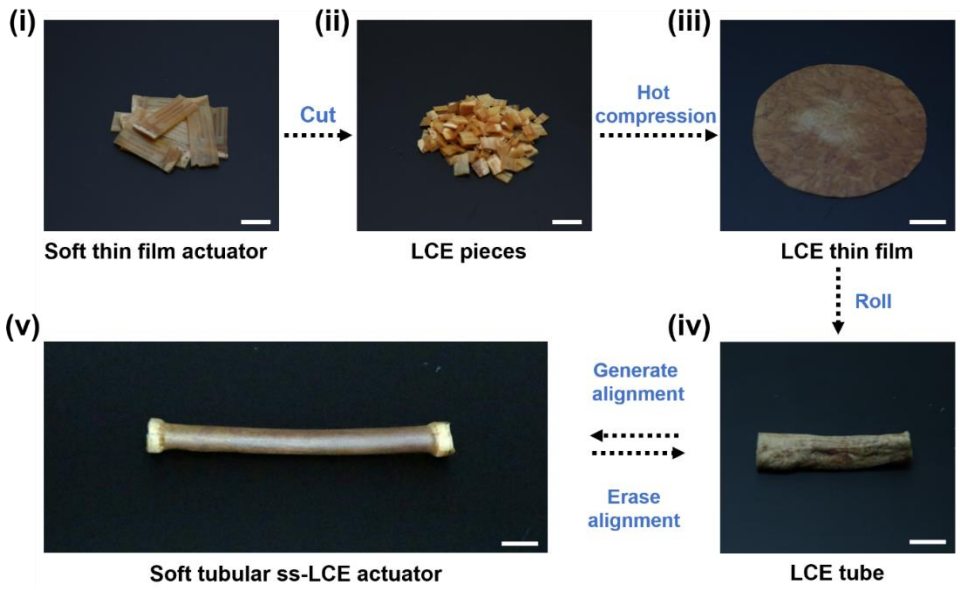

Figure 4.8: Recyclability of fluid-driven ss-LCE actuator. Several used fluid-driven ss-LCE actuators are cut into small pieces. These fragmented pieces are heated and compressed (180 °C for 1 hour), forming ss-LCE thin film enabled by the disulfide bond exchange reaction. The obtained ss-LCE thin film can be used to construct new actuators of different forms. For instance, we fabricate a soft tubular actuator from the thin film. We first roll the thin film into a hollow tube and then apply axial stretch to align the liquid crystal mesogens. We hold the stretch for 24 hours at room temperature to finally obtain an LCE tubular actuator. Scale bar: 1 cm.

4.2.5 A bimorph fluid-driven ss-LCE actuator and its application

Next, we demonstrate the design of a bimorph actuator based on the fluid-driven ss-LCE structure with five layers laminated together: three layers of solid ss-LCE thin film and two layers ss-LCE film with laser-cut channels in the middle (Figure 4.9a). Detailed characterizations of the bimorph actuator can be found in Figure 4.10. The bimorph actuator can bend in two directions by injecting hot or cold water into one of its two channels.

In addition, for all thermally responsive materials, an appropriate range of their working temperature is often limited by their response temperature. For example, in most thermally driven

LCE actuator, the environmental temperature is often set below the nematic-to-isotropic phase transition temperature. However, because of the introduction of the internal cooling mechanism, the bimorph actuator can exhibit similar bending actuation even at high environmental temperature (80 °C), through injecting cold water (5 °C) into its fluidic channels (Figure 4.9b).

We further construct a soft gripper by assembling three bimorph LCE actuators in parallel, which can carry out multiple tasks at both high temperature and low temperature. As demonstrated in Figure 4.9c, 4.9d, in the air with the temperature of 20 °C, three bimorph LCE actuators simultaneously bend inward or outward as hot water is injected into different channels of the actuator. As a result, the soft gripper can grasp a plastic cap or lift a rigid plate (with a hole). When the soft gripper is placed in a water bath with temperature of 80 °C, the three bimorph LCE actuators first contract nearly homogenously. When cold water with a temperature of 5 °C is injected to some of the fluidic channels of the actuator, all three actuators can bend inward and grasp a coin in the water as shown in Figure 4.9e.

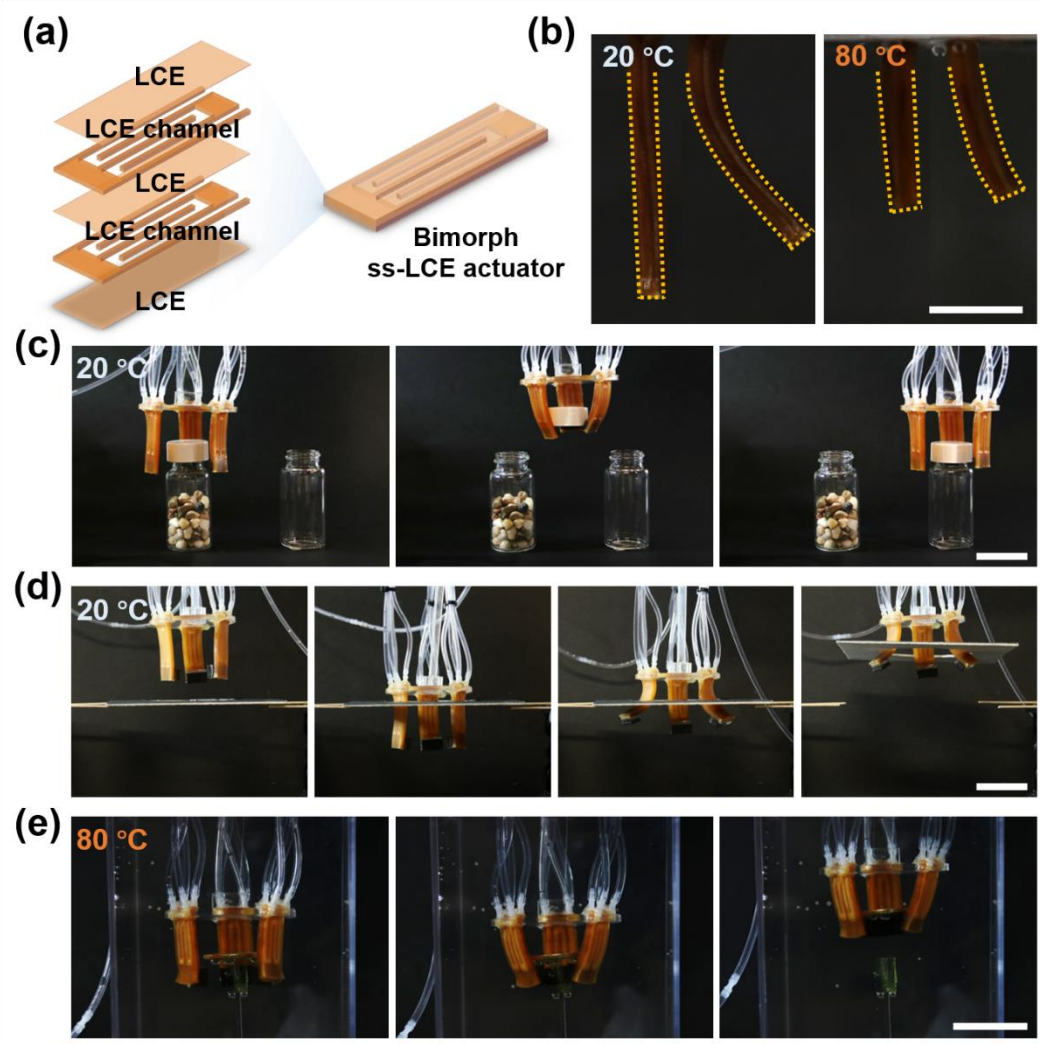

Figure 4.9: Bimorph fluid-driven ss-LCE actuators and soft gripper application. **a**. Structure of a bimorph fluid-driven ss-LCE actuator. The actuator is composed of five layers: three layers of solid LCE thin film and two layers of LCE film with laser-cut channels in the middle. **b**. The bimorph ss-LCE actuator can generate two directional bending at both 20 °C and 80 °C. **c**. At an environmental temperature of 20 °C, the soft gripper composed of three actuators can grasp a bottle cap when all the three actuators bend inward simultaneously. **d**. The soft gripper can lift a cardboard (with a hole) when the three actuators bend outward. **e**. In a water bath at the temperature of 80 °C, three bimorph ss-LCE actuators contract homogeneously first. When cold water with a temperature of 5 °C is injected into the fluidic channel, three bimorph ss-LCE actuator can bend inward and grasp a coin inside the water bath. Scale bar in (**b**-**e**): 2 cm.

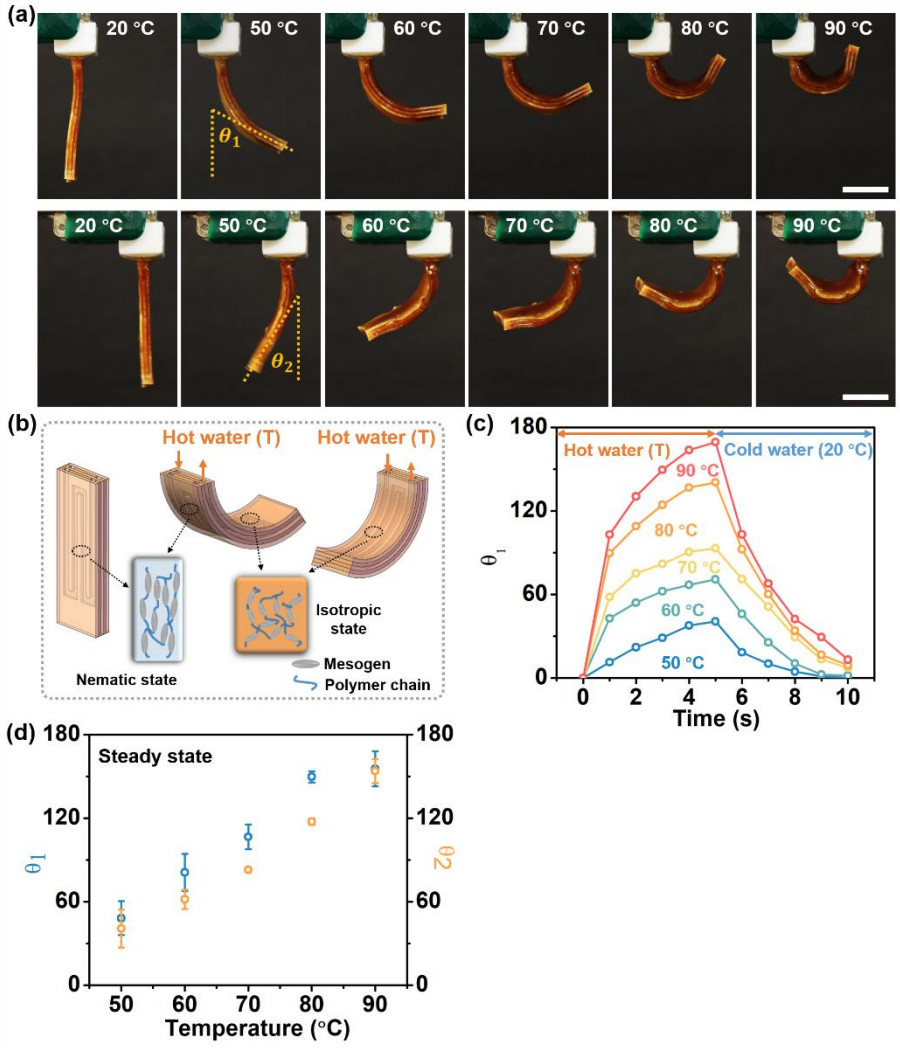

Figure 4.10: Detailed characterizations of a bimorph fluid-driven ss-LCE actuator. a. A bimorph actuator can generate two-directional bending actuation when hot water is injected into one of the two fluidic channels. The bending angle can be controlled by the temperature of the injecting water. **b**. Actuation mechanism of the bimorph actuator. **c**. Change of the bending angle θ_1 versus time with different temperatures of injecting water. Both heating time and cooling time are set to be 5 seconds. **d**. Bending angle θ_1 and θ_2 can be tuned by changing the temperature of the injecting water. Scale bar in **a**: 1 cm.

4.2.6 Soft locomoting robot

Finally, we build a soft locomoting robot by assembling four bending actuators (Figure 4.11a). The bending actuator is made by attaching a strain-limiting layer (Kapton film) to one side of the ss-LCE actuator. Upon injecting hot water, bending actuation can be produced by the actuator, owing to the mismatch of the heat-induced deformation between LCE and the strain-limiting layer (Figure 4.11b). The actuator can fully recover once the cold water passes through the fluidic channel. More detailed characterizations of the bending actuator can be found in Figure 4.12.

To realize automatic control of the robot, we set up a fluidic control system as shown in Figure 4.11a. Hot and cold water from two water reservoirs is pumped through solenoid valves to the fluidic channels in the actuator. To control the flow rate of water in the internal channel of each actuator, eight solenoid valves are employed, which are further controlled by microcontroller through pulse width modulation. Therefore, the locomotion of the soft robot can be achieved automatically.

The soft locomoting robot has two main actuating segments: two front legs and two rear legs. To make the soft robot move forward, inspired by the locomotion of inchworm, we intend to generate “wavy” configuration in the robot, which can be achieved by sequentially actuating the four legs. The schematic of the Figure 4.11c illustrates one cycle of the robot moving forward in which four steps are involved: 1) from 0 second to 10 second, two rear legs are injected with hot water and two front legs are injected with cold water, which makes the two rear legs bend upward while two front legs stay stationary; 2) from 10 second to 20 second, we inject hot water into all

the four legs, causing the bending of all the four legs and lifting up of the body of the soft robot; 3) from 20 second to 30 second, two rear legs recover to their initial flat shape with the injection of cold water while two front legs maintain its deformed state. In this step, two rear legs act as stationary points which push whole body of robot moving forward. 4) in the last step from 30 second to 40 second, we inject cold water into two front legs to make them recover into flatten state, a net displacement (around 5~6 mm) of the robot can be generated. Continuous movement of the soft robot can be achieved by repeating the above four steps. The soft walking robot can move around 48 mm for 8 cycles (320 s) which is shown in Figure 4.11d and e. The average moving speed of the robot (0.15 mm/s) is 5 times faster than the electrically controlled LCE-based soft robot reported in previous study.

It is noted that the crawling speed of the soft robot is not as rapid as the single LCE actuator demonstrated in Figure 4.4. The two main reasons for the slow speed are: First, the soft robot is automatically controlled through a fluid control system. There is significant heat loss when the hot fluid travels from the tank to the actuator. Consequently, the temperature of the fluid injected into the actuator is lower than the temperature of the fluid in the tank, which makes the actuator respond slower. Second, to support the entire body of the soft robot, we also increase the thickness of the LCE actuators (from 0.3 mm to 1 mm) as compared to the LCE actuator in Figure 4.4. It takes longer time for the thermal diffusion in a thicker LCE film, which also increases the actuation time of the LCE actuator.

Nevertheless, the two reasons mentioned above are not intrinsic barriers for a structure with the fluid-driven ss-LCE actuators to achieve fast speed. For example, to increase the temperature of the fluid injected into the actuator, we can either optimize the fluidic control system to reduce the heat loss or increase the temperature of the fluid in the tank. Moreover, we may still use the LCE actuator with small film thickness. To obtain large actuating force, we can employ multiple LCE actuators in parallel as shown in Figure 4.4e.

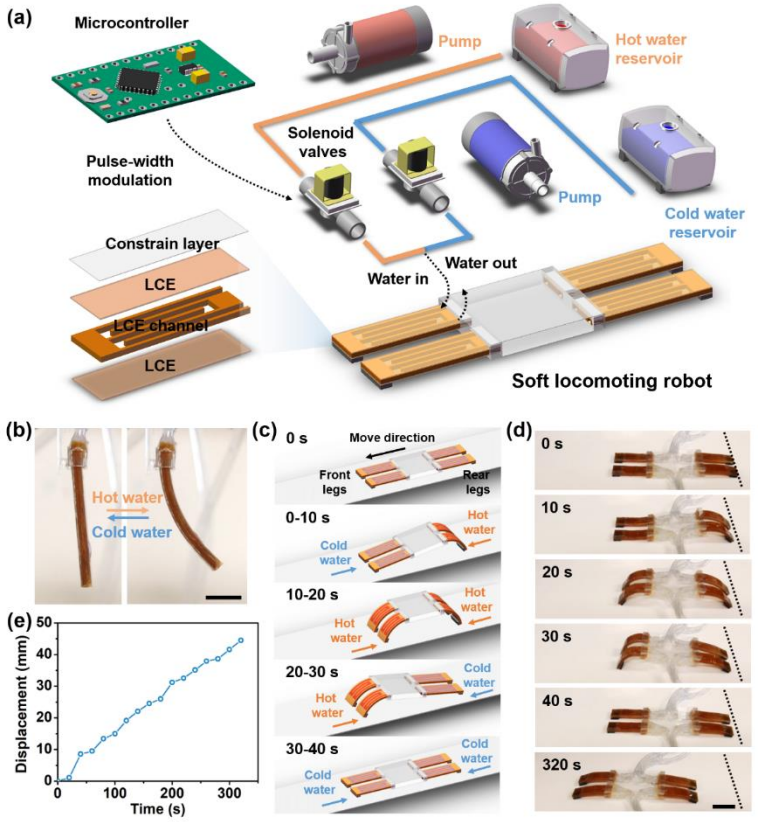

Figure 4.11: Soft locomoting robot with automatic and programmable control. **a**. Robotic design and the control system. The soft locomoting robot is composed of four fluid-driven ss-LCE bending actuators. For each bending actuator, a strain-limiting layer (Kapton film) is attached to one surface of the three-layer fluid-driven ss-LCE actuator. For fluidic control system, hot water or cold water is pumped from their reservoirs and injected into each bending actuator through solenoid valves. Each solenoid valve can be controlled by the microcontroller via pulse-width modulation. **b**. Reversible bending actuation of the actuator can be realized through alternatively injecting hot and cool water. **c** and **d**, Schematics and snap shots of soft locomoting robot during movement. The motion of the robot contains four steps: 1) from 0 second to 10 second, two rear legs are injected with hot water and two front legs are injected with cold water, which makes the two rear legs bend upward while two front legs stay stationary; 2) from 10 second to 20 second, we inject hot water into all the four legs, causing the bending of all the four legs and lifting up of the body of the robot; 3) from 20 second to 30 second, two rear legs recover to their initial flat shape by injecting cold water while two front legs maintain its deformed state. In this step, two rear legs act as stationary points which push the whole body of robot forward; 4) in the last step from 30 second to 40 second, we inject cold water into two front legs to make them recover into flatten state; a net displacement (5 mm) of the robot can be generated. Continuous movement of the robot can be achieved by repeating the above four steps. **e**. Displacement of the soft robot versus time. The speed of robot is around 3 body length/hour. Scale bar in **b** and **d**: 2 cm.

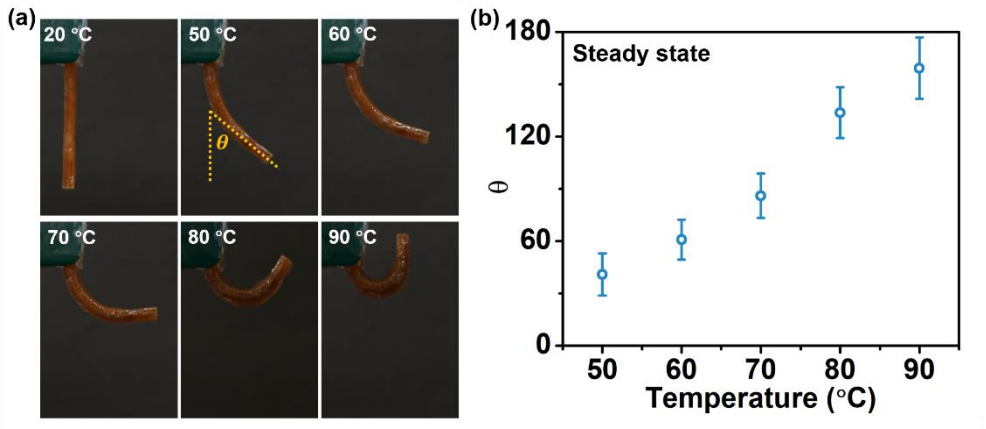

Figure 4.12: Detailed characterizations of a fluid-driven ss-LCE bending actuator. a. Photos of the bending actuator during actuation with the injecting water of several different temperatures. **b**. Bending angle (in steady state) of the actuator versus the temperature of injecting water. Scale bar in **a**: 1 cm.

4.3 Conclusion

In this article, we have designed, fabricated and characterized an eco-friendly fluid driven ss-LCE actuator. We have demonstrated that the combination of the fluidic structure design and the dynamic covalent bond material enables the facile laminate manufacturing approach, self-repairing capability and easy recyclability of the soft actuator. Thanks to the internal fluid heating and cooling mechanism and the strong bonding between different material layers, the actuator created in this article can generate fast cyclic actuation and operate in a broad range of environmental temperature. As proof-of-concept demonstrations, using the ss-LCE actuators, we have further constructed two prototypes of soft robotic structures: a gripper and a locomoting robot.

Compared with most previously developed LCE-based actuators, one of the most important advantages of the fluid-driven ss-LCE soft actuator developed in this article is its fast response.

As shown in Figure S4, the newly developed actuator can easily generate 10% cyclic actuation strain at 1 Hz which is very hard to achieve by previously developed LCE-based actuators of similar size. Moreover, because the actuator is only composed of a single material (ss-LCE), it can be easily recycled and reprocessed, which may be important for the future development of soft robots for various applications.

In the current work, for simplicity, we use water as the circulating fluid to heat up or cool down the actuator, so the highest/lowest temperature of the fluid is limited by the boiling/freezing temperature of the water. We should be able to further increase the response speed of the actuator by using other fluid with higher boiling temperature and/or lower freezing temperature. Moreover, we have only demonstrated simple and limited actuation modes of the fluid-driven ss-LCE actuator in the current study. Nevertheless, thanks to the dynamic covalent bonds in the LCE, we should be able to easily program or even reprogram diverse actuation modes of the fluid-driven ss-LCE actuator [111], which can significantly increase the design space of soft robots using the actuator. We hope our design of the fluid-driven ss-LCE actuator could facilitate more applications of LCE in the field of soft robotics.

Chapter 4, in full, is a reprint of the material as it appears in "Recyclable and self-repairable fluid-driven liquid crystal elastomer actuator", *ACS Applied Materials & Interfaces* 12 (2020): 35464-35474, by Qiguang He, Zhijian Wang, Yang Wang, Zhaoqiang Song and Shengqiang Cai. The dissertation author was the primary investigator and first author of this paper.

Chapter 5 Liquid crystal elastomer based artificial muscle fiber actuator

5.1 Introduction

One dimensional contraction can be broadly found in nature and engineering applications, which has drawn much attention in recent decades. For instance, human muscle made from bundles of muscle fiber can generate over 50% contraction in order to maintain normal physiological activities such as walking and running [53]. Spider silks contracts when the humidity changes, which provides resistance and reduces the damages or impacts coming from the nature [112, 113]. The smart textures can regulate their morphologies through filaments contraction in order to adapt the environment changes [114]. In this context, various stimuli-responsive materials have been developed as actuator to realize one dimensional contraction. For example, the hydrogel fibers shrink when the environmental temperature is above its lower critical solution temperature (LCST) [75], nylon fishlines provides extremely large stress when they are heated [80]. Although drastically efforts have been made in the past, there still exist few challenges in this area such as slow responsive speed, small actuation strain, which limit practical applications.

Liquid crystal elastomer (LCE) is one type of actuating material which is composed of polymer networks and liquid crystal molecules [98]. The LCE based soft actuators can generate extremely large and reversible actuation strain (~ 50%) based on its nematic-isotropic phase transition, which have been broadly developed in artificial muscle and soft robotic field [58, 115].

It has been shown that the LCE based actuators can be activated by various external stimulus such as heat [13], light via photothermal or photochemical effects [116, 117]. By programming the orientation of the liquid crystal mesogens of the LCE, versatile deformation modes can be realized such as contraction, bending and twisting [34, 118, 119].

Previously, in order to fabricate fiber form of LCE, several methods are widely adopted. For instance, Roach et al use 3D printing technique to fabricate long LCE fibers and apply these fibers into smart textiles application[114]; Naciri et al prepare the LCE fiber through drawing from melt mixture and they demonstrate the LCE fiber can be used as artificial muscle [120]. However, these fibers' diameter is still in large size (> 300 μm) and their response speed are slow. It is well known that the response can be greatly enhanced by the reduction of the size. To further reducing the size of fiber, the electrospinning technique has been used in the past, which thin polymer fiber can be extracted from their solution due to the large electrostatic charges. Finkelman et al first synthesis the main chain LCE fiber using electrospinning methods [121]. Sharma et al prepare the LCE-PVP composite fiber which shows the good alignment of liquid crystal mesogens [122]. Although many pioneer works have been done in the past, it is still challenging to collect the individual LCE fiber from the substrate after electrospinning and further apply the LCE fiber to the micro robotic applications.

Here, in this work, we are able to fabricate the LCE fiber with micrometer size via electrospinning technique. The LCE fiber can be easily collected from the metallic mesh collector after electrospinning process (Figure 5.1). We further show that the LCE fiber exhibits large and

reversible actuation (~ 60%) with extremely fast response speed (< 0.2 s), which provides the similar magnitude as human skeleton muscle. Additionally, due to the reduction of size, we find that the LCE fiber can perform unique characteristic such as self-oscillation under gradient temperature field. Moreover, we show the PDA-coated LCE fiber can be precisely and remotely controlled through photothermal effect. Finally, we demonstrate the feasibility of LCE fiber in the micro robotic and machine applications, an electrically controlled micro-tweezer, light-driven untethered micro-swimmer, and soft impendent pump are developed with desirable functionalities.

5.2 Results and discussion

5.2.1 Fabrication, work mechanism, thermal and mechanical property of LCE fiber

In the experiment, we use RM 257 as liquid crystal mesogen, HDT as chain extender (Figure 5.2). We first prepare the ink for the electrospinning which we dissolve the oligomer into the chloroform, detailed preparation can be found in supplementary materials. In terms of the electrospinning process as shown in Figure 5.1A, the ink can be pushed out with constant flow rate (0.02 mL/min) by the syringe pump. The metallic mesh collector is connected to the negative electrode of power supply, which is used to collect the LCE fiber during the electrospinning process. When the high voltage (6 kV) power supply is connected to the needle tip, the LCE fibers form and these fibers are collected in the gap of the metallic mesh (Figure 5.1B), these fibers have smooth surface as shown in Figure 5.1C. During the electrospinning process, we expose the UV irradiation to the LCE fiber in order to crosslink the LCE fibers.

The diameter of as-spun LCE fiber range from 10 μm to 100 μm as shown in Figure 5.1C and Figure 5.3. These as-spun LCE fibers are in polydomain state, which can be confirmed by the uniaxial tension tests (Figure 5.1D). For all different size of the LCE fiber, the stress of maintains a low value at beginning and then gradually increases when the stretch is over 3, which shows the similar behavior as bulk polydomain LCE. In the polydomain LCE, liquid crystal mesogens align well in one domain microscopically while the orientation of the mesogens in one domain is different from another. However, to have actuation behavior, the liquid crystal mesogens of LCE fiber has to be aligned along one direction. Therefore, to realize the actuation of LCE fiber, we apply the external load to the as-spun LCE fiber to align the mesogens forming monodomain LCE fiber (Figure 5.1E). As the monodomain LCE fiber is heated, the fiber undergoes nematic-isotropic phase transition. As the result, the LCE fiber contracts along its longitudinal direction. The actuation is fully reversible, the LCE fiber can fully recover to its initial configuration after the temperature drops to room temperature (Figure 5.1E). To confirm the orientation of the liquid crystal mesogens in different states, we use polarized optical microscope to check the brightness difference because of the optical birefringence (Figure 5.1F). For the polydomain LCE fiber, there is no brightness difference observed at 45° and 90° with respect to the analyzer. However, for the monodomain LCE fiber, we can observe the maximum brightness at 45° and minimum brightness at 90° with respect to the analyzer. In terms of the LCE fiber at isotropic state, we cannot observe the brightness difference at 45° and 90° with respect to the analyzer. We further characterize the glass transition temperature and nematic-isotropic phase transition temperature of as-spun LCE

fiber (polydomain state) using DSC (Figure 5.1G), which can be measured as 1 °C and 95 °C, respectively.

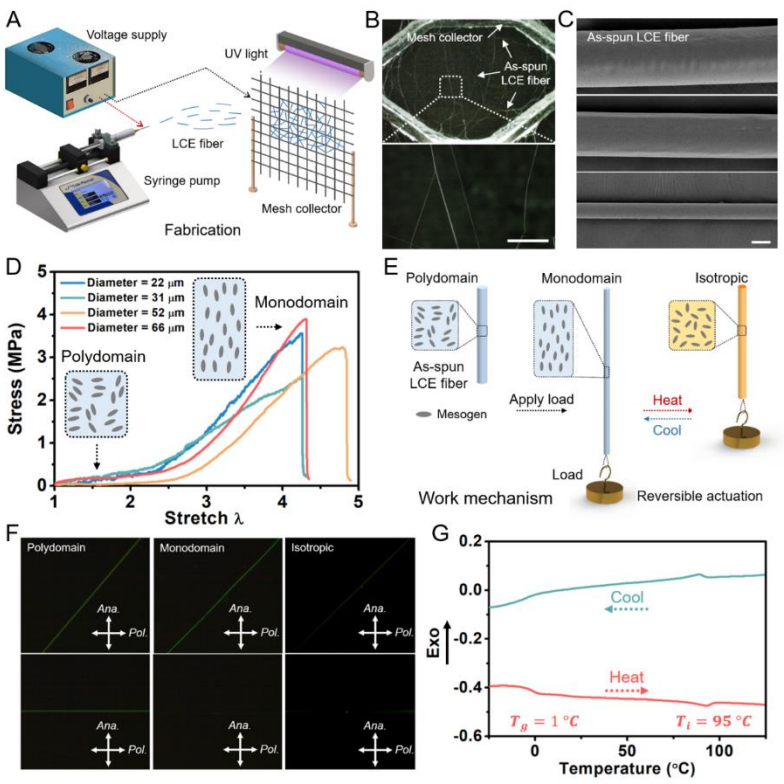

Figure 5.1: Fabrication and work mechanism of LCE fiber. A. Schematic of the electrospinning setup. The positive electrode of power supply is connected to the metallic needle, the negative electrode is connected to the metallic mesh collector. The syringe pump is used to control the flow rate of the ink with constant speed. The LCE fiber is crosslinked under UV irradiation during the electrospinning. The as-spun LCE fiber with polydomain state can be collected from the mesh after electrospinning. **B.** Optical images of as-spun LCE fibers with different diameters (polydomain state). **C.** SEM images of as-spun LCE fibers with different diameters (polydomain state). **D.** Uniaxial tensile tests (under 25 °C) of as-spun LCE fibers with different diameters (22 μm to 66 μm). For as-spun LCE fibers with different diameters, the stress first maintains low magnitude and then gradually increase when the stretch is over 3. The stress plateau corresponds to the rotation of liquid crystal mesogens. **E.** Work mechanism of LCE fiber. The as-spun LCE fiber is in polydomain state. When the load is applied to the fiber, the fiber is stretched from polydomain to monodomain state, liquid crystal mesogens are aligned along longitudinal direction of the fiber after stretching. When the fiber (with applied load) is heated, the fiber contracts along longitudinal direction due to nematic-isotropic transition. The fiber can fully recover to its initial shape when the temperature is cooled down. **F.** Polarized optical microscope (POM) images of polydomain, monodomain and isotropic state of LCE fibers with two different angles with respect to the analyzer. **G.** Differential scanning calorimetry (DSC) trace of as-spun LCE fiber. The glass transition temperature T_g is 1 °C and the nematic-isotropic phase transition temperature T_i is 95 °C. Scale bar in **B**: 200 μm. Scale bar in **C**: 20 μm.

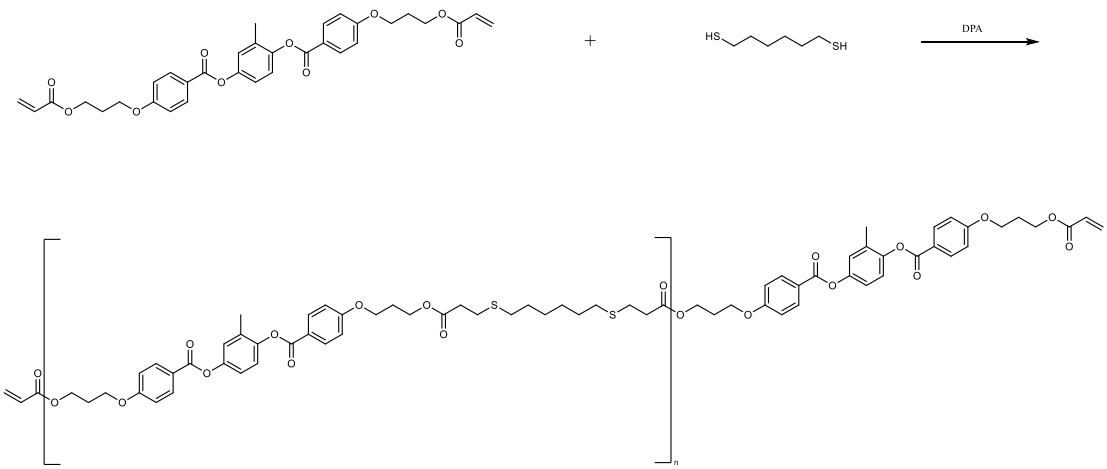

Figure 5.2: Chemical component of LCE fiber.

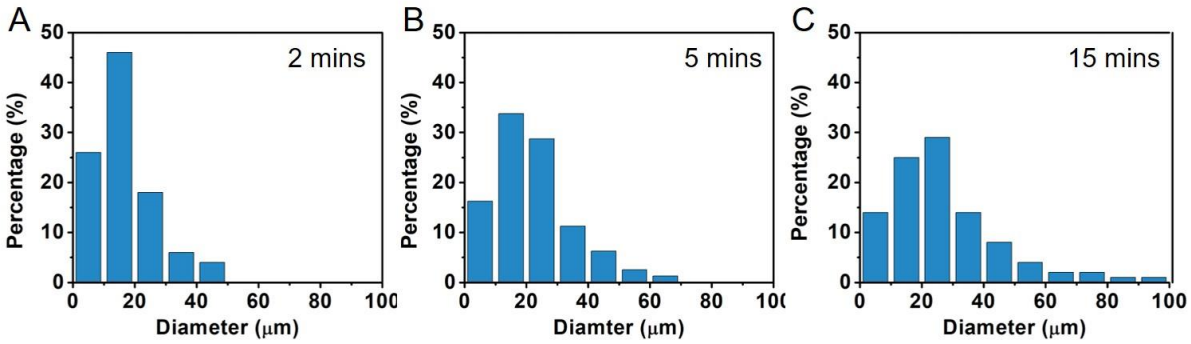

Figure 5.3: Diameter distribution of as-spun LCE fiber with different electrospinning times (2 mins, 5 mins and 15 mins).

5.2.2 Actuation performance characterization of LCE fiber

It is known that the LCE fiber in the monodomain state can generate large actuation when the temperature is above the nematic-isotropic phase transition temperature. In the experiment, we apply the external load to the as-spun LCE fiber in order to align the liquid crystal mesogens. Because of the applied load, the length of LCE fiber increases from L to $l\,(T = 20\,°C)$ and the diameter decreases (Figure 5.4). To generate the contraction, we increase the temperature, the length of LCE fiber shrink from $l\,(T = 20\,°C)$ to $l\,(T)$ as shown in Figure 5.5A. In order to

quantitively characterize the actuation of the LCE fiber, we define the actuation strain as $\varepsilon = \frac{l\,(T=20\,^{\circ}C)-l\,(T)}{l\,(T=20\,^{\circ}C)} \times 100\%$.

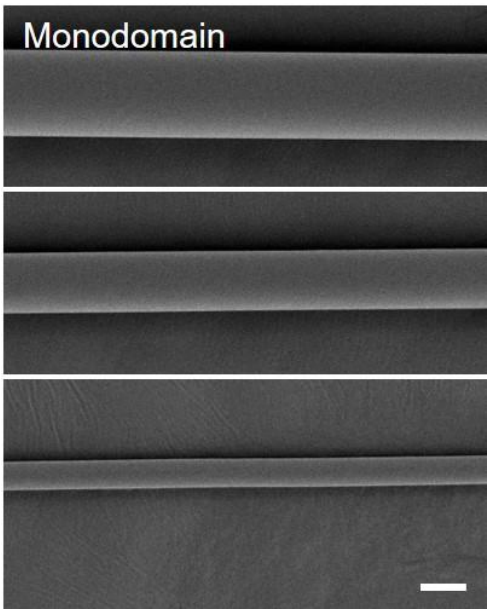

Figure 5.4: SEM images of LCE fiber after applying 0.02 MPa stress (monodomain state). Scale bar: 20 μm.

We first apply three different levels of external load to the LCE fiber and measure the dimensionless length ($l\,(T)/L$) as we gradually increase the temperature (Figure 5.5B and Figure 5.6). For a given applied stress, the dimensionless length decreases monotonically when the temperature is increased. It should be noted that the length of the fiber has a sharp decrease at T = 95 °C that is corresponding to the nematic-isotropic transition, which is consistent with DSC measurement (Figure 5.1G). Quantitively, the dimensionless length ($l\,(T)/L$) of LCE fiber (0.02 MPa applied stress) shrinks from 1.8 to 0.8 as the temperature is gradually increased from 20 °C

to 120 °C. The dimensionless length changes from 1.9 to 1.3, 2.3 to 1.5 at 0.08 MPa and 0.16 MPa applied stress, respectively. In addition, to study the actuation strain of LCE fiber with different diameter ranging from 22 μm to 94 μm, we calculate the actuation strain at T = 120 °C as shown in Figure 5.5C. For a given applied stress, there is no significantly difference in terms of the actuation strain when the fiber diameter changes. This is because the size of current LCE fiber is still in micrometer dimension, where size dependent phenomenon can only be observed when the fiber is in nanometer scale. Moreover, the average actuation strain of LCE fiber is 55%, 30% and 25% at the 0.02 MPa, 0.08 MPa and 0.16 MPa applied stress, respectively, which exhibits large deformability.

To quantitively study the actuation stress of LCE fiber, we apply the pre-stretch to polydomain LCE fiber by λ at 20 °C to align the liquid crystal mesogens. After stretching, the length increases from L to l. By fixing the length l, we measure the actuation stress as we gradually increase the temperature (Figure 5.5D and Figure 5.7). The result of actuation stress measurements is shown in Figure 2E, the actuation stress of LCE fiber ($d = 54\ \mu m$ before stretching) keeps increasing as we raise the environmental temperature due to the nematic-isotropic phase transition. In addition, the LCE fiber with larger pre-stretch ratio λ can generate higher magnitude actuation stress at the same temperature, specifically, 0.28 MPa, 0.22 MPa, 0.11 MPa and 0.02 MPa at λ = 3.0, 2.5, 2.0 and 1.5, respectively. This result can be attribute to the increased alignment of liquid crystal mesogens when the pre-stretch ratio is large. For the actuation stress of different size of LCE fiber, similarly,

the magnitudes are all comparable even the diameters of LCE fiber are quite different (Figure 5.5F).

By reducing the size, LCE fiber exhibits fast actuation response. To estimate the response speed of LCE fiber, in the experiment, we use a cartridge heater (surface temperature 300 °C) to heat up the specimen. When the heater is approaching to the LCE fiber, the fiber contract instantaneously (< 0.2 s). The LCE fiber can suddenly recover to its initial shape when we remove the heat source as shown in Figure 5.5G.

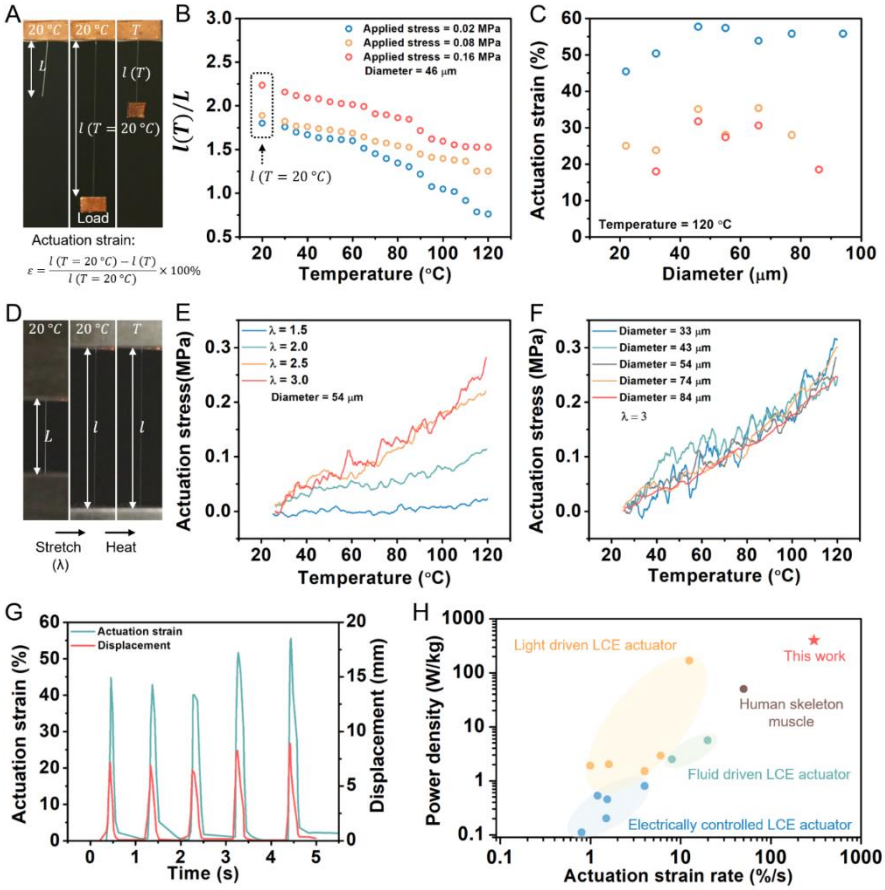

Figure 5.5: Actuation performance characterizations of LCE fiber. A. The length of LCE fiber in polydomain, monodomain and isotropic states. The length of the as-spun LCE fiber (polydomain) is L. When a specific load is applied to the as-spun LCE fiber, the length of LCE fiber (monodomain) increases to $l\,(T = 20\,°C)$. The length of LCE fiber (isotropic) becomes $l\,(T)$ when the temperature is increased to T. **B.** The dimensionless length change of LCE fiber $l\,(T)/L$ as a function of temperature under three different levels of applied stress from 0.02 MPa to 0.16 MPa. For a specific level of applied stress, the $l\,(T)/L$ of LCE fiber decreases when the temperature is gradually increased. **C.** The relationship between actuation strain and fiber diameter with different levels of applied stress. For LCE fibers with different diameters, the actuation strain shows comparable value. **D.** Actuation stress measurement of LCE fiber. The as-spun LCE fiber (polydomain) is firstly stretched by λ at 20 °C. The actuation stress of LCE fiber can be measured as the temperature is gradually increased from 20 °C to T while the strain is fixed. **E.** Actuation stress of LCE fiber as a function of temperature with four pre-stretch ratios (λ) 1.5, 2.0, 2.5 and 3. The actuation stress increases as the temperature increases. Larger pre-stretch ratio (λ) results in higher magnitude of actuation stress at same temperature. **F.** The actuation stress of LCE fibers with different diameters ranging from 33 μm to 84 μm. They all exhibit similar value at same temperature. **G.** Response speed of LCE fiber. **H.** Ashby plot of power density versus actuation strain rate of LCE-based soft actuators and human skeleton muscle.

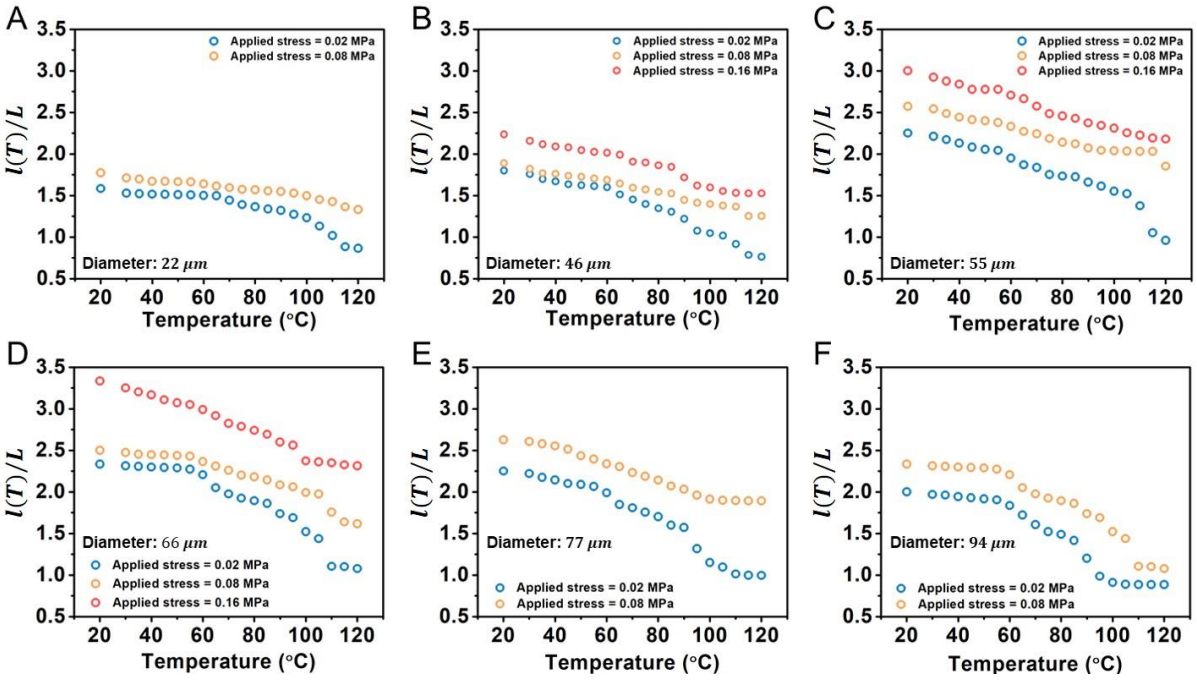

Figure 5.6: The dimensionless length change $l(T)/L$ of LCE fiber with different diameters (22 μm to 94 μm) as a function of temperature under three different levels of applied stress from 0.02 MPa to 0.16 MPa.

Notably, it is worth mentioning that in terms of the magnitude of actuation strain (> 50%), actuation stress (0.3 MPa), response speed (300%/s), work density (20 kJ/m^3), the LCE fiber exhibit comparable magnitude as human skeleton muscle (Figure 5.8). More importantly, compared with most developed LCE based soft actuators, taking advantage of the rapid actuation speed, the LCE fiber actuator exhibits relatively large power density (400 W/kg), which is two orders of magnitude higher than typical LCE based soft actuator (1 W/kg) as shown in Figure 5.5H.

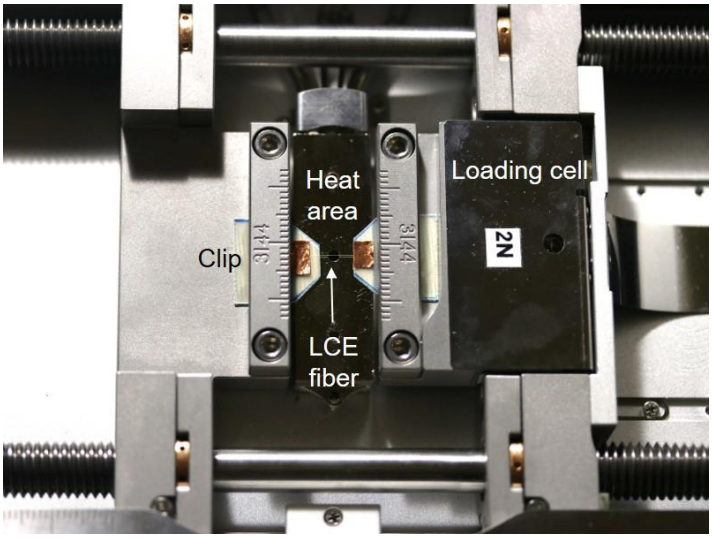

Figure 5.7: The real image of micro-tester. The LCE fiber is mounted between two clips. In the experiment, the length (strain) of the LCE fiber is fixed. The actuation stress can be measured as we gradually increase the temperature.

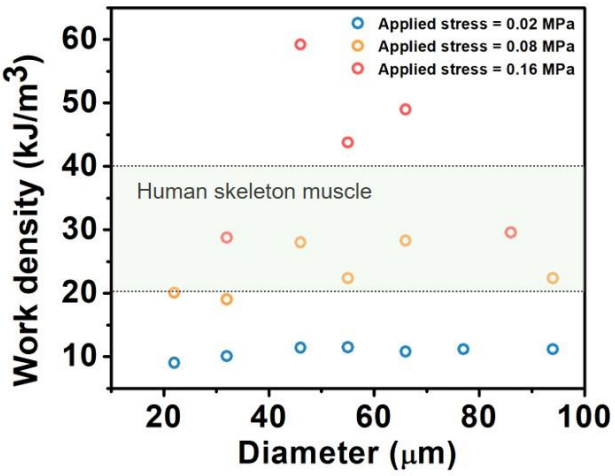

Figure 5.8: The work density of LCE fiber with different diameters. The magnitude of work density of LCE fiber is comparable to human skeleton muscle.

5.2.3 Oscillation of LCE fiber under gradient temperature field

The autonomous oscillation phenomenon can be broadly observed in nature as well as engineering system. The self-oscillation behavior does not require the on/off control of external stimulus, which greatly simplify the design of the actuator. Light-sensitive LCE based actuators have demonstrated self-oscillation behavior via self-shadowing effect under a constant light illumination. However, most oscillation modes are based on bending, for instance, the free-standing cantilever beams, which sometimes are not desired for the engineering applications. Here, we demonstrate the LCE fiber is able to generate unprecedented self-oscillation phenomenon under inhomogeneous temperature field, thanks to its high sensitivity to temperature.

The LCE fiber ($d = 33\ \mu m$ before stretching) is hung in a chamber (Figure 5.9A) where several heating wires are placed at the bottom to generate high temperature area. The bottom of the fiber is close to the heater whereas the top of the fiber is in room temperature area. The temperature distribution in the chamber can be measured by IR camera as shown in Figure 5.9B. The LCE fiber (with 0.02 MPa applied stress) immediately contracts and then elongates when it is suspended and placed inside of the chamber. Figure 5.9C shows the sequence frame of LCE fiber during the 16 to 17 second. The corresponding data of the entire oscillation is shown in Figure 5.9D. The LCE fiber exhibits the fully reversible continuous actuation in a chaotic fashion, the fiber contracts and elongates without regular frequency. The amplitude of the oscillation becomes smaller when the applied stress is increased. Quantitively, the dimensionless length ($l\ /L$) of LCE fiber decreases from 0.45 to 0.1 when the applied stress is increased from 0.02 MPa to 0.16 MPa.

We further analysis the data from Figure 5.9D by using the Fourier transformation to observe the frequency spectrum as shown in Figure 5.9E. The results indicate the oscillation is the combination of small amplitude component that fills the frequency to 2 Hz.

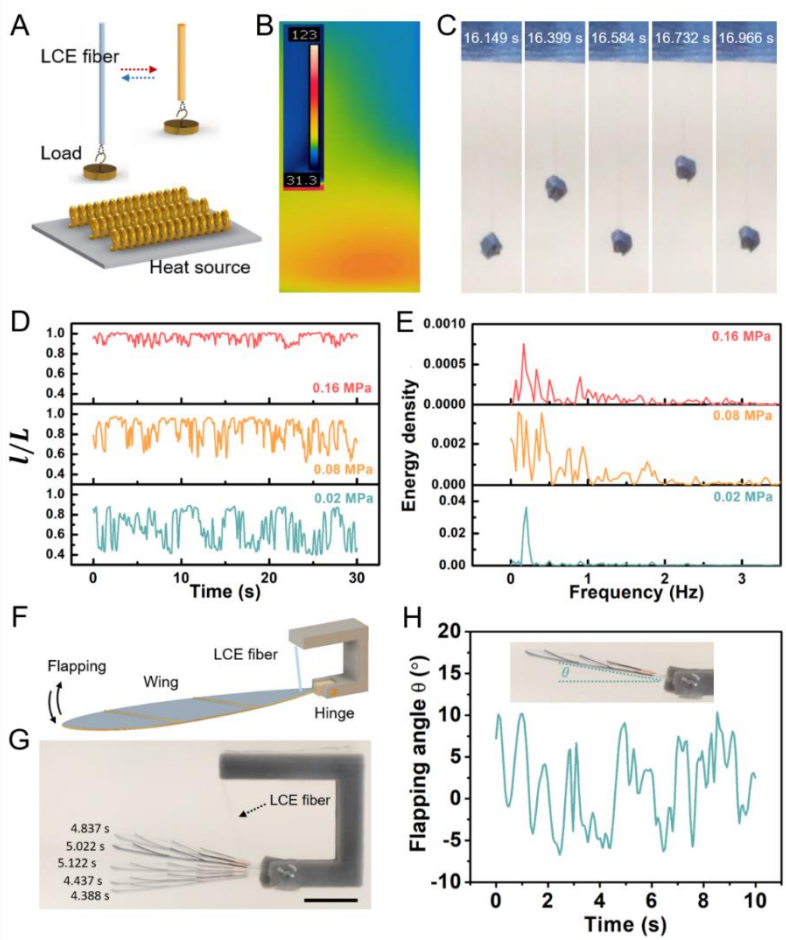

Figure 5.9: Oscillation of LCE fiber in gradient temperature field. A. Schematic illustration of the oscillation of monodomain LCE fiber under gradient temperature field. **B.** Thermal image of inhomogeneous temperature field measured by IR camera. **C.** Frames from video of the oscillation of LCE fiber (16 s to 17 s). **D.** Dimensionless length change of LCE fiber during oscillation with three different levels of applied stress from 0.02 MPa to 0.16 MPa. **E.** Frequency spectrum of the dimensionless length time series shown in Figure 3D. **F.** Schematic of the flapping wing induced by oscillation of LCE fiber. **G.** Frame from video of wing flapping. **H.** Flapping angle versus time during actuation. Scale bar in **F**: 10 mm.

To make use of the self-oscillation of LCE fiber, we further attach the plastic wing at the bottom of the LCE fiber to mimic the flapping motion of insects. The wing can move upward and downward as the LCE fiber continuously contracts and elongates which is shown in Figure 5.9F and 5.9G. The flapping motion of the plastic wing also exhibits chaotic fashion where the flapping angle has no regular frequency (Figure 5.9H).

5.2.4 Photothermal actuation of PDA-coated LCE fiber

Light, as a clean energy source, provides remotely, precisely, and instantly control to photosensitive LCE actuators which have been extensively studied. Among the light driven LCE actuator, polydopamine (PDA) coated LCE actuator exhibits several advantages such as stable photostability, high efficiency of energy conversion. To make LCE fiber optically responsive, we fabricate PDA-coated LCE fiber following simple method which only involve dip-coating process as shown in Figure 5.10A. Monodomain LCE fibers are submerged into dopamine/Tris based buffer solution. After 48 hours, the surface of LCE fiber turn into dark grey, which indicates the polymerization of dopamine at the surface of LCE fiber.

The PDA-coated LCE fiber can generate longitudinal contraction under the NIR light due to the photothermal effect (Figure 5.10B). In the experiment, to precisely control the frequency of NIR light, a rotating motor equipped with half opening mask are employed, which determine the time period of NIR light exposure.

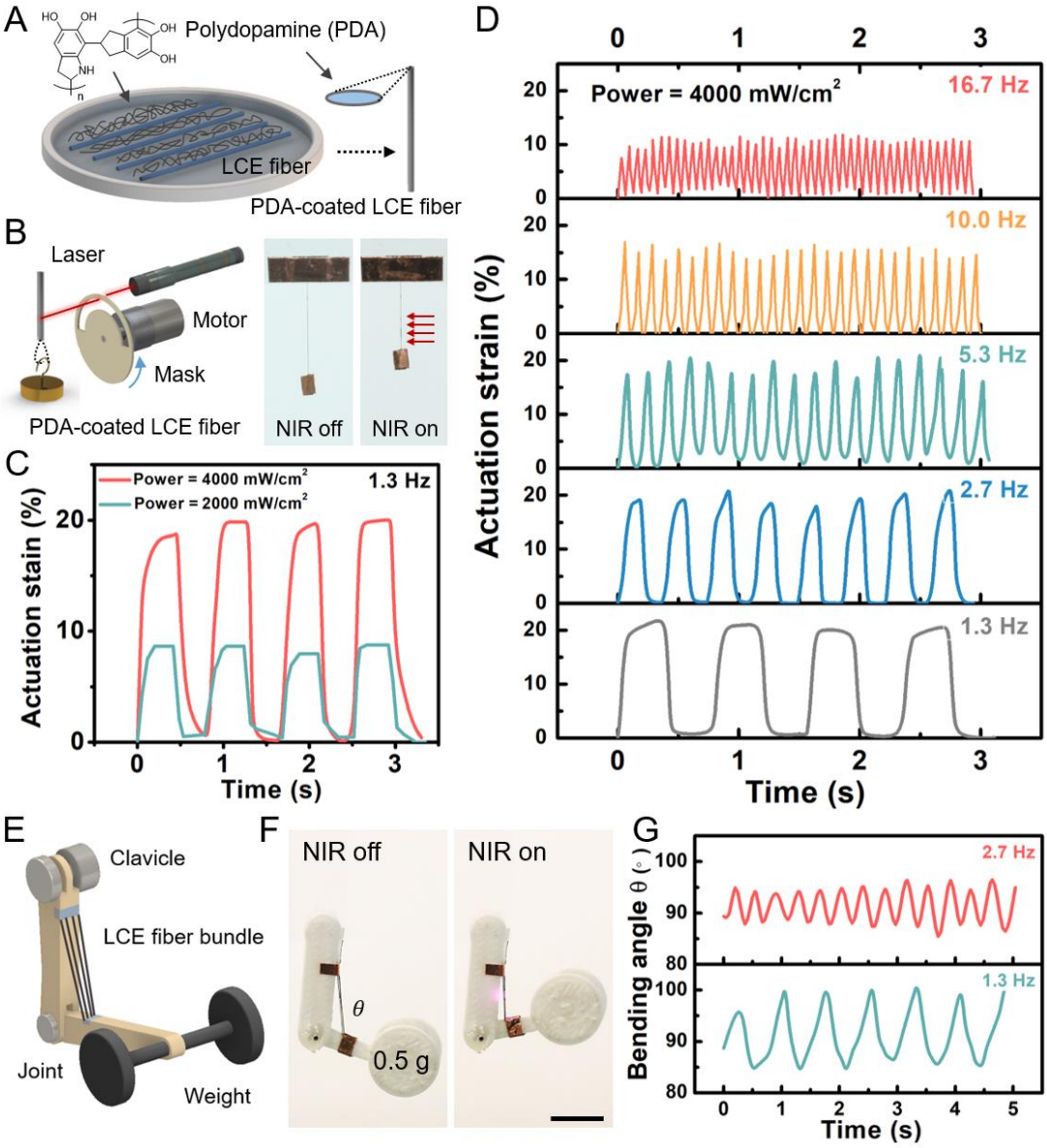

Figure 5.10: Photothermal actuation of PDA-coated LCE fiber. A. Preparation of Polydopamine (PDA)-coated monodomain LCE fiber via dip coating method. **B.** When the NIR light is applied to the PDA-coated LCE fiber, the LCE fiber contacts and lifts weight up. The frequency of NIR light can be controlled by the rotation speed of the motor. **C.** Actuation strain of PDA-coated LCE fiber as function of time under two laser beams with different powers. **D.** Influence of NIR light irradiation time on the actuation strain of PDA-coated LCE fiber. The maximum actuation strain is decreased when the frequency increases. **E.** Schematic of weight-lifting artificial limb, LCE fiber bundle can be implemented as bicep artificial muscle. **F.** When the NIR light is applied to the LCE fiber bundle, the bicep contracts, which moves the arm to bend at elbow. **G.** Plot of elbow bending angle θ as function of time at two different levels of frequency 1.3 Hz and 2.7 Hz. Scale bar in **F**: 10 mm.

To evaluate the actuation performance of PDA-coated LCE fiber under periodic NIR light, two laser beams with different levels of power are employed (Figure 5.10C). When the NIR light is exposed to the PDA-coated LCE fiber ($d = 35\ \mu m$), the actuation strain of LCE fiber increase instantaneously and then reach to the maximum values within short time period of 0.2 s. More importantly, the PDA-coated LCE fiber can rapidly recover to its initial length within 0.2 s when the NIR light is blocked, which indicates the ultrafast response of actuation as well as recovery. Moreover, the maximum actuation strain under higher laser power (4000 mW/cm^2) exhibits larger amplitude (20%) compared to lower power (2000 mW/cm^2). In addition, we also measure the response speed of PDA-coated LCE fiber with different diameters as shown in Figure 5.11, the LCE fiber with thinnest diameter exhibit both fast actuation as well as recovery compared with largest diameter of fiber.

We further study the actuation performance of PDA-coated LCE fiber ($d = 35\ \mu m$) under different frequency of NIR light exposure (4000 mW/cm^2). By controlling the rotating speed of the motor, the frequency of NIR light can be determined ranging from 1.3 Hz to 16.7 Hz. As shown in Figure 5.10D, at low frequency of 1.3 Hz, the actuation strain increases first and then reaches to the maximum plateau value (20%) which is corresponding to the steady state. When we further increase the frequency in the range of 2.7- 5.3 Hz, the maximum actuation strain maintains 20%. However, at relatively high frequency of 10.0 Hz and 16.7 Hz, the maximum actuation strain of PDA-coated LCE fiber decreases, the magnitude is 15% and 10% at frequency 10.0 Hz and 16.7

Hz, respectively. We finally conduct the durability tests of the PDA-coated LCE fiber. Its actuation strain remains unchanged (20%) after 2000 cycles under 5 Hz frequency (Figure 5.12).

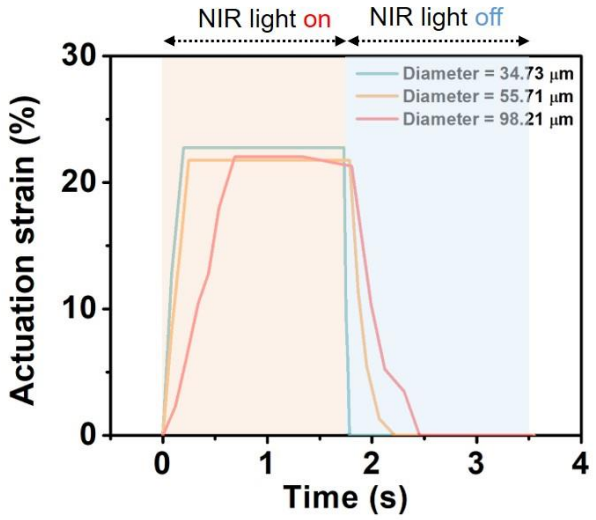

Figure 5.11: The response speed of PDA-coated LCE fiber with different diameters. Both the contraction and recovery speed decrease as the fiber diameter is increased.

Single fiber can produce modest force output, which may not be sufficient for certain application. To overcome this limitation, inspired by muscle bundle, we can amplify them by assembling multiple LCE fiber as shown in Figure 5.13. Single fiber ($d = 68\ \mu m$) can only lift 0.1 g weight while four such fibers can generate large force output to supply heavier weight (0.6 g) without affecting the response speed. We then implement PDA-coated LCE fiber bundle as bicep muscle to the 3D printed arm skeleton in order to realize the elbow movement (Figure 5.10E). Upon the LCE fiber bundle is activated by NIR light, it contracts, causing the arm bend of 85 ° and lift the weight of 0.5 g (Figure 5.10F). The PDA-coated LCE fiber bundle can be fully released upon the NIR light is switched off, causing the arm fully recovered. The implementations of

thermally driven materials as bicep muscle have been extensively demonstrated and well explored. However, the LCE fiber dominates in terms of the fast actuation and recovery speed. In Figure 5.10G, we show that the relationship between the bending angle of elbow and the time under periodic NIR light. The frequency of 1.3 and 2.7 Hz can be easily achieved.

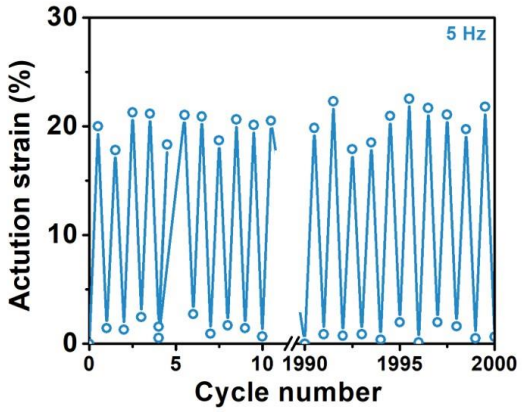

Figure 5.12: The cycling test of PDA-coated LCE fiber under 0.16 MPa applied stress. The frequency is 5 Hz.

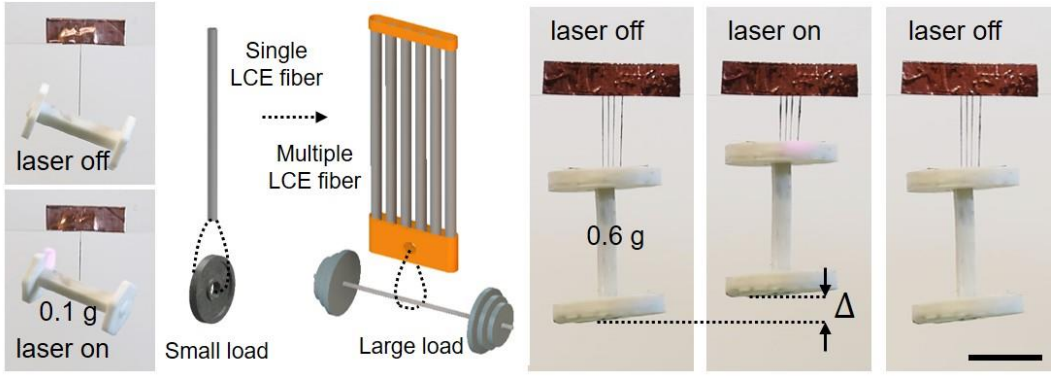

Figure 5.13: Multiple PDA-coated LCE fiber assembling. Demonstration of PDA-coated monodomain LCE fiber lift weight (0.1 g) under different frequency. Assembly of four PDA-coated monodomain LCE fiber. This design can increase the actuation force without affecting the response speed. Scale bar: 10 mm.

5.2.5 Micro machine and robotic applications of LCE fiber

The micro-scale size and rapid response of LCE fiber accompanied with large and reversible actuation endows it an ideal option to actuate microrobots and machines.

Electrically controlled soft actuators provide several obvious advantages such as simple system integration and programmable controllability, which is highly desired for micro-manipulation systems and devices. We design and fabricate the electrically controlled micro-tweezer that can be activated by LCE fiber. As shown in Figure 5.14A, the LCE fiber is mounted near the tip of two cantilever beams, two microheaters are attached to the inner sides of the beam. When the voltage is applied to the microheaters, Joule heat can be generated and then increase the temperature above the phase transition of LCE fiber. Therefore, the LCE fiber contracts which make the tip close (Figure 5.14B). The tip of the micro-tweezer can recover to open state when the applied voltage is switched off. The tip displacement can be precisely controlled by the applying different voltages, higher applied voltage enables larger tip movement as well as faster speed (Figure 5.14C).

Light driven LCE fiber can be precisely, rapidly, and remotely controlled, which make it an ideal choice the construct the untethered microrobot. We next fabricate micro-swimmer based on PDA-coated LCE fiber that can generate rapid movement on the water surface (Figure 5.14D). The micro-swimmer is mainly composed of flexible hinge, polyimide tape (with curved end), scotch tape, PEF film and PDA-coated LCE fiber. Although the density of the PET film (1.38 g/cm^3) is larger than the water, the micro-swimmer can still float on the water surface due to the

surface tension (Figure 5.14D). The micro-swimmer can generate movement by shielding of NIR, as the schematic illustrated in Figure 5E. For one swimming stroke, when the NIR is exposed to the PDA-coated LCE fiber, the fiber contracts due to photothermal effect, the entire structure folds. The front fin moves upward and then squeeze the water backward, which can generate thrust force that can push the entire body moving forward. The robot can still generate small displacement when the NIR light is switched off. With periodically NIR light switched on and off, the micro-swimmer generates large displacement (35 mm) on the water which is shown in Figure 5.14F.

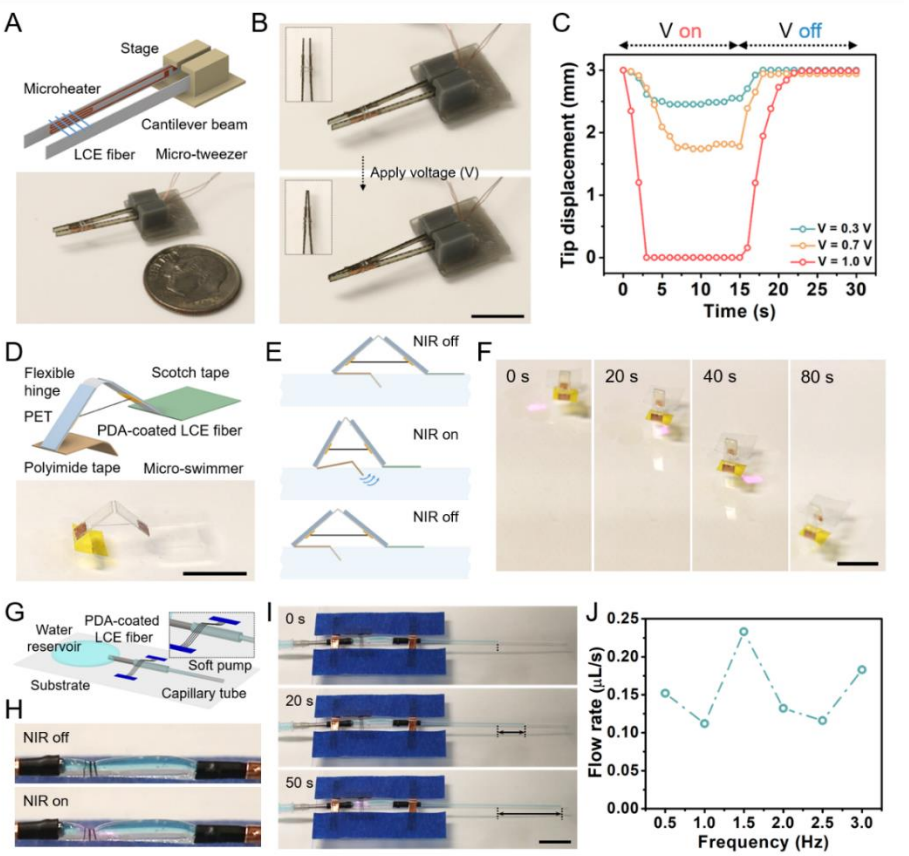

Figure 5.14: Micro machine and robotic applications of LCE fiber. A. Schematic and real image of micro-tweezer. The micro-tweezer is composed of two cantilever beams (equipped with microheater at the inner side), stage and LCE fiber. The LCE fiber is mounted near the tip of two cantilever beams. **B.** Operation principle of micro-tweezer. When the voltage is applied to two heaters, the LCE fiber can be heated up and then contract. Therefore, the tip of the tweezer is closed. **C.** Tip displacement of micro-tweezer versus time under three different levels of applied voltage: 0.3 V, 0.7 V and 1.0 V. **D.** Schematic and real image of micro-swimmer. The micro-swimmer is mainly composed of flexible hinge, PET films, polyimide tape, scotch tape and LCE fiber. **E.** Schematic illustration of micro-swimmer during actuation. When the LCE fiber is exposed to the NIR light, the LCE fiber contracts, the front fin moves upward and squeezes the water backward, which generates thrust force that can push the entire body moving forward. **F.** Frames from the video of micro-swimmer during actuation. **G.** Schematic of soft pump. Several PDA-coated LCE fibers are placed onto the soft tube made from Ecoflex. A metallic needle is used to connect the soft tube and the water reservoir. Another capillary tube is connected to the soft tube enabling the observation of water movement. **H.** When NIR light is applied to the PDA-coated LCE fiber, the soft tube deforms and, the water inside of the soft tube is squeezed to the right direction. **I.** Frames from the videos of soft pump during actuation at a frequency of 1 Hz. **J.** The flow rate of soft pump versus the frequency of the actuation of LCE fiber. Scale bar in **B**, **D**, **F, I**: 10 mm.

Finally, we demonstrate the soft micro impedance pump driven by PDA-coated LCE fiber (Figure 5.14G). The soft impedance pump is comprised of a soft tube in the middle, two rigid tubes at both ends. Several PDA-coated LCE fibers are employed onto the soft tube because of its large actuation and fast speed. When NIR is applied to the LCE fibers, the soft tube deforms due to the local contraction of LCE fibers (Figure 5.14H). Water inside of the soft tube can be squeezed and move to the right. The fundamental operation principle of the soft impedance pump is the asymmetrically periodic excitation with respect to the fluid which has been broadly studied in previous studies. Therefore, by applying the periodic NIR to the PDA-coated LCE fibers, the soft tube in the middle continuously deform and release, the wave forms resulting in the accumulation of pressure gradient which can drive the water. Figure 5I and Movies S10 demonstrate the water can be successfully driven to move forward under the periodic NIR with certain frequency. The flow rate of the soft impedance pump is calculated and shown in Figure 5.14J, using 1.5 Hz frequency excitation, the flow rate can be measured as 0.24 μL/s which is comparable to the previous study.

5.3 Conclusion

In this chapter, we design and fabricate one dimensional LCE fiber via electrospinning technique. We then characterize the actuation performance of the LCE fiber. Notably, the LCE fiber exhibits similar performance as real human skeleton muscle in terms of the actuation strain, stress, response speed, work density and power density. To better control the LCE fiber, we use

NIR as stimuli to trigger the actuation. In addition, taking advantage of the small scale of the LCE fiber, it can be easily integrated to any micro robotic and machine systems as micro actuator. Our work not only develop a new approach to design new type of micro actuator but also demonstrate how to control and make use of it, which opens up avenue to micro actuators and systems.

It is worth mentioning that the diameter of the LCE fiber made from electrospinning has broad variation and cannot be precisely controlled, which may cause inconvenience in multi-fiber assembling. However, there are more than 500 LCE fibers can be fabricated from one time electrospinning, LCE fiber with similar dimension can be selected from one batch. In addition, compared with the previous Electrospun LCE fiber, the diameter of LCE fiber in this work is one order of magnitude larger because of the high concentration (20%) of the ink and small applied voltage (6 kV) during electrospinning process. Although the response speed can be further optimized by simply reducing the size, the force output may also weaken, which is not favorable for most micro scale applications.

Chapter 5, in full, is currently being prepared for publication by Qiguang He, Zhijian Wang, Yang Wang, Zijun Wang, Chenghai Li, Jian Zeng, Raja Annapooranan, Renkun Chen and Shengqiang Cai. The dissertation author was the primary investigator and first author of this paper.

Chapter 6 Conclusion

6.1 Summary of the dissertation

Liquid crystal elastomer (LCE) is a good option to construct the artificial muscle and soft robotics, its actuation performance such as actuation strain, actuation stress, work density is all comparable to the human skeleton muscle. Moreover, the versatile deformation modes of LCE can be achieved by simply programming the orientation of liquid crystal mesogens. In this dissertation, we bridge the gap between the soft actuating material LCE and the practical engineering applications. We design and fabricate multiple methods and develop new materials to enable LCE based soft actuators to have facile controllability, multiple functionalities, fast actuating response speed, broad operation temperature, repairability, recyclability. The experimental results clearly verify these unique characteristics. The main results of each chapter are summarized as follows:

In Chapter 2, we design and construct soft tubular actuators using an emerging artificial muscle material that can be easily patterned with programmable strain: liquid crystal elastomer. Controlled by an externally applied electrical potential, the tubular actuator can exhibit multidirectional bending as well as large (~40%) homogenous contraction. Using multiple tubular actuators, we build a multifunctional soft gripper and an untethered soft robot. These soft machines all have multiple functionalities.

In Chapter 3, inspired by biology, we design and fabricate a vascular LCE-based artificial muscle (VLAM) with internal fluidic channel in which we inject hot or cool water to heat up or

cool down the material to achieve fast actuation as well as recovery. We demonstrate that the actuation stress, strain and cyclic response rate of the VLAM are comparable to mammalian skeletal muscle. Because of the internal heating and cooling mechanism, VLAM shows very robust actuating performance within wide range of environmental temperature. The VLAM designed in this article may also provide a convenient way to harvest waste heat to conduct mechanical work.

In Chapter 4, we develop fluid-driven disulfide LCE actuators through facile laminate manufacturing enabled by dynamic bonds exchange reaction. Owing to the merits of active heating/cooling mechanism of the fluidic structure, this newly developed disulfide LCE actuator can generate large cyclic actuation at a frequency around 1 Hz and can also operate in a wide range of temperature. The unique combination of the fluidic structure design and the dynamic covalent bonds in the elastomer has also enabled the full recyclability and self-repairability of the actuator. Using the newly developed actuator as building block, we further construct soft robotic systems that can realize manipulating and programmable movement. The design principle demonstrated in the current work opens a promising avenue for exploring more novel applications of LCE-based soft actuator.

In Chapter 5, using the electrospinning technique, we design and fabricate micro sized liquid crystal elastomer (LCE) based artificial muscle that exhibits large actuation strain (~60%), fast response speed (<0.2 s) and high power density (400 W/kg). The size and actuation performance of LCE fiber are all comparable to human skeleton muscle. Additionally, the LCE fiber shows self-oscillation performance in gradient temperature field. Moreover, the actuation of LCE fiber

can be remotely and precisely controlled by applying NIR light via photothermal mechanism. Finally, we demonstrate that the LCE fiber can be implemented into micro-robotic and micro machines such as tweezer, swimmer, and soft impendent pump, showing the feasibility and versatile functionalities of LCE fiber in micro systems.

6.2 Outlook for future work

Few challenges are still existed in LCE base soft actuators, which may further limit their applications. Although the actuation performance of LCE is very similar to human skeleton muscle, it still cannot be used to replace the real muscle. The instinct problem is the nematic-isotropic phase transition temperature of LCE is high (> 60 °C), which is not suitable for human being with body temperature around 35 °C. Therefore, it requires the development of new LCE materials with low transition temperature. In addition, since LCE is thermally-driven materials, the energy efficiency is extremely low (< 1%), which is not desirable for the entire system. The future works may develop new methods to activate the LCE based soft actuators with more efficient ways.

Bibliography

1. Rus, D. and Tolley, M.T., 2015. Design, fabrication and control of soft robots. Nature, 521(7553), pp.467-475.

2. Ilievski, F., Mazzeo, A.D., Shepherd, R.F., Chen, X. and Whitesides, G.M., 2011. Soft robotics for chemists. Angewandte Chemie, 123(8), pp.1930-1935.

3. Tolley, M.T., Shepherd, R.F., Mosadegh, B., Galloway, K.C., Wehner, M., Karpelson, M., Wood, R.J. and Whitesides, G.M., 2014. A resilient, untethered soft robot. Soft robotics, 1(3), pp.213-223.

4. Polygerinos, P., Wang, Z., Galloway, K.C., Wood, R.J. and Walsh, C.J., 2015. Soft robotic glove for combined assistance and at-home rehabilitation. Robotics and Autonomous Systems, 73, pp.135-143.

5. Yu, C., Duan, Z., Yuan, P., Li, Y., Su, Y., Zhang, X., Pan, Y., Dai, L.L., Nuzzo, R.G., Huang, Y. and Jiang, H., 2013. Electronically Programmable, Reversible Shape Change in Two-and Three-Dimensional Hydrogel Structures. Advanced Materials, 25(11), pp.1541-1546.

6. Keplinger, C., Sun, J.Y., Foo, C.C., Rothemund, P., Whitesides, G.M. and Suo, Z., 2013. Stretchable, transparent, ionic conductors. Science, 341(6149), pp.984-987.

7. Meng, H. and Li, G., 2013. A review of stimuli-responsive shape memory polymer composites. Polymer, 54(9), pp.2199-2221.

8. Mosadegh, B., Polygerinos, P., Keplinger, C., Wennstedt, S., Shepherd, R.F., Gupta, U., Shim, J., Bertoldi, K., Walsh, C.J. and Whitesides, G.M., 2014. Pneumatic networks for soft robotics that actuate rapidly. Advanced functional materials, 24(15), pp.2163-2170.

9. Yuk, H., Lin, S., Ma, C., Takaffoli, M., Fang, N.X. and Zhao, X., 2017. Hydraulic hydrogel actuators and robots optically and sonically camouflaged in water. Nature communications, 8(1), pp.1-12.

10. Spillmann, C.M., Naciri, J., Martin, B.D., Farahat, W., Herr, H. and Ratna, B.R., 2007. Stacking nematic elastomers for artificial muscle applications. Sensors and Actuators A: Physical, 133(2), pp.500-505.

11. Zeng, H., Wani, O.M., Wasylczyk, P., Kaczmarek, R. and Priimagi, A., 2017. Self-regulating

iris based on light-actuated liquid crystal elastomer. Advanced materials, 29(30), p.1701814.

12. Rogóż, M., Zeng, H., Xuan, C., Wiersma, D.S. and Wasylczyk, P., 2016. Light-driven soft robot mimics caterpillar locomotion in natural scale. Advanced Optical Materials, 4(11), pp.1689-1694.

13. Ahn, C., Liang, X. and Cai, S., 2015. Inhomogeneous stretch induced patterning of molecular orientation in liquid crystal elastomers. Extreme Mechanics Letters, 5, pp.30-36.

14. Bisoyi, H.K. and Li, Q., 2016. Light-driven liquid crystalline materials: from photo-induced phase transitions and property modulations to applications. Chemical reviews, 116(24), pp.15089-15166.

15. Boothby, J.M., Kim, H. and Ware, T.H., 2017. Shape changes in chemoresponsive liquid crystal elastomers. Sensors and Actuators B: Chemical, 240, pp.511-518.

16. Saed, M.O., Torbati, A.H., Nair, D.P. and Yakacki, C.M., 2016. Synthesis of programmable main-chain liquid-crystalline elastomers using a two-stage thiol-acrylate reaction. Journal of visualized experiments: JoVE, (107).

17. Yakacki, C.M., Saed, M., Nair, D.P., Gong, T., Reed, S.M. and Bowman, C.N., 2015. Tailorable and programmable liquid-crystalline elastomers using a two-stage thiol–acrylate reaction. Rsc Advances, 5(25), pp.18997-19001.

18. Kotikian, A., Truby, R.L., Boley, J.W., White, T.J. and Lewis, J.A., 2018. 3D printing of liquid crystal elastomeric actuators with spatially programed nematic order. Advanced Materials, 30(10), p.1706164.

19. Wang, Z., Wang, Z., Zheng, Y., He, Q., Wang, Y. and Cai, S., 2020. Three-dimensional printing of functionally graded liquid crystal elastomer. Science advances, 6(39), p.eabc0034.

20. Davidson, E.C., Kotikian, A., Li, S., Aizenberg, J. and Lewis, J.A., 2020. 3D printable and reconfigurable liquid crystal elastomers with light-induced shape memory via dynamic bond exchange. Advanced Materials, 32(1), p.1905682.

21. Wang, Z., Tian, H., He, Q. and Cai, S., 2017. Reprogrammable, reprocessible, and self-healable liquid crystal elastomer with exchangeable disulfide bonds. ACS applied materials & interfaces, 9(38), pp.33119-33128.

22. Wang, Z., He, Q., Wang, Y. and Cai, S., 2019. Programmable actuation of liquid crystal elastomers via “living” exchange reaction. Soft matter, 15(13), pp.2811-2816.

23. He, Q., Wang, Z., Wang, Y., Minori, A., Tolley, M.T. and Cai, S., 2019. Electrically controlled liquid crystal elastomer–based soft tubular actuator with multimodal actuation. Science advances, 5(10), p.eaax5746.

24. Wang, C., Sim, K., Chen, J., Kim, H., Rao, Z., Li, Y., Chen, W., Song, J., Verduzco, R. and Yu, C., 2018. Soft ultrathin electronics innervated adaptive fully soft robots. Advanced Materials, 30(13), p.1706695.

25. He, Q., Wang, Z., Song, Z. and Cai, S., 2019. Bioinspired design of vascular artificial muscle. Advanced Materials Technologies, 4(1), p.1800244.

26. He, Q., Wang, Z., Wang, Y., Song, Z. and Cai, S., 2020. Recyclable and self-repairable fluid-driven liquid crystal elastomer actuator. ACS Applied Materials & Interfaces, 12(31), pp.35464-35474.

27. Jiang, Z.C., Xiao, Y.Y. and Zhao, Y., 2019. Shining light on liquid crystal polymer networks: Preparing, reconfiguring, and driving soft actuators. Advanced Optical Materials, 7(16), p.1900262.

28. Jiang, Z.C., Xiao, Y.Y., Yin, L., Han, L. and Zhao, Y., 2020. “Self-Lockable” Liquid Crystalline Diels–Alder Dynamic Network Actuators with Room Temperature Programmability and Solution Reprocessability. Angewandte Chemie, 132(12), pp.4955-4961.

29. He, Q., Zheng, Y., Wang, Z., He, X. and Cai, S., 2020. Anomalous inflation of a nematic balloon. Journal of the Mechanics and Physics of Solids, p.104013.

30. Davidson, Z.S., Shahsavan, H., Aghakhani, A., Guo, Y., Hines, L., Xia, Y., Yang, S. and Sitti, M., 2019. Monolithic shape-programmable dielectric liquid crystal elastomer actuators. Science advances, 5(11), p.eaay0855.

31. Ahn, C., Liang, X. and Cai, S., 2019. Bioinspired design of light-powered crawling, squeezing, and jumping untethered soft robot. Advanced Materials Technologies, 4(7), p.1900185.

32. Zeng, H., Wani, O.M., Wasylczyk, P. and Priimagi, A., 2018. Light-driven, caterpillar-inspired miniature inching robot. Macromolecular rapid communications, 39(1), p.1700224.

33. Palagi, S., Mark, A.G., Reigh, S.Y., Melde, K., Qiu, T., Zeng, H., Parmeggiani, C., Martella, D., Sanchez-Castillo, A., Kapernaum, N. and Giesselmann, F., 2016. Structured light enables biomimetic swimming and versatile locomotion of photoresponsive soft microrobots. Nature materials, 15(6), pp.647-653.

34. Wang, M., Lin, B.P. and Yang, H., 2016. A plant tendril mimic soft actuator with phototunable bending and chiral twisting motion modes. Nature communications, 7(1), pp.1-8.

35. Schuhladen, S., Preller, F., Rix, R., Petsch, S., Zentel, R. and Zappe, H., 2014. Iris-Like Tunable Aperture Employing Liquid-Crystal Elastomers. Advanced materials, 26(42), pp.7247-7251.

36. Minori, A.F., He, Q., Glick, P.E., Adibnazari, I., Stopol, A., Cai, S. and Tolley, M.T., 2020. Reversible actuation for self-folding modular machines using liquid crystal elastomer. Smart Materials and Structures, 29(10), p.105003.

37. Minori, A., Jadhav, S., He, Q., Cai, S. and Tolley, M.T., 2017, September. Reversible actuation of origami inspired composites using liquid crystal elastomers. In Smart Materials, Adaptive Structures and Intelligent Systems (Vol. 58257, p. V001T08A015). American Society of Mechanical Engineers.

38. Wang, Z., Fan, W., He, Q., Wang, Y., Liang, X. and Cai, S., 2017. A simple and robust way towards reversible mechanochromism: Using liquid crystal elastomer as a mask. Extreme Mechanics Letters, 11, pp.42-48.

39. Gilbert, H.B., Rucker, D.C. and Webster III, R.J., 2016. Concentric tube robots: The state of the art and future directions. Robotics Research, pp.253-269.

40. Dupont, P.E., Lock, J., Itkowitz, B. and Butler, E., 2009. Design and control of concentric-tube robots. IEEE Transactions on Robotics, 26(2), pp.209-225.

41. Madhani, A.J., Niemeyer, G. and Salisbury, J.K., 1998, October. The black falcon: a teleoperated surgical instrument for minimally invasive surgery. In Proceedings. 1998 IEEE/RSJ International Conference on Intelligent Robots and Systems. Innovations in Theory, Practice and Applications (Cat. No. 98CH36190) (Vol. 2, pp. 936-944). IEEE.

42. Xu, K. and Simaan, N., 2008. An investigation of the intrinsic force sensing capabilities of continuum robots. IEEE Transactions on Robotics, 24(3), pp.576-587.

43. Degani, A., Choset, H., Wolf, A. and Zenati, M.A., 2006, May. Highly articulated robotic probe for minimally invasive surgery. In Proceedings 2006 IEEE International Conference on Robotics and Automation, 2006. ICRA 2006. (pp. 4167-4172). IEEE.

44. Christianson, C., Goldberg, N.N., Deheyn, D.D., Cai, S. and Tolley, M.T., 2018. Translucent soft robots driven by frameless fluid electrode dielectric elastomer actuators. Science Robotics, 3(17).

45. Whitesides, G.M., 2018. Soft robotics. Angewandte Chemie International Edition, 57(16), pp.4258-4273.

46. Martinez, R.V., Branch, J.L., Fish, C.R., Jin, L., Shepherd, R.F., Nunes, R.M., Suo, Z. and Whitesides, G.M., 2013. Robotic tentacles with three-dimensional mobility based on flexible elastomers. Advanced materials, 25(2), pp.205-212.

47. Laschi, C., Cianchetti, M., Mazzolai, B., Margheri, L., Follador, M. and Dario, P., 2012. Soft robot arm inspired by the octopus. Advanced robotics, 26(7), pp.709-727.

48. Hannan, M.W. and Walker, I.D., 2003. Kinematics and the implementation of an elephant's trunk manipulator and other continuum style robots. Journal of robotic systems, 20(2), pp.45-63.

49. Seok, S., Onal, C.D., Cho, K.J., Wood, R.J., Rus, D. and Kim, S., 2012. Meshworm: a peristaltic soft robot with antagonistic nickel titanium coil actuators. IEEE/ASME Transactions on mechatronics, 18(5), pp.1485-1497.

50. Marchese, A.D., Komorowski, K., Onal, C.D. and Rus, D., 2014, May. Design and control of a soft and continuously deformable 2d robotic manipulation system. In 2014 IEEE international conference on robotics and automation (ICRA) (pp. 2189-2196). Ieee.

51. Onal, C.D. and Rus, D., 2013. Autonomous undulatory serpentine locomotion utilizing body dynamics of a fluidic soft robot. Bioinspiration & biomimetics, 8(2), p.026003.

52. Drotman, D., Ishida, M., Jadhav, S. and Tolley, M.T., 2018. Application-driven design of soft, 3-D printed, pneumatic actuators with bellows. IEEE/ASME Transactions on Mechatronics, 24(1), pp.78-87.

53. Mirvakili, S.M. and Hunter, I.W., 2018. Artificial muscles: Mechanisms, applications, and challenges. Advanced Materials, 30(6), p.1704407.

54. Li, Q. ed., 2013. Intelligent stimuli-responsive materials: from well-defined nanostructures to applications. John Wiley & Sons.

55. Ohm, C., Brehmer, M. and Zentel, R., 2010. Liquid crystalline elastomers as actuators and sensors. Advanced Materials, 22(31), pp.3366-3387.

56. White, T.J. and Broer, D.J., 2015. Programmable and adaptive mechanics with liquid crystal polymer networks and elastomers. Nature materials, 14(11), pp.1087-1098.

57. Pei, Z., Yang, Y., Chen, Q., Terentjev, E.M., Wei, Y. and Ji, Y., 2014. Mouldable liquid-crystalline elastomer actuators with exchangeable covalent bonds. Nature materials, 13(1), pp.36-41.

58. Ula, S.W., Traugutt, N.A., Volpe, R.H., Patel, R.R., Yu, K. and Yakacki, C.M., 2018. Liquid crystal elastomers: an introduction and review of emerging technologies. Liquid Crystals Reviews, 6(1), pp.78-107.

59. Qian, X., Chen, Q., Yang, Y., Xu, Y., Li, Z., Wang, Z., Wu, Y., Wei, Y. and Ji, Y., 2018. Untethered recyclable tubular actuators with versatile locomotion for soft continuum robots. Advanced Materials, 30(29), p.1801103.

60. Wang, Z., Li, K., He, Q. and Cai, S., 2019. A Light-Powered Ultralight Tensegrity Robot with High Deformability and Load Capacity. Advanced Materials, 31(7), p.1806849.

61. Gelebart, A.H., Mulder, D.J., Varga, M., Konya, A., Vantomme, G., Meijer, E.W., Selinger, R.L. and Broer, D.J., 2017. Making waves in a photoactive polymer film. Nature, 546(7660), pp.632-636.

62. Tian, H., Wang, Z., Chen, Y., Shao, J., Gao, T. and Cai, S., 2018. Polydopamine-coated main-chain liquid crystal elastomer as optically driven artificial muscle. ACS applied materials & interfaces, 10(9), pp.8307-8316.

63. Liu, L., Liu, M.H., Deng, L.L., Lin, B.P. and Yang, H., 2017. Near-infrared chromophore functionalized soft actuator with ultrafast photoresponsive speed and superior mechanical property. Journal of the American Chemical Society, 139(33), pp.11333-11336.

64. Pei, Z., Yang, Y., Chen, Q., Wei, Y. and Ji, Y., 2016. Regional shape control of strategically assembled multishape memory vitrimers. Advanced Materials, 28(1), pp.156-160.

65. Bisoyi, H.K., Urbas, A.M. and Li, Q., 2019. Soft materials driven by photothermal effect and their applications. Photoactive Functional Soft Materials: Preparation, Properties, and Applications, pp.1-44.

66. Petsch, S., Rix, R., Reith, P., Khatri, B., Schuhladen, S., Ruh, D., Zentel, R. and Zappe, H., 2014, January. A thermotropic liquid crystal elastomer micro-actuator with integrated deformable micro-heater. In 2014 IEEE 27th International Conference on Micro Electro Mechanical Systems (MEMS) (pp. 905-908). IEEE.

67. Clark, R.A., 1964. The bending and stretching of plates (EH Mansfield). SIAM Review, 6(4), p.468.

68. Messner, P.W.C., Paik, J., Shepherd, R., Kim, S. and Trimmer, B.A., 2014. Energy for biomimetic robots: challenges and solutions. Soft Robotics, 1(2), pp.106-109.

69. Yuan, C., Roach, D.J., Dunn, C.K., Mu, Q., Kuang, X., Yakacki, C.M., Wang, T.J., Yu, K. and Qi, H.J., 2017. 3D printed reversible shape changing soft actuators assisted by liquid crystal elastomers. Soft Matter, 13(33), pp.5558-5568.

70. Gu, G., Zou, J., Zhao, R., Zhao, X. and Zhu, X., 2018. Soft wall-climbing robots. Science Robotics, 3(25).

71. Miriyev, A., Stack, K. and Lipson, H., 2017. Soft material for soft actuators. Nature communications, 8(1), pp.1-8.

72. Marchese, A.D., Onal, C.D. and Rus, D., 2014. Autonomous soft robotic fish capable of escape maneuvers using fluidic elastomer actuators. Soft robotics, 1(1), pp.75-87.

73. Wehner, M., Tolley, M.T., Mengüç, Y., Park, Y.L., Mozeika, A., Ding, Y., Onal, C., Shepherd, R.F., Whitesides, G.M. and Wood, R.J., 2014. Pneumatic energy sources for autonomous and wearable soft robotics. Soft robotics, 1(4), pp.263-274.

74. Petersen, K.H. and Shepherd, R.F., 2019. Fluid-driven intrinsically soft robots. In Robotic Systems and Autonomous Platforms (pp. 61-84). Woodhead Publishing.

75. Liu, Y., Zhang, K., Ma, J. and Vancso, G.J., 2017. Thermoresponsive semi-IPN hydrogel microfibers from continuous fluidic processing with high elasticity and fast actuation. ACS applied materials & interfaces, 9(1), pp.901-908.

76. Acome, E., Mitchell, S.K., Morrissey, T.G., Emmett, M.B., Benjamin, C., King, M., Radakovitz, M. and Keplinger, C., 2018. Hydraulically amplified self-healing electrostatic actuators with muscle-like performance. Science, 359(6371), pp.61-65.

77. Kellaris, N., Venkata, V.G., Smith, G.M., Mitchell, S.K. and Keplinger, C., 2018. Peano-HASEL actuators: Muscle-mimetic, electrohydraulic transducers that linearly contract on activation. Science Robotics, 3(14).

78. Kuang, X., Chen, K., Dunn, C.K., Wu, J., Li, V.C. and Qi, H.J., 2018. 3D printing of highly stretchable, shape-memory, and self-healing elastomer toward novel 4D printing. ACS applied materials & interfaces, 10(8), pp.7381-7388.

79. Yang, D., Verma, M.S., So, J.H., Mosadegh, B., Keplinger, C., Lee, B., Khashai, F., Lossner, E., Suo, Z. and Whitesides, G.M., 2016. Buckling pneumatic linear actuators inspired by muscle. Advanced Materials Technologies, 1(3), p.1600055.

80. Haines, C.S., Lima, M.D., Li, N., Spinks, G.M., Foroughi, J., Madden, J.D., Kim, S.H., Fang, S., De Andrade, M.J., Göktepe, F. and Göktepe, Ö., 2014. Artificial muscles from fishing line and sewing thread. science, 343(6173), pp.868-872.

81. Bar-Cohen, Y. and Anderson, I.A., 2019. Electroactive polymer (EAP) actuators—background review. Mechanics of Soft Materials, 1(1), pp.1-14.

82. Terryn, S., Brancart, J., Lefeber, D., Van Assche, G. and Vanderborght, B., 2017. Self-healing soft pneumatic robots. Science Robotics, 2(9).

83. Li, S., Vogt, D.M., Rus, D. and Wood, R.J., 2017. Fluid-driven origami-inspired artificial muscles. Proceedings of the National academy of Sciences, 114(50), pp.13132-13137.

84. Chou, C.P. and Hannaford, B., 1996. Measurement and modeling of McKibben pneumatic artificial muscles. IEEE Transactions on robotics and automation, 12(1), pp.90-102.

85. Yap, H.K., Ng, H.Y. and Yeow, C.H., 2016. High-force soft printable pneumatics for soft robotic applications. Soft Robotics, 3(3), pp.144-158.

86. Robertson, M.A., Sadeghi, H., Florez, J.M. and Paik, J., 2017. Soft pneumatic actuator fascicles for high force and reliability. Soft robotics, 4(1), pp.23-32.

87. Xia, Y., Cedillo-Servin, G., Kamien, R.D. and Yang, S., 2016. Guided folding of nematic

liquid crystal elastomer sheets into 3D via patterned 1D microchannels. Advanced Materials, 28(43), pp.9637-9643.

88. Li, Q., 2012. Liquid crystals beyond displays: chemistry, physics, and applications. John Wiley & Sons.

89. Ambulo, C.P., Burroughs, J.J., Boothby, J.M., Kim, H., Shankar, M.R. and Ware, T.H., 2017. Four-dimensional printing of liquid crystal elastomers. ACS applied materials & interfaces, 9(42), pp.37332-37339.

90. Li, J., Wong, W.Y. and Tao, X.M., 2020. Recent advances in soft functional materials: preparation, functions and applications. Nanoscale, 12(3), pp.1281-1306.

91. Felton, S., Tolley, M., Demaine, E., Rus, D. and Wood, R., 2014. A method for building self-folding machines. Science, 345(6197), pp.644-646. Felton, S., Tolley, M., Demaine, E., Rus, D. and Wood, R., 2014. A method for building self-folding machines. Science, 345(6197), pp.644-646.

92. Mirvakili, S.M. and Hunter, I.W., 2017. Multidirectional artificial muscles from nylon. Advanced Materials, 29(4), p.1604734.

93. Madden, J.D., Vandesteeg, N.A., Anquetil, P.A., Madden, P.G., Takshi, A., Pytel, R.Z., Lafontaine, S.R., Wieringa, P.A. and Hunter, I.W., 2004. Artificial muscle technology: physical principles and naval prospects. IEEE Journal of oceanic engineering, 29(3), pp.706-728.

94. Perry, S.F. and Wood, C.M., 1989. Control and coordination of gas transfer in fishes. Canadian Journal of Zoology, 67(12), pp.2961-2970.

95. Kusters, Y.H. and Barrett, E.J., 2016. Muscle microvasculature's structural and functional specializations facilitate muscle metabolism. American Journal of Physiology-Endocrinology and Metabolism, 310(6), pp.E379-E387.

96. Majidi, C., 2014. Soft robotics: a perspective—current trends and prospects for the future. Soft robotics, 1(1), pp.5-11.

97. Ionov, L., 2014. Hydrogel-based actuators: possibilities and limitations. Materials Today, 17(10), pp.494-503.

98. Warner, M. and Terentjev, E.M., 2007. Liquid crystal elastomers (Vol. 120). Oxford university

press.

99. Pang, X., Lv, J.A., Zhu, C., Qin, L. and Yu, Y., 2019. Photodeformable Azobenzene-Containing Liquid Crystal Polymers and Soft Actuators. Advanced Materials, 31(52), p.1904224.

100. Wermter, H. and Finkelmann, H., 2001. Liquid crystalline elastomers as artificial muscles. e-Polymers, 1(1).

101. Wani, O.M., Zeng, H. and Priimagi, A., 2017. A light-driven artificial flytrap. Nature communications, 8(1), pp.1-7.

102. Kotikian, A., McMahan, C., Davidson, E.C., Muhammad, J.M., Weeks, R.D., Daraio, C. and Lewis, J.A., 2019. Untethered soft robotic matter with passive control of shape morphing and propulsion. Science Robotics, 4(33).

103. Ahn, C., Li, K. and Cai, S., 2018. Light or thermally powered autonomous rolling of an elastomer rod. ACS applied materials & interfaces, 10(30), pp.25689-25696.

104. Zeng, H., Wasylczyk, P., Parmeggiani, C., Martella, D., Burresi, M. and Wiersma, D.S., 2015. Light-fueled microscopic walkers. Advanced Materials, 27(26), pp.3883-3887.

105. Serak, S., Tabiryan, N., Vergara, R., White, T.J., Vaia, R.A. and Bunning, T.J., 2010. Liquid crystalline polymer cantilever oscillators fueled by light. Soft Matter, 6(4), pp.779-783.

106. Wang, Z. and Cai, S., 2020. Recent progress in dynamic covalent chemistries for liquid crystal elastomers. Journal of Materials Chemistry B, 8(31), pp.6610-6623.

107. Hanzon, D.W., Traugutt, N.A., McBride, M.K., Bowman, C.N., Yakacki, C.M. and Yu, K., 2018. Adaptable liquid crystal elastomers with transesterification-based bond exchange reactions. Soft Matter, 14(6), pp.951-960.

108. McBride, M.K., Hendrikx, M., Liu, D., Worrell, B.T., Broer, D.J. and Bowman, C.N., 2017. Photoinduced Plasticity in Cross-Linked Liquid Crystalline Networks. Advanced Materials, 29(17), p.1606509.

109. Tang, J., Yang, J., Yang, H., Miao, R., Wen, R., Liu, K., Peng, J. and Fang, Y., 2018. Boronic ester-based dynamic covalent ionic liquid gels for self-healable, recyclable and malleable optical devices. Journal of Materials Chemistry C, 6(46), pp.12493-12497.

110. Nguyen, A.M. and Seibel, A., 2019, September. Recycling-oriented design in soft robotics. In Actuators (Vol. 8, No. 3, p. 62). Multidisciplinary Digital Publishing Institute.

111. Wang, Y., Wang, Z., He, Q., Iyer, P. and Cai, S., 2020. Electrically Controlled Soft Actuators with Multiple and Reprogrammable Actuation Modes. Advanced Intelligent Systems, 2(6), p.1900177.

112. Agnarsson, I., Dhinojwala, A., Sahni, V. and Blackledge, T.A., 2009. Spider silk as a novel high performance biomimetic muscle driven by humidity. Journal of Experimental Biology, 212(13), pp.1990-1994.

113. Blackledge, T.A., Boutry, C., Wong, S.C., Baji, A., Dhinojwala, A., Sahni, V. and Agnarsson, I., 2009. How super is supercontraction? Persistent versus cyclic responses to humidity in spider dragline silk. Journal of Experimental Biology, 212(13), pp.1981-1989.

114. Roach, D.J., Yuan, C., Kuang, X., Li, V.C.F., Blake, P., Romero, M.L., Hammel, I., Yu, K. and Qi, H.J., 2019. Long liquid crystal elastomer fibers with large reversible actuation strains for smart textiles and artificial muscles. ACS applied materials & interfaces, 11(21), pp.19514-19521.

115. Li, M.H. and Keller, P., 2006. Artificial muscles based on liquid crystal elastomers. Philosophical Transactions of the Royal Society A: Mathematical, Physical and Engineering Sciences, 364(1847), pp.2763-2777.

116. Kuenstler, A.S., Kim, H. and Hayward, R.C., 2019. Liquid crystal elastomer waveguide actuators. Advanced Materials, 31(24), p.1901216.

117. Wang, Y., Dang, A., Zhang, Z., Yin, R., Gao, Y., Feng, L. and Yang, S., 2020. Repeatable and Reprogrammable Shape Morphing from Photoresponsive Gold Nanorod/Liquid Crystal Elastomers. Advanced Materials, 32(46), p.2004270.

118. Coulson, R., Stabile, C.J., Turner, K.T. and Majidi, C., 2021. Versatile Soft Robot Gripper Enabled by Stiffness and Adhesion Tuning via Thermoplastic Composite. Soft Robotics.

119. Liu, H., Tian, H., Shao, J., Wang, Z., Li, X., Wang, C. and Chen, X., 2020. An Electrically Actuated Soft Artificial Muscle Based on a High-Performance Flexible Electrothermal Film and Liquid-Crystal Elastomer. ACS Applied Materials & Interfaces.

120. Naciri, J., Srinivasan, A., Jeon, H., Nikolov, N., Keller, P. and Ratna, B.R., 2003. Nematic elastomer fiber actuator. Macromolecules, 36(22), pp.8499-8505.

121. Krause, S., Dersch, R., Wendorff, J.H. and Finkelmann, H., 2007. Photocrosslinkable Liquid Crystal Main-Chain Polymers: Thin Films and Electrospinning. Macromolecular rapid communications, 28(21), pp.2062-2068.

122. Sharma, A. and Lagerwall, J.P., 2018. Electrospun composite liquid crystal elastomer fibers. Materials, 11(3), p.393.